POLITECNICO DI TORINO

Ph.D. in Materials Science and Technology- XXVIII Cycle

Ph.D. Thesis

Elaboration and characterization of humidity sensors for environmental monitoring

Ahmed Sabry Shehata Afify

197249

Tutor:
Prof. Jean-Marc Tulliani

Department of Applied Science and Technology (DISAT),
Politecnico di Torino, Italy

April 2016

SUMMARY

The water content in surrounding air is an important factor for the well-being of humans and animals, as the level of comfort is determined by a combination of two factors: relative humidity and ambient temperature.

Humidity is also an important factor for operating certain equipment such as high-impedance electronic circuits, electrostatic-sensitive components, high-voltage devices, fine mechanisms, etc. Nonetheless, moisture is the ingredient common to most manufactured goods and processed materials.

Thus, humidity sensors have been receiving wide attentions since decades. Yet, despite the high request, major advances in these sensors in terms of simple structure, lower cost, better selectivity, durability and reliability are always needed. Throughout the years, a large number of materials based on polymers, composite and ceramics have been tested, due to their own features and specific operating conditions. However, great attention has been paid to ceramic materials due to their chemical inertness which allow them to operate in harsh conditions. Amongst the different studied humidity sensors, impedance-based ones are used most commonly. The operation principle of the impedance sensors is based on the dependence of the impedance (or either capacitance or resistance) of the sensor element recognizing the nature and amount of water molecules on the surface or in the bulk. The resistance or impedance of the resistive-type sensor decreases as the relative humidity (RH)increases. Ions or electrons, or both of them, are the conduction carriers for resistive-type humidity sensors. The common construction of the resistive-type ceramic humidity sensors consists of a ceramic substrate with noble metal interdigitated electrodes

coated with humidity sensing ceramic materials, both deposited by screen-print technique [1].

Metal oxides and metal oxide based composites are the most popular materials to be used as resistive sensing elements: TiO_2, TiO_2–SnO_2, TiO_2–WO_3, TiO_2–Cu_2O–Na_2O, $KTaO_3$//TiO_2(bilayered), TiO_2/$KTaO_3$ (bilayered), TiO_2–K_2O–$LiZnVO_4$, Al_2O_3, AlO(OH), SiO_2, WO_3, Cr_2O_3–WO_3, SnO_2, a noble metal doped SnO_2, SnO_2: ZrO_2 (bilayered), single Sb doped SnO_2, K^+-dopedSnO_2–$LiZnVO_4$, MnO_2 –Mn_3O_4, Li^+-doped Fe_2O_3, Au^{3+} and Li^+ co-doped Fe_2O_3, Li^+, Zn^{2+} and Au^{3+} co-doped Fe_2O_3, $NiMoO_4$–MoO_3, Li^+-doped $NiMoO_4$–MoO_3, $CuMoO_4$–MoO_3 and $PbMoO_4$–MoO_3 [1]. Spinel-type oxides and composites based on spinel-type oxides are also used for humidity resistive sensing elements: $MgAl_2O_4$, Sr^{2+}-doped $CoAl_2O_4$, Sr^{2+}-doped $BaAl_2O_4$, Sr^{2+}-doped $ZnAl_2O_4$, $MgFe_2O_4$, $MgAl_2O_4$–$MgFe_2O_4$, $Mg_{0.8}Li_{0.2}Fe_2O_4$, $Mg_{0.9}Sn_{0.1}Fe_2O_4$, $MgFe_2O_4$–CeO_2, $MgCr_2O_4$–TiO_2, Zn_2SnO_4–$LiZnVO_4$ and $ZnCr_2O_4$–K_2CrO_4 [1]. Finally, Perovskite-type oxides and composites based on perovskites have been used for humidity sensing elements too: NaH_2PO_4 doped $BaTiO_3$, $MnTiO_3$, Li+ doped $Ca_{0.35}Pb_{0.65}TiO_3$, $BaNbO_3$, $LaFeO_3$, K+-doped nanocrystalline $LaCo_{0.3}Fe_{0.7}O_3$ ($La_{0.93}K_{0.07}Co_{0.3}Fe_{0.7}O_{3-\delta}$) and Sr-doped $SmCrO_3$ ($Sm_{0.90}Sr_{0.10}CrO_3$) [1].

Preparation techniques can considerably affect the physical, chemical and gas sensing properties of the metal oxide sensors. Developments of new preparative routes, as well as compositional variations, are two perspective approaches for the design of highly sensitive and selective gas sensor materials.

Based on these concepts, the research work of this PhD thesis was devoted to synthesize, characterize and validate new sensing materials for humidity detection.

The thesis is organized into 5 chapters: a general overview of the definition of humidity and of the concept of environmental monitoring, as well as a classification of sensors and a brief information about the selected sensing materials: sepiolite, hematite and pyrolyzed bamboo and the mechanisms involved in water adsorption is given in **Chapter 1**.

The elaboration and the characterization of modified natural sepiolites and the determination of their humidity sensing properties is discussed in **Chapter 2**.

The synthesis by a sol gel technique and the characterization of 'sepiolite -like' sensing materials is discussed in **Chapter 3**.

The effect of doping with metal ions hematite-based humidity sensors is described in **Chapter 4**.

Finally, the fabrication of humidity sensors based on carbon films by using micro carbonized bamboo particles is presented in **Chapter 5.**

The main achievements of this research are the production by simple low cost wet chemical routes of new sensing materials which exhibit promising sensing features towards RH. Among the different examined samples, tungsten-doped sepiolite, sodium doped hematite and micro carbonized bamboo give the best responses and can be considered reliable and reproducible to be incorporated in commercial humidity sensors.

Reference:

[1] T.A. Blanka, L.P. Eksperiandova, K.N. Belikov, Recent trends of ceramic humidity sensors development: A review. Sensors and Actuators B, 228 (2016) 416–442.

ACKNOWLEDGEMENTS

First of all, my deep thanking to Almighty God (**Allah**) for His countless blessings on me and making me able to complete my doctoral thesis. Then I am grateful to **Erasmus Mundus program** (WELCOME Project Action 2) (scholarship application number WELC11011869), Coordination Office: **Politecnico di Torino**, Turin, Italy, for their trust in me and awarding me the financial and moral support for my PhD study.

I would like to extend my sincere gratitude to my advisor **Prof. Jean-Marc Tulliani** for his continuous support, guidance, motivation, enthusiasm, discussions all the time of research activities and writing of different scientific articles and to bring this thesis into its final shape. Also for the partial financial support during the last months of study and indeed, to the **INSTM** research unit at Polito.

Also I would like to thank, Prof.ssa. Barbra Bonelli for her support and guidance during my research, I am grateful to Dr. Ildiko Peter, Dr. Marco Piumetti, Dr. Azhar Hussienn and Dr. Muhammad Ramzan Abdul Karim for their efforts. In addition, I would like to thank the rest of LINCE group (**Daniele Ziegler**, Rebecca, Mirko, Anna, Alessandra, Giorgio, Marta, Marko, Laura, Dr. Paola Palermo and Prof.ssa. Mariangela Lombardi) for their kind help during my lab activities. I simply cannot express the gratitude in words for their all-time support and standing with me during my stay at Politecnico di Torino. I really learned a lot from all of them. I am also grateful to my friend **Dr. Mohamed Abd Elkader Mohamed Hassan** for his moral support, encouragement and motivating words during all this duration and my brothers in Egypt **Dr. Amr Addeck**, **Dr. M. Ataalla**, **Eng. Mohmed Hakim** and **Eng. Hazm Badr**.

Special thanks to my family and relatives for their love and prayers. I cannot express gratitude in words to my father, mother and sisters for all of their sacrifices and hardships bearing on my behalf. I would simply say that it is just because of your endless affection, patience and prayers that enabled me to complete my studies. Finally, I would like to thank my small family, my wife and my cute little angel "**Habiba**".

DEDICATION

I dedicate this work to:

My parents "**Sabry Shehata Batehish**" and "**Fatma Kamel Elbatrik**" ;

My sisters "**Ayat**" and "**Amira**"

My late grandfather "**Kamel Abaas Elbartik**" and my Aunt "**Nagat Batehish**";

and for all the martyrs of freedom in Islamic countries and the entire world

Table of content

Chapter One:

General introduction

1.1 A brief history of sensors

Early sensors were simple devices, measuring a quantity of interest and producing some form of mechanical, electrical, or optical output signal. In just the last decade or so, computing, pervasive communications, connectivity to the Web, mobile smart devices, and cloud integration have added immensely to the capabilities of sensors. A key challenge with sensor technologies is translating promising laboratory prototypes into real-world deployments. The development of Micro Electro-Mechanical Systems (MEMS)-based sensors led to the availability of small, accurate sensors at a price point that made it feasible to integrate them into a wide variety of devices ranging from sports watches to consumer electronics to cars [1].

MEMS have become a key building block for many of the application domains. In recent decades the evolution of sensors has been strongly influenced by Information and Communication (ICT) technologies, with integration of microcontrollers, wireless communications modules, and permanent data storage. These technologies have supported the development of sensor systems with common architectures. Computing, storage, and communications features are used to serve multiple sensors with common connectivity. Collectively these enhancements have produced smart sensors that allow the delivery of intelligent sensor solutions with key features such as digital signal processing and wireless data streaming. In the health and wellness domain, wireless body-worn networks appeared around 1995. These networks—commonly referred to as wireless body area networks (WBAN)—comprise several sensors that measure physiological signals of interest and make that data available wirelessly to a computing device [2].

How will sensors continue to evolve? A number of key trends are emerging. First, we are starting to see the market of sensors. There is a clear transition from limited, specialized use of sensors to greater general use among the public.

Commercial sensor products can be found with greater frequency in pharmacies, sports stores, supermarket chains, and, of course, online. Adoption is rapidly growing in sports and wellness applications, with significant brands staking claims on the market and fueling its growth.

The first personal environmental monitoring products have also emerged, with a focus on improving well-being. Crowd sourcing of data, though still in its infancy, is being driven by sensors either connected to smart phones or tablets or integrated into them, and by apps, and by connectivity to the Web or cloud. Continuous miniaturization of sensors and low-cost systems on chips (SOCs) will continue to fuel future development of the Internet of Things (IOT).

Sensors will fade into the background of everyday life, and interaction with them will become passive and routine. The nexus of health, wellness, and environmental monitoring will continue to evolve and drive changes in human behaviors. Monitoring enabled by sensors will raise our awareness of how lifestyle choices and external influences impact our personal health and well-being. Adoption of data mining, particularly pattern-matching and machine-learning techniques will help unlock the hidden patterns and associations in sensor data. These trends could give us the first glimpses of collective intelligence in which epidemiological insights may be possible with customizations for personalized health [1, 2].

1.2 Basic principle of sensors

Intelligent systems based on sensors and controls can be used for health and safety (e.g., medical diagnostics, air quality monitoring, and detection of toxic, flammable, and explosive gases), energy efficiency, and emission control in combustion processes, and industrial process control for improved productivity and product quality.

There is a continuing need for the development of fast, sensitive, rugged, reliable, and low-cost sensors for applications in harsh industrial environments found in heat treating, metal processing, casting, glass, ceramic, pulp, paper, automotive, aerospace, utility, power, chemical, petrochemical, and food-processing industries[3].

The use of sensors is basically for measurements of physical quantities and for controlling some systems. A transducer is a device that converts energy from one form to another. A sensor converts a physical parameter to an electric output. An actuator converts an electric signal to a physical output. In general, sensors are devices able to convert physical or chemical quantities into electrical signals [4].

There are no uniform descriptions of sensors or the process of sensing. In many cases, the definitions available are driven by application perspectives. Taking a general perspective, a sensor can be defined as: a device that receives a stimulus and responds with an electrical signal [5].

Another common variation, which takes into account the observational element of the measurement, describes a sensor as follows: it generally refers to a device that converts a physical measure into a signal that is read by an observer or by an instrument [6].

The definition of the IEC (International Electrotechnical Committee) states that “the sensor is the primary part of a measuring chain which converts the input variable into a signal suitable for measurement” [7]. Therefore, the need to monitor and control has led to the research and development of very large variety of sensors using different materials and technologies [4].

1.3 Introduction to humidity (concept and some definitions)

Humidity is a very common component in our environment, measurements and/or control of humidity is important not only for human comfort but also for a broad spectrum of industries and technologies [8, 9].

Humidity sensors have gained increasing applications in industrial processing and environmental control. For manufacturing highly sophisticated integrated circuits in semiconductor industry, humidity or moisture levels are constantly monitored in wafer processing. There are many domestic applications, such as intelligent control of the living environment in buildings, cooking control for microwave ovens, and intelligent control of laundry etc. In automobile industry, humidity sensors are used in rear- window defoggers and motor assembly lines. In medical field, humidity sensors are used in respiratory equipment, sterilizers, incubators, pharmaceutical processing, and biological products. In agriculture, humidity sensors are used for green-house air conditioning, plantation protection (dew prevention), soil moisture monitoring, and cereal storage.

In general industry, humidity sensors are used for humidity control in chemical gas purification, dryers, ovens, film desiccation, paper and textile production, and food processing. Generally speaking, a humidity sensor has to fulfill most of the following

requirements to satisfy the wide strange of applications good sensitivity in a wide humidity range, quick response, good reproducibility with no hysteresis, fitness to circuitry, tough durability and long life, resistant to other contaminants (selectivity), insignificant dependence on temperature, simple structure, and low cost[10, 11].

Various types of humidity sensors based on a variety of sensing materials will be described later.

Some definitions related to humidity

Generally the term moisture refers to the amount of water content in liquid or solid (absorption or adsorption), which can be removed without altering of its chemical properties.

The term humidity is reserved for the water vapor content in gases. Absolute humidity is defined as the density of water vapor content per unit volume or the mass m of water vapor per unit volume v of wet gas: dw = m/v. Humidity is measured by an instrument called hygrometer which was invented by Sir John Leslie (1766–1832) [12], it must be selective to water molecules.

Mixing ratio (humidity ratio) r is the mass of water vapor per unit mass of dry gas. Relative humidity is the ratio between water vapor pressure (P_W) and saturated vapor pressure (P_S) (eq. 1):$RH = 100\frac{P_W}{P_S}$(eq. 1)

or the ratio between current absolute humidity and the highest possible absolute humidity at a certain temperature; the value of RH expresses the vapor content as a percentage of the concentration required to cause the vapor saturation. An alternative way to present RH

is as a ratio of the mole fraction of water vapor in a space to the mole fraction of water vapor in the space at saturation. The value of P_w together with partial pressure of dry air P_a is equal to pressure in the enclosure or to the atmospheric pressure P_{atm}, if the enclosure is open to the atmosphere (eq. 2):$P_{atm} = P_W + P_a$ (2)

at temperatures above the boiling point, water pressure could displace all other gases in the enclosure. The atmosphere would then consist entirely of super- heated steam. In this case,$P_w = P_{atm}$. At temperatures above 100°C, RH is a misleading indicator of moisture content because at these temperatures P_s is always more than P_{atm} , and maximum RH can never reach 100%. Thus, at normal atmospheric pressure and a temperature of 100°C, the maximum RH is 100%, whereas at 200°C, it is only 6%.

Above 374°C, saturation pressures are not thermodynamically specified. Dew point temperature is the temperature at which the partial pressure of the water vapor present would be at its maximum, or saturated vapor condition, with respect to equilibrium with a plain surface of ice. It is also defined as the temperature to which the gas–water vapor mixture must be cooled isobarically (at constant pressures) to induce frost or ice (assuming no prior condensation).

The dew point is the temperature at which relative humidity is 100%. In other words, the dew point is the temperature that the air must reach for the air to hold the maximum amount of moisture it can. When the temperature cools to the dew point, the air becomes saturated and fog, dew, or frost can occur. The equation (3) allows calculating the dew point from relative humidity and temperature:

$EW = 10^{(0.66077+7.5t/(237+t)}$ (eq. 3)

With EW: the saturation vapor pressure over water. All temperatures are in Celsius grades. The dew-point temperature is found from the approximation (eq. 4):

$$DP = \frac{(273.3(0.66077 - log_{10}\ EW_{RH})}{log_{10} EW_{RH} - 8.16077} \text{ (eq. 4)}$$

$$EW_{RH} = \frac{(EW).(RH)}{100} \text{ (eq. 5)}$$

The relative humidity displays an inverse relationship with the absolute temperature. The dew-point temperature is usually measured with a chilled mirror. However, below the 0°C dew point, the measurement becomes uncertain, as moisture eventually freezes and a crystal lattice growth will slowly occur, much like a snow flake.

Nevertheless, moisture can exist for a prolonged time below 0°C in a liquid phase, depending on such variables as molecular agitation, rate of convection, sample gas temperature, contaminations, and so forth. Frost point is the temperature (below 0°C) at which the vapor condenses to ice. (Dew point /Forest point temperature) is a function of the pressure of the gas but is independent of temperature and is therefore defined as absolute humidity measurement.

A part per million (ppm) represents water vapor content by volume fraction (ppm_v) or, if multiplied by the ratio of the molecular weight of water to that of air, as ppm_w [12, 13].

1.4 Environmental monitoring

There are many potential factors surrounding us on a daily basis that can affect our wellness or directly influence the development of illness. The effects of poor water and air quality, pathogens in the food supply, and noise and light pollution will continue to have significant health impacts. Increased urbanization, growing use of motor vehicles and other forms of transport, increased waste production (human, animal, and industrial), and other factors will increase pressure on our natural environment.

1.4.1 Definition of environmental monitoring

It can be defined as the systematic sampling of air, water, soil, and biota to observe and study the environment, as well as to derive knowledge from this process [14, 15]. Monitoring can be conducted for a number of purposes, including to establish environmental "baselines, trends, and cumulative effects", to test environmental modeling processes, to educate the public about environmental conditions, to inform policy design and decision-making, to ensure compliance with environmental regulations, to assess the effects of anthropogenic influences, or to conduct an inventory of natural resources [16].

A list of additional purposes for monitoring is presented in Table 1, which shows the importance of monitoring and how its results are ubiquitous in our daily lives [14].

Environmental monitoring programs can vary significantly in the scale of their spatial and temporal boundaries. Monitoring programs can vary significantly in scope, ranging from community based monitoring on a local scale, to large-scale collaborative global monitoring programs such as those focused on climate change [17, 18].

Environmental monitoring is conducted by stewardship organizations, concerns individuals, non-governmental environmental organizations, private consulting firms, and government agencies. In order for monitoring activities to be effective and to culminate into high quality sets of data, it is important to identify focused, relevant, and adaptive questions that can be used to guide the development of a monitoring plan [17, 19].

The "seven habits of highly effective monitoring programs" have been identified in ref. [17]. The successful management of an efficient monitoring program can be challenging, and environmental monitoring has been criticized as being ineffective, costly, and unscientific [14, 17, 19]. However, it is also argued that monitoring can be conducted under a rigorous application of the scientific method and that it is a "fundamental component of environmental science and policy" [14, 17].

Other fundamental components of effective monitoring programs include: the application of quality assurance and quality control measures during the data collection process, data storage and access, and the consultation of experienced statisticians during the sampling design process [15, 19].

Protection of public water supplies	Urban air quality
Weather forecasting	Economic development and land planning
Global climate change	Population growth
Natural resource protection and management	Hazardous, non-hazardous and radioactive waste management
Endangered species and biodiversity	

Table 1: Knowledge-based regulation and benefits of environmental monitoring [14].

1.4.2 Environmental components of monitoring

The five spheres of the Earth System include the atmosphere, hydrosphere, biosphere, lithosphere, and cryosphere [20]. Environmental monitoring can be conducted on biotic and abiotic components of any of these spheres, and can be helpful in detecting baseline patterns and patterns of change in the inter and intra process relationships between and within these spheres.

The interrelated processes that occur between the five spheres are characterized as physical, chemical, and biological processes. The sampling of air, water, and soil through environmental monitoring can produce data that can be used to understand the state and composition of the environment and its processes [20, 21].

Environmental monitoring uses a variety of equipment and techniques depending on the focus of the monitoring.

1.4.3 Importance of environmental monitoring

Environmental monitoring is a necessary component of environmental science and policy design. Despite criticisms that environmental monitoring can be ineffective and costly when programs are poorly planned, well-planned monitoring programs cost little in comparison to the resources that can be protected and the policy design that can be informed [17].

Successes and failures of monitoring programs in the preceding decades have been thoroughly analyzed by the scientific community, and practical solutions for addressing

the standard challenges of monitoring programs are readily available in the scientific literature [17, 19].

In order to achieve valuable results from environmental monitoring activities, it is necessary to adhere to sampling processes that are supported by the traditional scientific method [14], and any effective monitoring program must include focused and relevant questions, appropriate research designs, high quality data collection and management, and careful analysis and interpretation of the results [17].

Long-term monitoring programs are often faced by the challenge of securing long-term funding that will remain stable in a dynamic political environment [17, 19]. In light of the increasing frequency and magnitude of environmental issues that are emerging in this era of globalization, government funding institutions are encouraged to commit to meaningful, stable, and long-term funding of monitoring programs in acknowledgement of the cost savings associated with the protection of natural resources and the improved efficiency of policy design [17].

To encourage a greater commitment to monitoring on behalf of funding agencies, management relevancy, as well as the quality and effectiveness of monitoring programs, program design should include a collaborative effort on behalf of scientists, statisticians, policy makers, and natural resource managers [19]. Despite the challenges that are faced by environmental monitoring, monitoring remains an important tool in the achievement of major advances in environmental science [17].

One of the most prominent examples of the significance of environmental monitoring is in the record of atmospheric CO_2 concentrations recorded in Mauna Loa, Hawaii by Charles

David Keeling [17, 21].This long-term record has led to an increased understanding and awareness of global climate change, one of the greatest environmental challenges that has ever been faced in human history.

The relevance of environmental monitoring in environmental science and policy design is well-established. Environmental monitoring will continue to improve its methodology through advancements in modern science, and government and other funding institutions should increase meaningful, long-term funding towards the establishment of effective monitoring programs distributed from the local to global scales.

1.5 Sensor classification

Sensor classification schemes range from very simple to the complex. Depending on the classification purpose, different classification criteria may be selected. Here, there are several practical ways to look at the sensors.

All sensors may be of two kinds: passive and active where the passive sensor does not need any additional energy source and directly generates an electric signal in response to an external stimulus; that is, the input stimulus energy is converted by the sensor into the output signal [22].

The examples are a thermocouple, a photodiode, and a piezoelectric sensor. Most of passive sensors are direct sensors where they require external power for their operation, which is called an excitation signal. That signal is modified by the sensor to produce the output signal.

The active sensors sometimes are called parametric because their own properties change in response to an external effect and these properties can be subsequently converted into electric signals. It can be stated that a sensor modulates the excitation signal and that modulation carries information of the measured value. For example, a thermistor is a temperature-sensitive resistor. It does not generate any electric signal, but by passing an electric current through it (excitation signal), its resistance can be measured by detecting variations in current and/or voltage across the thermistor. These variations (presented in Ohms) directly relate to a temperature through a known function.

Another example of an active sensor is a resistive strain gauge in which electrical resistance relates to a strain. To measure the resistance of a sensor, electric current must be applied to it from an external power source.

Depending on the selected reference, sensors can be classified into absolute and relative ones. An absolute sensor detects a stimulus in reference to an absolute physical scale that is independent on the measurement conditions, whereas a relative sensor produces a signal that relates to some special case.

An example of an absolute sensor is a thermistor: a temperature-sensitive resistor. Its electrical resistance directly relates to the absolute temperature scale of Kelvin. Another very popular temperature sensor, a thermocouple, is a relative sensor. It produces an electric voltage that is function of a temperature gradient across the thermocouple wires. Thus, a thermocouple output signal cannot be related to any particular temperature without referencing to a known baseline.

Another example of the absolute and relative sensors is a pressure sensor. An absolute-pressure sensor produces signal in reference to vacuum—an absolute zero on a pressure scale. A relative-pressure sensor produces signal with respect to a selected baseline that is not zero pressure (e.g., the atmospheric pressure).

Another way to look at a sensor is to consider all of its properties, such as what it measures (stimulus), what its specifications are, what physical phenomenon it is sensitive to, what conversion mechanism is employed, what material it is fabricated from, and what its field of application is. Tables 2–4, adapted from Ref. [23], represent such a classification scheme, which is pretty much broad and representative.

According to specifications such as sensitivity, stability (short and long term), accuracy, speed of response, selectivity, overload characteristic, hysteresis, operating life, cost, size, weight, stimulus range, resolution, environmental conditions (surroundings), linearity, dead band, output format, etc.

According to the contact between sensor and the quantity of interest:

- **Contact**: This approach requires physical contact with the quantity of interest. Comfort and biocompatibility are important considerations for on-body contact sensing. Contact sensors may have restrictions on size and enclosure design. Contact sensing is commonly used in healthcare- and wellness-oriented applications, particularly where physiological measurements are required, such as in electrocardiography (ECG), electromyography (EMG), and electroencephalography (EEG). The response time of contact sensors is determined by the speed at which the quantity of interest is transported to the measurement

site. Contact surface effects, such as the quality of the electrical contact between an electrode and subject's skin, also play a role. Poor contact can result in signal noise and the introduction of signal artifacts.

- **Non-contact**: This form of sensing does not require direct contact with the quantity of interest. It is commonly used in ambient sensing applications. Such applications must have minimum impact on the environment or subject of interest in order to preserve state. Sensors that are used in non-contact modes, passive infrared (PIR), for example, generally have fast response times.
- **Sample removal**: This approach involves an invasive collection of a representative sample by a human or automated sampling system. Sample removal commonly occurs in healthcare and environmental applications, to monitor E. coli in water or glucose levels in blood, for example. Such samples may be analyzed using either sensors or laboratory-based analytical instrumentation [24].

According to sensing material as in table 2:

Inorganic	**Organic**
Conductor	Insulator
Semiconductor	Liquid, gas or plasma
Biological substance	Other

Table 2: Different types of sensing materials

According to detection means used in sensor: biological, chemical, electric, magnetic, electromagnetic wave, heat, temperature, mechanical displacement, radioactivity, radiation and other.

According to conversion phenomena as in table 3:

Physical	chemical	Biological
Thermoelectric	Chemical transformation	Biochemical transformation
Photoelectric	Physical transformation	Physical transformation
Photomagnetic	Electrochemical process	Effect on test organism
Magnetoelectric	spectroscopy	Spectroscopy
Electromagnetic	other	Other
Thermoelastic		
Electroelastic		
Thermomagnetic		
Thermooptic		
Photoelastic		
Other		

Table 3: Different types of conversion phenomena

According to the field of application: agriculture, civil engineering, construction, distribution, commerce, finance, energy, power, health, medicine, manufacturing, military, scientific measurement, transportation (excluding automotive), domestic, appliances, environmental, meteorology, security, information, telecommunication, marine, recreation, toys, space and others.

According to stimulus as reported in table 4:

Chemical	Biological	Acoustic	Electric	Magnetic	Optical	Mechanical	Thermal
Components (identities, concentration and states)	Biomass (types, concentration and states)	Wave amplitude, phase, polarization, spectrum and wave velocity	Charge, current, potential, voltage, electric field (amplitude, phase, polarization and spectrum), permittivity and conductivity	Magnetic field (amplitude, phase, polarization, spectrum), magnetic flux and permeability	Wave amplitude, refractive index, emissivity, reflectivity and absorption	Position (linear, angular), acceleration, force, pressure, stress, strain, mass, density, moment, torque, speed of flow, rate of mass transport, shape, roughness, orientation, stiffness, compliance, viscosity, crystallinity, and structural integrity	Type, energy intensity, Temperature, flux, specific heat and thermal conductivity

Table 4: Different types of stimulus

1.5.1 Characterization of sensors

The performance of chemical sensors should be expressed in the form of numbers. The criteria defined by traditional analytical chemistry were established primarily for characterizing analytical results and analytical procedures, but not for describing devices. We must distinguish whether a process (the analysis) must be evaluated or a device (the sensor) is the subject of consideration.

Some of the traditional criteria, like sensitivity, can be applied to procedures as well as to devices. Others, like accuracy, have been defined clearly for validating measurement results. A measured value may be correct or false, but a sensor itself may be neither correct nor false [25, 26].

1.5.2 Validation of results

The following units are commonly used for characterizing the validity of analytical results:

• **Accuracy**: an expression of the agreement between the measurement results (given as the average value of a measurement series) and the true value. It is also a measure of the systematic error, i.e. deviation from the true value (normally given as a percentage).

• **Precision**: an expression of the random error of a measurement series or, in other words, of the scattering of single values around the average value. The generally accepted way to express precision is with the standard deviation (STD). The latter is the mathematical term for the width of the Gaussian error distribution curve given in the form of σ (the distance between the centre and the inflection point of the Gaussian curve).

For practical purposes, instead of σ, the estimated value s is determined from a finite population of single values. The approximate values are given by the equation (6):

$$s = \sqrt{\frac{\sum(x-y)^2}{n-1}} \text{ (eq. 6)}$$

where (x) is every individual value, (y) the average value and(n) is the number of measurements [26].

1.5.3 Common parameters of sensors

The following list contains static as well as dynamic parameters which can be used to characterize the performance of chemical sensors [26, 27].

• **Sensitivity**: change in the measurement signal per concentration unit of the analyte, i.e. the slope of a calibration graph.

• **Detection limit**: the lowest concentration value which can be detected by the sensor in question, under definite conditions. Whether or not the analyte can be quantified at the detection limit is not determined. Procedures for evaluation of the detection limit depend on the kind of sensor considered.

• **Dynamic range**: the concentration range between the detection limit and the upper limiting concentration.

• **Selectivity**: an expression of whether a sensor responds selectively to a group of analytes or even specifically to a single analyte. Quantitative expressions of selectivity exist for different types of sensors.

• **Linearity**: the relative deviation of an experimentally determined calibration graph from an ideal straight line. Usually values for linearity are specified for a definite concentration range.

• **Resolution**: the lowest concentration difference which can be distinguished when the composition is varied continuously. This parameter is important chiefly for detectors in flowing streams.

• **Response time**: the time for a sensor to respond from zero concentration to a step change in concentration. Usually specified as the time to rise to a definite ratio of the final value. Thus, e.g. the value of t_{99} represents the time necessary to reach 99 percent of the full-scale output. The time which has elapsed until 63 percent of the final value is reached is called the time constant.

• **Hysteresis**: the maximum difference in output when the value is approached with (a) an increasing and (b) a decreasing analyte concentration range. It is given as a percentage of full-scale output.

• **Stability**: the ability of the sensor to maintain its performance for a certain period of time. As a measure of stability, drift values are used, e.g. the signal variation for zero concentration.

• **Life cycle**: the length of time over which the sensor will operate. The maximum storage time (shelf life) must be distinguished from the maximum operating life. The latter can be specified either for continuous operation or for repeated on-off cycles.

1.6 Ceramic sensing materials

Ceramics are crystalline materials which are very useful in sensor fabrication. The reason why these materials are widely used is due to the fact that they exhibit a number of specific features which enable their cost to become lower and their reliability to increase, thus occupying a significant position in sensor technology.

The main common properties are structural strength, thermal stability, low weight, resistance to many chemicals, the ability to bond with other materials, the ability to modify the composition by the addition of dopants and modifiers and excellent electrical insulating properties. Another advantage of ceramics is that they mostly do not react with oxygen and thus do not create oxides.

Development of new sensors has rapidly grown in the last years especially in control systems, with both high sensitivity and rapid response. The concept of ceramic sensors include all sensors produced using ceramic technology [28].

Since 1950s ceramic elements are still employed as gas chemiresistors [29]. The sintered block arrangement is considered to be the simplest ceramic sensor design. The block is prepared by sintering metal oxide powders, with the electrode wires embedded in the block. However, a porous structure is necessary to increase both the surface-to-volume ratio and the gas penetrability of a gas-sensing matrix.

Metal oxides and metal oxide based composites are the most popular materials to be used as resistive sensing elements: TiO_2, TiO_2–SnO_2, TiO_2–WO_3, TiO_2–Cu_2O–Na_2O, $KTaO_3$//TiO_2(bilayered), TiO_2/$KTaO_3$ (bilayered), TiO_2–K_2O–$LiZnVO_4$, Al_2O_3, AlO(OH), SiO_2, WO_3, Cr_2O_3–WO_3, SnO_2, a noble metal doped SnO_2, SnO_2:

ZrO_2(bilayered), single Sb doped SnO_2, K^+-dopedSnO_2–$LiZnVO_4$, MnO_2 –Mn_3O_4, Li^+-doped Fe_2O_3, Au^{3+} and Li^+ co-doped Fe_2O_3, Li^+, Zn^{2+} and Au^{3+} co-doped Fe_2O_3, $NiMoO_4$–MoO_3, Li^+-doped $NiMoO_4$–MoO_3, $CuMoO_4$–MoO_3 and $PbMoO_4$–MoO_3 [30]. Spinel-type oxides and composites based on spinel-type oxides are also used for humidity resistive sensing elements: $MgAl_2O_4$, Sr^{2+}-doped $CoAl_2O_4$, Sr^{2+}-doped $BaAl_2O_4$, Sr^{2+}-doped $ZnAl_2O_4$, $MgFe_2O_4$, $MgAl_2O_4$–$MgFe_2O_4$, $Mg_{0.8}Li_{0.2}Fe_2O_4$, $Mg_{0.9}Sn_{0.1}Fe_2O_4$, $MgFe_2O_4$–CeO_2, $MgCr_2O_4$–TiO_2, Zn_2SnO_4–$LiZnVO_4$ and $ZnCr_2O_4$–K_2CrO_4. Finally, Perovskite-type oxides and composites based on perovskites have been used for humidity sensing elements too: NaH_2PO_4 doped $BaTiO_3$, $MnTiO_3$, Li+ doped $Ca_{0.35}Pb_{0.65}TiO_3$, $BaNbO_3$, $LaFeO_3$, K+-doped nanocrystalline $LaCo_{0.3}Fe_{0.7}O_3$ ($La_{0.93}K_{0.07}Co_{0.3}Fe_{0.7}O_{3-\delta}$) and Sr-doped $SmCrO_3$ ($Sm_{0.90}Sr_{0.10}CrO_3$) [30].

Metal oxide powders for ceramic sensors can be synthesized using various methods which are described in literature such as sol–gel, flame pyrolysis, and hydrothermal synthesis [31, 32]. Many of these technologies offer some significant advantages for fabricating nanoparticles, such as simplicity, flexibility, low cost, ease of use on large substrates. By modifying the parameters of synthesis and sintering a new gas-sensing properties can be obtained [33].

Amongst the many materials used as semiconducting gas sensor, from now on, I will focus only on the ones used in the experimental part: sepiolite, hematite and pyrolyzed bamboo.

1.6.1 Inorganic clays

Clays are naturally occurring minerals which are formed by the weathering and decomposition of igneous rocks, they are inexpensive and eco-friendly materials and they have found numerous applications. The term clay is generally applied to (1) a natural material with plastic properties, (2) particles of very fine size: customarily defined as particles smaller than two micrometers, and (3) very fine mineral fragments or particles composed mostly of hydrous-layer silicates of aluminum, though occasionally containing magnesium and iron.

Although, in a broader sense, clay minerals can include virtually any mineral of the above-cited particle size, this definition is restricted to represent hydrous-layer silicates and some related short-range ordered alumino-silicates, both of which occur either exclusively or frequently in very fine-size grades[34].

A large variety of different clay minerals exist, which vary in their layer arrangement, substitutions and composition. Clays are generally classified by structure as allophone, kaolinite, halloysite, smectite, illite, chlorite, vermiculite, attapulgite–palygorskite-sepiolite and mixed layer minerals [35]. They are layered minerals, and each layer is comprised of fused sheets of octahedra of Al^{3+}, Mg^{2+}or Fe^{3+} oxides and sheets of tetrahedra of Si^{4+} oxides [36].

Isomorphic substitution of metal atoms in the clay lattice can lead to an overall negative charge on individual clay layers. This charge is compensated for by cations which exist in the region between the clay layers known as the interlayer region. These interlayer cations are exchangeable cations and may trade places with other cations under

appropriate conditions. The cation exchange capacity (CEC) of clay minerals depends upon crystal size, pH and the type of exchangeable cation [37].

In naturally occurring clays there is variability in the charge-balancing interlayer cations, which tend to be small inorganic species such as Na^{+} and Ca^{2+} cations. The development of X-ray diffraction techniques in the 1920s and the subsequent improvement of microscopic and thermal procedures enabled investigators to establish that clays are composed of a few groups of crystalline minerals. The introduction of electron microscopy methods proved very useful in determining the characteristic shape and size of clay minerals. More recent analytical techniques such as infrared spectroscopy, neutron diffraction analysis, Mössbauer spectroscopy, and nuclear magnetic resonance spectroscopy have helped advance scientific knowledge of the crystal chemistry of these minerals.

Nanoclays are naturally occurring aluminum silicate, primarily composed of fine-grained minerals having natural structure with sheet-like geometry. The sheet-structured hydrous silicates are generally referred to as phyllosilicates. These clay minerals have been widely studied in practical applications such as in geology, agriculture, construction, engineering, process industries, and environment applications.

They provide an attractive alternative for the decontamination of soils, underground waters, sediments and industrial effluents [38]. They are also widely used materials in drug products like excipients and active agents [39, 40]. Millions of tons of these materials are used annually and their applications will continue to grow at a rate equivalent to the growth of national products [41].

Clay materials contain water in several forms. The water may be held in pores and may be removed by drying under ambient conditions. Water also may be adsorbed on the surface of clay mineral structures and in smectites, vermiculites, hydrated halloysite, sepiolite, and palygorskite; this water may occur in interlayer positions or within structural channels. The water adsorbed between layers or in structural channels may further be divided into zeolitic and bound waters. The latter is bound to exchangeable cations or directly to the clay mineral surfaces. It is generally agreed that the bound water has a structure other than that of liquid water; its structure is most likely that of ice.

As the thickness of the adsorbed water increases outward from the surface and extends beyond the bound water, the nature of the water changes either abruptly or gradually to that of liquid water.

Ions and molecules adsorbed on the clay mineral surface exert a major influence on the thickness of the adsorbed water layers and on the nature of this water. The non liquid water may extend out from the clay mineral surfaces as much as 6–10 nm. The water-retention capacity of clay minerals is generally proportional to their surface area. The ion-exchange properties of the clay minerals are extremely important because they determine the physical characteristics and economic use of the minerals.

Depending on deficiency in the positive or negative charge balance (locally or overall) of mineral structures, clay minerals are able to adsorb certain cations and anions and retain them around the outside of the structural unit in an exchangeable state, generally without affecting the basic silicate structure. These adsorbed ions are easily exchanged by other ions. The exchange reaction differs from simple sorption because it has a quantitative relationship between reacting ions.

Exchange capacities vary with particle size, perfection of crystallinity, and nature of the adsorbed ion; hence, a range of values exists for a given mineral rather than a single specific capacity. With certain clay minerals such as imogolite, allophane, and to some extent kaolinite that have hydroxyls at the surfaces of their structures, exchange capacities also vary with the pH of the medium, which greatly affects dissociation of the hydroxyls.

Under a given set of conditions, the various cations are not equally replaceable and do not have the same replacing power. Calcium, for example, will replace sodium more easily than sodium will replace calcium. Sizes of potassium and ammonium ions are similar, and the ions are fitted in the hexagonal cavities of the silicate layer. Vermiculite and vermiculitic minerals preferably and irreversibly adsorb these cations and fix them between the layers. Heavy metal ions such as copper, zinc, and lead are strongly attracted to the negatively charged sites on the surfaces of the 1:1 layer minerals, allophane and imogolite, which are caused by the dissociation of surface hydroxyls of them [34].

The solubility of clay minerals in acids varies with the nature of the acid and its concentration, the acid-to-clay ratio, the temperature, the duration of treatment, and the chemical composition of the clay mineral attacked. In general, ferromagnesian clay minerals are more soluble in acids than their aluminian counterparts. Incongruent dissolutions may result from reactions in a low-acid-concentration medium where the acid first attacks the adsorbed or interlayer cations and then the components of the octahedral sheet of the clay mineral structure. When an acid of higher concentration is used, such stepwise reactions may not be recognizable, and the dissolution appears to be congruent.

One of the important factors controlling the rate of dissolution is the concentration in the aquatic medium of the elements extracted from the clay mineral. Higher concentration of an element in the solution hinders to a greater degree the extractions of the element.

In alkaline solutions, a cation-exchange reaction first takes place, and then the silica part of the structure is attacked. The reaction depends on the same variables as those stated for acid reactions [34, 42].

1.6.1.1 Sepiolite

Sepiolite naturally occur in soils, in sedimentary "clay deposits," and are alteration products of certain basic igneous rocks. Although sepiolite and attapulgite are found in similar environments, the presence of both in the same deposit is not common [42].

It resembles metacolloidal asbestos, occur in silicified serpentinites accompanied by veinlets of quartz, opal, and calcite, replacing older carbonate host rock [43].

Both fibrous and lamellar sepiolite was reported from solution cavities in a Madagascar limestone [44]. It requires alkaline conditions and high Si and Mg activities for stability [45].The excellent deposit of sepiolite which afford a good material, but not in large amounts include: from antiquity, at Eskishehir, in Turkey, from Vallecas, near Madrid, and Cabanas, near Toledo, in Spain, and at Nugssuaq in western Greenland, in the USA [46]. Owing to its absorptive properties, sepiolite is used commercially as carriers, fillers, clarifying agents, and could be used in different industrial applications when modified chemically or thermally including construction, coating etc. [47, 48].

1.6.1.2 Structure of Sepiolite

Sepiolite is a papyrus-like or fibrous hydrated magnesium silicate mineral and is included in the phyllosilicate group because it contains a continuous two-dimensional tetrahedral sheet of composition Si_2O_5. It differs, however, from the other layer silicates because it lacks continuous octahedral sheets.

Its structure can be regarded as consisting of narrow strips or ribbons of 2:1 layers that are linked stepwise at the corners. Since the octahedral sheet is discontinuous, some octahedral magnesium ions are exposed at the edges and hold bound water molecules. In addition to the bound water, variable amounts of zeolitic (i.e., free) water are contained in the rectangular channels. Sepiolite has an ideal composition and empirical formula of $Mg_8Si_{12}O_{30}\ (OH)_4(OH_2)_4(H_2O)_8$ [49].

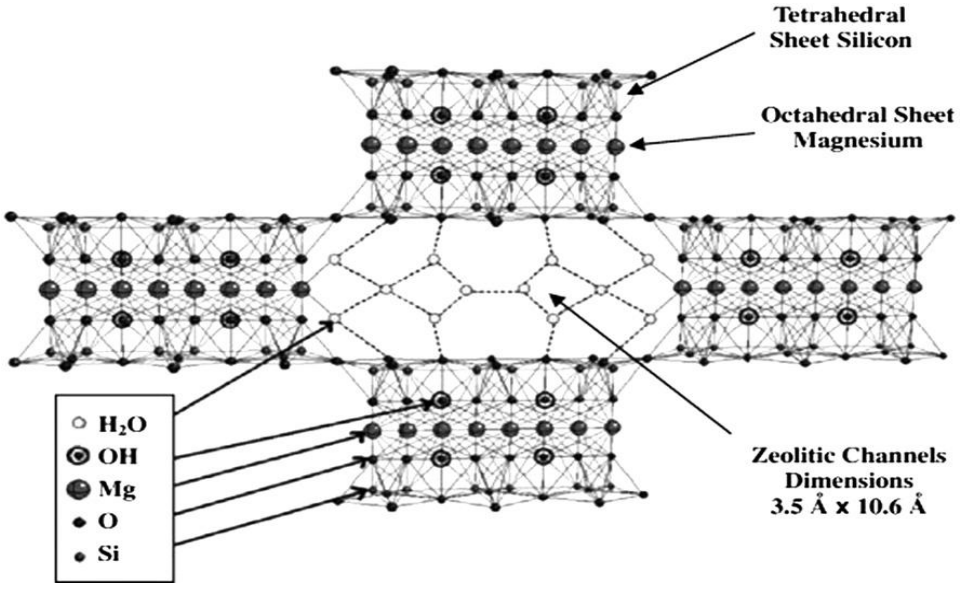

Fig.1. Schematic representation of the sepiolite structure [50].

Sepiolite is a highly porous mineral with low bulk density and thus, sepiolite is an effective absorbent. At the same time, due to its rigid structure, sepiolite will not swell in the presence of water or other liquids [51].

The unit cell of the clay has an orthorhombic symmetry with lattice parameters a = 1.35 nm, b = 2.70 nm, and c = 0.53 nm. Like palygorskite, rectangular channels forms parallel the c-axis of the unit cell and often contain zeolitic water or hydroxyl groups. A trivalent cation (Mn^{3+}, Al^{3+}, or Fe^{3+}) is often found as a substitutional impurity occupying a silicon site in a tetrahedral sheet [52].

When sepiolite is heated both forms of water (zeolitic and bound waters) may be removed by heating to temperatures on the order of 100–200°C and in most cases, except for hydrated halloysite, are regained readily at ordinary temperatures. Hydroxyl ions are driven off by heating clay minerals to temperatures of 400–700°C. The rate of loss of the hydroxyls and the energy required for their removal are specific properties characteristic of the various clay minerals. This dehydroxylation process results in the oxidation of Fe^{2+} to Fe^{3+} in ferrous-iron-bearing clay minerals.

At temperatures beyond dehydroxylation, the clay mineral structure may be destroyed or simply modified, depending on the composition and structure of the substance. In the presence of fluxes, such as iron or potassium, fusion may rapidly follow dehydroxylation. In the absence of such components, particularly for aluminous dioctahedral minerals, a succession of new phases may be formed at increasing temperatures prior to fusion. Information concerning high-temperature reactions is important for ceramic science and industry [44].

As already abovementioned, sepiolite contains four different types of water molecules:

(i) Hygroscopic, (ii) zeolitic, (iii) bound and (iv) hydroxylated water. The most probable binding sites on the sepiolite surface are surface hydroxyls and Lewis acidic centers.

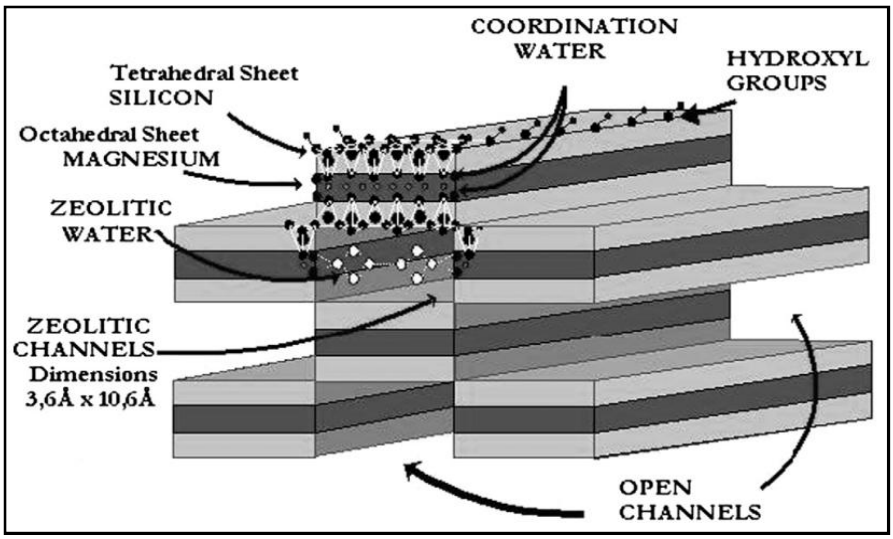

Fig. 2. Scheme of sepiolite main structure characteristics

1.6.2 Semiconductor humidity sensors

There are two types of semiconductors: intrinsic in which electrical conductivity doesn't depend on impurities and extrinsic in which electrical conductivity depends on impurities which can be obtained by doping (either by diffusion or ion implantation).

Literally conductivity occurs by holes or electrons. In intrinsic semiconductors, holes are promoted by electron mobility so number of electrons is equal to the number of holes. Extrinsic semiconductors have different concentrations of electrons and holes, generally p-type when number of holes is more than number of electron and n-type in which number of electrons is higher than number of holes. Literally, it is well known that the types of conduction are ionic (mostly for porous sintered ceramics), electronic and electrolyte.

1.6.3 Tungsten oxide

Because of its interesting chemical, optical and electrical properties, tungsten oxide (WO_3), which is a n-type semiconductor, has been the object of extensive research.

It was studied in numerous fields such as electrochromism [53-56], photoelectrochemical [57, 58] and particularly as gas sensor [59-64]. Pure WO_3 has good sensing properties to oxidizing gases such as NO and NO_2 [65, 66], O_3 [67, 68] and Cl_2 [69]. However for reducing gases (CO, NH_3, ethanol, methanol, etc.), the surface modification of WO_3 by noble catalyst (Pt, Au, and Pd) is required.

The sensing mechanism of gas sensors based on modified metal oxides by noble metals (NM-MO) has been reported in the literature by several authors [70]. It is accepted that the sensing mechanism is associated to the change of the resistance in contact with the chemisorbed oxygen and gas species on the surface of the metal oxide.

For NM-MO such as Pd–SnO_2, Pt– WO_3 and Pd– WO_3, the catalyst on the surface of the metal oxides favors the presence of oxygen species (O^-, $O_2^-$and O^{2-}) on the surface which depends strongly on the temperature [71-74]. The ionization of oxygen molecules by the capture of electrons from the conduction band of oxides results in an electron depletion region on the surface of the sensor material. When the surface of the gas sensors is exposed to reducing gases, the oxygen species react with the gases and electrons are given back to the semiconductor, which increases its conductivity [75].

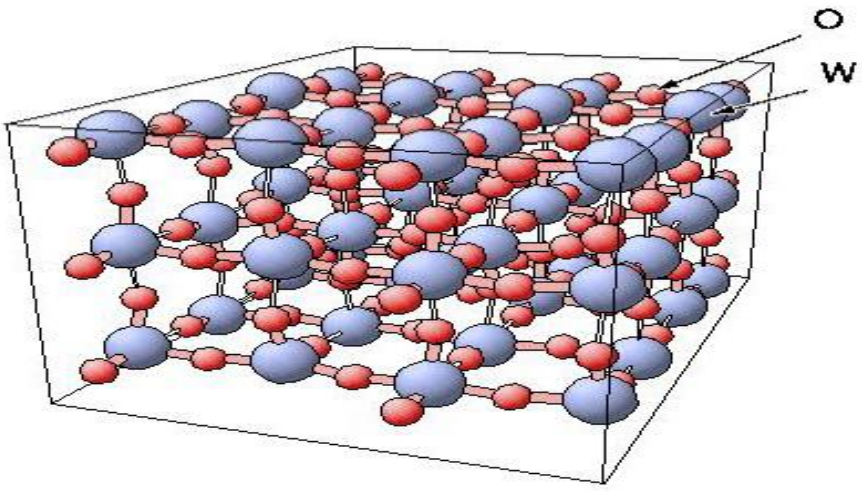

Fig. 3. WO_3 lattice monoclinic, pseudo-cubic [76].

1.6.4 Iron oxide

Fe_2O_3 has been widely studied due to its abundance, low cost, and interesting magnetic, semiconducting, and electrochemical properties [77-84].

α-Fe_2O_3 is a n-type semiconductor with an experimental band-gap of 2.2 eV; it has been proven to be a good gas sensitive material for detection of toxic, combustible, explosive and harmful gases in both domestic and industrial applications and extensive studies have been carried out to improve the gas sensing performances of the α-Fe_2O_3 based sensors [85, 86]. It is well-known that the shape and size of α-Fe_2O_3 have a significant influence on its gas sensing properties [87-91].

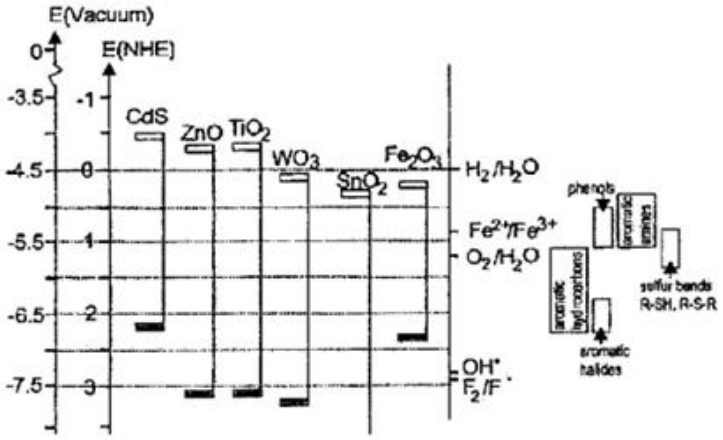

Fig.4. Position of the conduction and valence bands of somesemiconductors at pH = 1 and some redox potentials [92, 93]

In addition it was identified as a charge transfer semiconductor [94, 95].

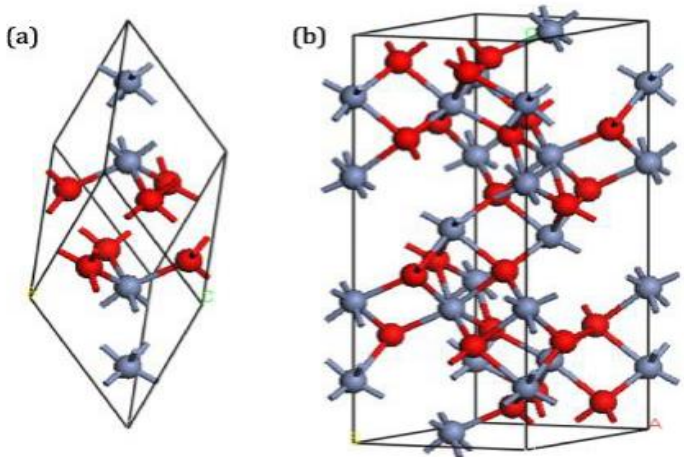

Fig.5. Crystal structure of the corundum structure. The transition metal atoms are labeled as grey while O is red. (a) The rhombohedral primitive cell. (b) The hexagonal representation [94].

1.7 Water adsorption mechanism

Dry oxide contact with water molecules by a dissociative mechanism to form two hydroxyl ions for each water molecule, which are adsorbed on the metal cation that has a high local charge density and exerts a strong electrostatic field.

Proton reacts with adjacent surface O^{2-} to form a second hydroxyl group. So, the first layer of adsorbed water is chemically adsorbed and the subsequent layers are physically adsorbed. First physisorbed layer is characterized by double hydrogen bonding of a single water molecule.

Other layers are singly bonded and form liquid like network. Physisorption takes place at temperatures below 100°C.In case of presence of pores in the microstructure of the semiconductor, the most important factors are: the size of the pores and their distribution which are responsible for capillary condensation. It is possible to evaluate the pore radius at which capillary condensation occurs at different temperatures (T) by using the Kelvin equation (7) : $r_k = \frac{2\gamma M}{\rho^{RT} ln(\frac{P_S}{P})}$ (eq. 7)

Where r_k is the Kelvin radius, P is the water-vapor pressure, P_s is the water-vapor pressure at saturation, and γ, ρ and M are the surface tension (72.75 dyn cm^{-1} at 20°C), density and molecular weight of water, respectively. Water condensation takes place in all the pores with radii up to r_k, at given temperatures and water-vapor pressures. The smaller ther_k, or the lower the temperature, the more easily condensation occurs [96]. These physical interaction mechanisms between water and oxide surfaces are largely recognized to be the basis of the operative mechanisms of a wide range of different humidity-sensor materials.

However, the main problems of most ceramic sensors are their high resistance to low humidity and the need for periodic heat cleaning to recover sensor properties which result in the formation of undesired hydroxyl groups which need more than 400°C to be removed, so commercial sensors are usually accompanied with a heater for the purpose of generation and prolonged exposure to humidity and environmental pollutants affect on the sensor performance [97].

1.7.1 Ionic-type humidity sensors

The detection mechanism of ionic-type humidity sensors is strictly related to the above water-adsorption mechanisms. Moisture can be detected by measuring humidity-sensitive variations in conductivity, which ionic-type oxides undergo as a result of water adsorption: the oxides react to humidity by decreasing their resistivity [97].

The conduction mechanism depends on the surface coverage of adsorbed water. When only hydroxyl ions are present on the oxide surface, the charge carriers are protons, from hydroxyl dissociation, which hop between adjacent hydroxyl groups.

When water is present, but surface coverage is not complete, H_3O^+ diffusion on hydroxyl groups dominates, but proton transfer between adjacent water molecules in clusters also takes place [97].

When the first physisorbed water layer is continuous, charge transport is governed by proton hopping between neighboring water molecules in the continuous film. The easy dissociation of physisorbed water, due to the high electrostatic fields in the chemisorbed layer, produces H_3O^+ groups. The charge transport occurs when H_3O^+ releases a proton to a nearby H_2O molecule, ionizing it and forming another H_3O^+, resulting in the hopping of

protons from one water molecule to another [97]. This process is known as the Grotthuss chain reaction. This mechanism means that higher resistivity of the oxides is observed at low RH values. This is because mobile protons may arise from the dissociation of the hydroxyl groups or of the water molecules, but the activation energy required to dissociate hydroxyl ions is higher than that necessary to dissociate water molecules.

A higher carrier concentration is found when more than one layer of physisorbed water molecule is present on the surface. These molecules are singly hydrogen-bonded and form a liquid-like network, which greatly increases the dielectric constant and, therefore, the proton concentration.

Moreover, in addition to the protonic conduction in the adsorbed layers, electrolytic conduction occurs in the liquid layer of water condensed within capillary pores, thereby resulting in an enhancement of conductivity. Thus, primary concern of ionic type humidity sensor is controlling porosity and surface activity where highly porous and large surface area is desirable for the enhancement of sensitivity towards humidity. Pore size distributions ranging from 20-500nm shows the best performance [97].

For single crystals, capillary condensation cannot be responsible for humidity sensing and surface conduction in multi-layered water molecules cannot be ignored [98].

Another model proposed that ionic and electronic conduction coexist in porous ceramics at any humidity. The resistance of a sensor is then given by the sum of electronic conduction of the crystal grains and the proton hopping between two water molecules adsorbed on the grain surfaces [97]. The following equation (8) was derived:

$lg\,{}^{R_\Phi}/_{R_0} = (\lg a - \lg \Phi) / (1 + b/\Phi)$ (eq. 8) Where R_Φ and R_0 are the resistance of the porous ceramic element when relative humidity is RH% and 0% respectively, Φ is the concentation of quasi liquid water (equal to $(RH)^n$, where n is the correction index) and a and b are theoretical constants depending on the compostion of the ceramic and the pore structure. This model takes into consideration the Grotthuss proton-transfer mechanism and the intrinsic resistivity of the materials. The same authors also proposed an interesting method for controlling the porosity of humidity-sensitive ceramics by using graphite powder as the pore former for Co-Fe and Mg-Cr spinels, which was removed during sintering. When graphite powder was added for the fabrication of porous Co-Fe spinel, the porosity of the specimen increased remarkably and graphite did not affect the composition of the matrix, thereby resulting in increased resistance versus RH sensitivity [98, 99].

1.7.2 Influence of the addition of alkali ions

The addition of alkali ions has been reported to be effective in improving the performance of many different kinds of sensing materials, by influencing the microstructure because of an increase of open porosity, a decrease of average pore size and of grain size [100]. Moreover, alkali addition enhances the formation of physisorbed layers [101], allows the ceramic to be easy sintered, lowers the intrinsic resistance without impairing the sensitivity and alkali ions may move between adsorbed water molecules which increases the number of charge carriers and thus the conductivity [102].

1.7.3 Electronic-type humidity sensors

The demand for humidity sensors able to operate at temperatures higher than 100°C led to the development of humidity-sensing devices based on different detection mechanisms. To this aim, semiconductor humidity sensors using metal oxides were investigated. In this case, water molecules behave as a reducing gas so electrons transfer from them to the metal oxide sensing material. Firstly, the surface of metal oxides adsorbs oxygen ions from air which determines the resistivity of the oxide surface.

Secondly, oxidative reactions take place between reducing gases and oxygen ions resulting in releasing electrons which increase the electrical conductivity of the oxide surface. However, another proposed mechanism indicates that during the chemisoprtion where two OH^- groups are formed with H^+ bonds to the oxide ion and OH^- bonds to metal ion there is no electron transfer [103].

In perovskite, donation of electrons from water molecules is attributed to the presence of surface defects which trap electrons which are liberated by the adsorption of water molecules [104]. So, released electrons can be restored in the conduction band in case of n-type semiconductors and in valence band in case of p-type ones.

The presence of inflammable gases, causes resistivity changes in the same direction as water vapor, as one of the major problems related to the use of electronic conductivity-based humidity sensors.

1.7.4 Solid-electrolyte-type humidity sensors

These materials have been studied to control humidity at high temperature for several industrial applications, such as drying processes, combustion control systems and control of humidity in drying ovens. Proton conductors have been used for humidity sensing at high temperatures. High proton conductivity, good stability at operating temperatures, low electronic conductivity and good mechanical properties are the requirements of the materials to be used as proton conductors in high temperature electrochemical sensors. The variation of water vapor pressure is measured by the electromotive force (e.m.f.) generated at the electrodes of the cell. The e.m.f. varies linearly with the logarithm of water partial pressure, the concept of it is shown in Fig.6.

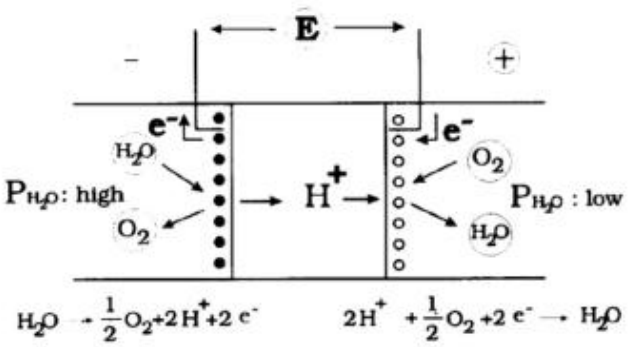

Fig.6. Concept of the water-vapor concentration cell.

Another type of solid-electrolyte humidity sensor, which does not need a reference atmosphere, is based on yttria-stabilized zirconia, an oxide ion conductor, which uses the limiting current appearing in the diffusion-controlled electrolysis of water vapor and operates at 450°C [105]. Based on this principle, Yagi et al. developed a sensor with the cathode and the anode on the same plane; the cathode also acts as the diffusion control hole [106- 109].

1.8 **Summary**

Demands for humidity sensors has increased greatly in the last years, to find novel, low cost and high efficient sensing materials that can be operated at high temperatures and in harsh conditions. The effect of microstructure of the ceramic sensing materials, especially the presence of pores which enhance the capillary condensation of water, in addition with doping that can raise the sensitivity to water vapor were deeply investigated throughout the years. Therefore, on the basis of previous experiences in the lab and after a literature survey, it was decided in this Ph.D thesis to develop humidity sensors based on modified sepiolite, to exploit the high specific surface area of this material. To this aim, natural sepiolite was doped with semiconducting metal oxides to enhance its humidity sensing properties. Then, a synthetic like sepiolite was synthesized too, with the purpose of controlling the composition of the new materials, to overcome the presence of impurities in the original clays.

Finally, alkaline-doped hematite was investigated too, again on the basis of previous experiences, as well as, for the first time, carbon-based materials produced form agriculture wastes, as an alternative to more expensive carbon nanotubes or graphene.

References

[1] Marek, Jiri and Udo-Martin Gómez, “MEMS (Micro-Electro-Mechanical Systems) for Automotive and Consumer”, in Chips 2020: A Guide to the Future of Nanoelectronics, Höfflinger, Bernd, Ed., Heidelberg, Springer-Verlag, (2012)293–314.

[2] McAdams, Eric, Claudine Gehin, Bertrand Massot, and James McLaughlin, “The Challenges Facing Wearable Sensor Systems,” in 9th International Conference on Wearable Micro and Nano Technologies for Personalized Health, Porto (2012)196–202.

[3] Sheikh Akbar, Prabir Dutta, and Chonghoon Lee, High-Temperature Ceramic Gas Sensors: A Review, Int. J. Appl. Ceram. Technol., 3 (4) (2006)302–311

[4]. T. G. Nenov and S. P. Yordanov, Ceramic Sensors, Technology and Applications, Technomic Publishers, Lanscaster, (1996)138-144.

[5] Fraden, Jacob, Handbook of Modern Sensors, 4th ed. New York: Springer (2010).

[6] Chen, K. Y., K. F. Janz, W. Zhu, and R. J. Brychta, “Redefining the roles of sensors in objective physical activity monitoring,” Medicine and Science in Sports and Exercise, 44 (2012)13.

[7] Terms and Definitions in Industrial Process Measurement and Control, (IEC draft 65/84) International Electrotechnical Committee (1982).

[8] Stetter, J.R.; Penrose, W.R.; Yao, S. Sensors, Chemical Sensors, Electrochemical Sensors and ECS. J. Electrochem. Soc., 150 (2003) S11.

[9] Carr-Brion, K. Moisture Sensors in Process Control; Elsevier Applied Science Publishers: London, UK (1986).

[10] Z. Chen and C. Lu, Humidity Sensors: A Review of Materials and Mechanisms, Sensor Lett., 3(4) (2005)274–295.

[11] F. C. Quinn, The most common problem of moisture/humidity measurement and control. In: Moisture and Humidity, Proceedings of the 1985 International Symposium on Moisture and Humidity. Chaddock, J. B. ed., ISA, Washington, DC (1985)1–5.

[12] E. F. Carter, ed. Dictionary of Inventions and Discoveries. Crane, Russak and Co., New York, 1966. 3. Baughman E. H. and Mayes, D. NIR applications to process analysis. Am. Lab., 21(10) (1989)54–58.

[13] P. T. Moseley, J. O. W. Norris and D. E. Norris, Techniques and mechanisms in gas sensing, Adam Hilger Bristol, Philadelphia and New York (1991)189-190.

[14] Artiola, J.F., Pepper, I.L., Brusseau, M. (Eds.). Environmental Monitoring and Characterization. Burlington, MA: Elsevier Academic Press (2004).

[15] G.B. Wiersma, (Ed.) Environmental Monitoring. Boca Raton, FLA: CRC Press (2004).

[16] B. Mitchell, Resource and Environmental Management (2nd Ed.). Harlow: Pearson Education Limited (2002).

[17] Lovett, G.M., Burns, D.A., Driscoll, C.T., Jenkins, J.C., Mitchells, M.J., Rustad, L., Shanley, J.B., Likens, G.E., Haeuber, R., Who needs environmental monitoring?, J. Front. Ecol. Environ., 5(5) (2007)253-260.

[18] Conrad, C. and Daoust, T.,"Community-Based Monitoring Frameworks: Increasing the Effectiveness of Environmental Stewardship" J. Environ. Manage. 41(3):(2008)358-388

[19] Lindenmayer, D.B., Likens, G. E. Adaptive monitoring: a new paradigm for long-term research and monitoring. J. Trends Ecol. E vol.24 (9) (2009)482-486.

[20] De Blij, H.J., Muller, P.O., Williams, R.S., Conrad, C., Long, P. Physical Geography: the Global Environment. Don Mills, ONT: Oxford University Press (2005).

[21] Vaughan, H., Brydges, T., Fenech, A., Lumb, A., Monitoring long-term ecological changes through the Ecological Monitoring and Assessment Network: Science-based and policy relevant. J. Environ. Monit. Assess., 67 (2001)3–28.

[22] Norton, H. N. Handbook of Transducers. Prentice-Hall, Englewood Cliffs, NJ (1989).

[23] White, R. W. A sensor classification scheme. In: Microsensors. IEEE Press, New York (1991)3–5.

[24] Jones, Deric P., Biomedical Sensors, 1st Ed. New York: Momentum Press (2010).

[25] Otto M. , Analytische Chemie. VCH, Weinheim New York (1995).

[26] Schwedt G., Analytische Chemie. Thieme, Stuttgart (1995)

[27] Wolfbeis OS Fresenius J Anal Chem., (1990)337:522.

[28] Fraden Jacob, Modern Sensors Handbook – Physics, Designs and Applications, American Institute of Physics, NY, (1996)542.

[29] Vandrish G., Ceramic applications in gas and humidity sensors. Key Eng Mater 122–124: (1996)185–224.

[30] T.A. Blanka, L.P. Eksperiandova, K.N. Belikov, Recent trends of ceramic humidity sensors development: A review. Sensors and Actuators B 228: (2016)416–442.

[31] Comini E, Faglia G, Sberveglieri G., Electrical-based gas sensing. In: Comini E, Faglia G, Sberveglieri G (eds) Solid state gas sensing. Springer, New York, (2009)47–107.

[32] Korotcenkov G., Cho BK Methods of sensing materials synthesis and deposition. In: Chemical sensors: fundamentals of sensing materials, vol 1, General approaches. Momentum, New York, NY (2010) 214–303.

[33] Song K-H, Park SJ Factors determining the carbon monoxide sensing properties of tin oxide thick film calcined at different temperatures. J Am Ceram Soc 77: (1994)2935–2939.

[34] R. E. Grim, H. Kodama, www.britannica.com, 24/12/2015.

[35] Grim, R.E., Clay Mineralogy, 2nd Ed. McGraw-Hill Book Company, NY(1968).

[36] Wyckoff, R.W.G., Crystal Structures, vol. 4. John Wiley and Sons, New York (1968).

[37] Pinnavaia, T.J., Intercalated clay catalysts. Science 220 (1983)365–371.

[38] Garrido-Ramírez EG, Theng BKG, Mora ML., Clays and oxide minerals as catalysts and nanocatalysts in Fenton-like reactions a review. Appl Clay Sci., 47 (2010)182–92.

[39] Carretero MI, Pozo M. Clay and non-clay minerals in the pharmaceutical industry: Part I. Excipients and medical applications. Appl Clay Sci; 46: (2009)73–80.

[40] Carretero MI, Pozo M., Clay and non-clay minerals in the pharmaceutical and cosmetic industries Part II. Active ingredients. Appl Clay Sci , 47 (2010)171–81.

[41] Murray HH. Traditional and new applications for kaolin, smectite, and palygorskite: a general overview. Appl Clay Sci., 17 (2000)207.

[42] F. A. Mumpton and R. Roy, new data on sepiolite and attapulgite, clays and Clay Minerals 5 (1956)136-143.

[43] Serdyuchenko, D. P., Sepiolite from northern Caucasus: Doklady Acad. Nauk S.S.S.R., 69 (1949)577-580.

[44] LaCroix A., Les transformations min&alogiques secondaires observ~es dans les gisements de phlogopite de l'extreme-sud de Madagascar: Compt. Rend. Acad. Sci., 210 (1940)353-357.

[45] Singer A., Palygorskite and sepiolite group minerals. In: Minerals in Soil Environments (S.B. Weed & J.B. Dixon). 2nd Ed. Soil Sci. Soc. Am. Pub. Madison, (1989)829-872.

[46] S. A. McLean, B.L. Allen, and J.R. Craig, the occurrence of sepiolite and attapulgite on the southern High Plains, Clays and Clay Minerals 20 (1972) 143-149.

[47] J. Ralph, www.mindat.org, 18/10/2015.

[48] A. Torro-Palau and J. C. Fernandez-Garcia, A. C. Orgiles-Barcelo, M. M. Pastor-Bias and J. M. Martin-Martinez, Structural modification of sepiolite (natural magnesium silicate) by thermal treatment: effect on the properties of polyurethane adhesives, Int. J. Adhesion and Adhesives 17 (1997)111-119.

[49] H. Kodama, www.britannica.com, 18/10/2015.

[50] C. Beaugera, G. Lainéa, A. Burrb, A. Taguetc, B. Otazaghinec, A. Rigaccia, Nafion–sepiolite composite membranes for improved proton exchange membrane fuel cell performance, Journal of Membrane Science 430 (2013)167–179.

[51] R. E. Grim, H. Kodama, www.rsminerals.co.uk, 20/10/2015.

[52] M. A. Jr., R. C. Chianelli, and R. M. Arrowood, Computational Study of the Structure of a Sepiolite / Thioindigo Mayan Pigment, Bioinorganic Chemistry and Applications, (2012)1-6.

[53] S.K. Deb, Opportunities and challenges in science and technology of WO_3 for electrochromic and related applications, Solar Energy Materials and Solar Cells, 92 (2008)245–258.

[54] R. Sivakumar, A. Moses, Ezhil Raj, B. Subramanian, M. Jayachandran, D.C. Trivedi, C. Sanjeeviraja, Preparation and characterization of spray deposited n-type WO_3 thin films for electrochromic devices, Bulletin of Materials Science 39 (2004)1479.

[55] J. Zhang, X.L. Wang, X.H. Xia, C.D. Gu, J.P. Tu, Electrochromic behavior of WO_3 nanotree films prepared by hydrothermal oxidation, Solar Energy Materials and Solar Cells, 95 (2011)2107–2112.

[56] C. Chananonnawathorn, S. Pudwat, M. Horprathum, P. Eiamchai, P. Limnontakul, C. Salawan, K. Aiempanakit, Electrochromic property dependent on oxygen gas flow rate and films thickness of sputtered WO_3 films, Procedia Engineering, 32 (2012)752–758.

[57] K. Paipitak, C. Kahattha, W. Techitdheera, S. Porntheeraphat, W. Pecharap, Characterization of sol–gel derived Ti-doped tungsten oxide electrochromic thin films, Energy Procedia 9 (2011)446–451.

[58] W. Li, J. Li, X. Wang, S. Luo, J. Xiao, Q. Chen, Visible light photoelectrochemical responsiveness of self-organized nanoporous WO_3 films, Electrochimica Acta 56 (2010)620–625.

[59] W. Li, J. Li, X. Wang, J. Ma, Q. Chen, Photoelectrochemical and physical properties of WO_3 films obtained by the polymeric precursor method, International Journal of Hydrogen Energy 35 (2010)13137–13145.

[60] C. Zhang, A. Boudiba, C. Navio, C. Bittencourt, M.G. Olivier, R. Snyders, M. Debliquy, Highly sensitive hydrogen sensors based on co-sputtered Platinum activated tungsten oxide films, International Journal of Hydrogen Energy 36 (2011)1107–1114.

[61] C. Zhang, O. Van Overschelde, A. Boudiba, R. Snyders, M.G. Olivier, M. Debliquy, Improvement of sensing characteristics of radio-frequency sputtered tungsten oxide films through surface modification by laser irradiation, Materials Chemistry and Physics 133 (2012)588–591.

[62] C. Zhang, M. Debliquy, A. Boudiba, H. Liao, C. Coddet, Sensing properties of atmospheric plasma-sprayed WO_3 coating for sub-ppm NO_2 detection, Sensors and Actuators B 144 (2010)280–288.

[63] A. Boudiba, C. Zhang, C. Navio, C. Bittencourt, R. Snyders, M. Debliquy, Preparation of highly selective, sensitive and stable hydrogen sensors based on Pd-doped tungsten trioxide, Procedia Engineering 5 (2010)180–183.

[64] C. Zhang, A. Boudiba, C. Navio, M.G. Olivier, R. Snyders, M. Debliquy, Study of electivity of NO_2 sensors composed of WO_3 and MnO_2 thin films grown by radio frequency sputtering, Sensors and Actuators B 161 (2012)914–922.

[65] R. Calavia, A. Mozalev, R. Vazquez, I. Gracia, C. Cané, R. Ionescu, E. Llobet, Fabrication of WO_3 nanodot-based microsensors highly sensitive to hydrogen, Sensors and Actuators B 149 (2010)352–361.

[66] S. Vallejos, T. Stoycheva, P. Umek, C. Navio, R. Snyders, C. Bittencourt, E. Llobet, C. Blackman, S. Moniz, X. Correig, Au nanoparticle-functionalised WO_3 nanoneedles and their application in high sensitivity gas sensor devices, Chemical Communications 47 (2011)565–567.

[67] T.S. Kim, Y.B. Kim, K.S. Yoo, G.S. Sung, H.J. Jung, Sensing characteristics of dc reactive sputtered WO_3 thin films as an NO_x gas sensor, Sensors and Actuators B 62 (2000)102–108.

[68] K. Aguir, C. Lemire, D.B.B. Lollman, Electrical properties of reactively sputtered WO_3 thin films as ozone gas sensor, Sensors and Actuators B 84 (2002)1–5.

[69] A. Labidi, C. Jacolin, M. Bendahan, A. Abdelghani, J. Guérin, K. Aguir, M. Maaref, Impedance spectroscopy on WO_3 gas sensor, Sensors and Actuators B 106 (2005)713.

[70] F. Bender, C. Kim, T. Mlsna, J.F. Vetelino, Characterization of a WO_3 thin film chlorine sensor, Sensors and Actuators B 77 (2001)281–286.

[71] M. Hübner, C.E. Simion, A. Haensch, N. Barsan, U. Weimar, CO sensing mechanism with WO_3 based gas, Sensors and Actuators B 151 (2010)103–106.

[72] J.K. Srivastava, P. Pandey, V.N. Mishra, R. Dwivedi, Sensing mechanism of Pd doped SnO_2 sensor for LPG detection, Solid State Sciences 11 (2009)1602–1605.

[73] N. Barsan, U. Weimar, Conduction model of metal oxide gas sensors, Journal of Electroceramics 7 (2001)143–167.

[74] D. Kohl, The role of noble metals in the chemistry of solid-state gas sensor, Sensors and Actuators B 1 (1990)158–165.

[75] P. P. Sahay, Zinc oxide thin film gas sensor for detection of acetone, Journal of Materials Science 40 (2005)4383–4385.

[76] http://www.fhi-berlin.mpg.de/KH, 25/10/2015.

[77] H. B. Wu, J. S. Chen, H. H. Hng, X. W. Lou, Nanostructured metal oxide-based materials as advanced anodes for lithium-ion batteries, Nanoscale, 4 (2012)2526–2542.

[78] T. Yu, Y. Zhu, X. Xu, K.S. Yeong, Z. Shen, P. Chen, C.T. Lim, J.T.L. Thong, C.H. Sow, Simple nanoscience: Substrate-friendly synthesis of metal oxide nanostructures using a hotplate, Small 2 (2006)80.

[79] J. Chen, L. Xu, W. Li, X. Gou, α-Fe_2O_3 Nanotubes in Gas Sensor and Lithium-Ion Battery Applications, Adv. Mater. 17 (2005)582-586.

[80] J. Sarradin, A. Guessous, M. Ribes, J., Synthesis and characterization of lithium intercalation electrodes based on iron oxide thin films, Power Sources 62 (1996)149-154.

[81] J. Morales, L. Sánchez, F. Martín, F. Berry, X. Ren, J., Synthesis and characterization of nanometric iron and iron-titanium oxides by mechanical milling: electrochemical properties as anodic materials in lithium cells, Electrochem. Soc. 152 (2005)A1748.

[82] D. Larcher, D. Bonnin, I. Rivals, L. Personnaz, J.-M. Tarascon, Combined XRD, EXAFS, and Mössbauer Studies of the Reduction by Lithium of α-Fe_2O_3 with Various Particle Sizes, J. Electrochem. Soc. 150 (2003)A1643.

[83] M.V. Reddy, T. Yu, C.-H. Sow, Z. Shen, C.T. Lim, G.V. Subba Rao, B.V.R. Chowdari, α- Fe_2O_3 nanoflakes as an anode Material for Li-ion batteries, Adv. Funct. Mater. 17 (2007)2792.

[84] Huang, Bo; Tai, Kaiping; Dillon, Shen J, Structural evolution of α-Fe_2O_3 nanowires during lithiation and delithiation, Journal of Power Sources 245 (2014)308-314.

[85] S. Wang, Li Wang, T. Yang, X. Liu, J. Zhang, B. Zhu, S. Zhang, W. Huang, S. Wu, Porous α-Fe_2O_3 hollow microspheres and their application for acetone sensor, Journal of Solid State Chemistry 183 (2010)2869–2876.

[86] L. Huo, Q. Li, H. Zhao, L. Yu, S. Gao, J. Zhao, Solgel route to pseudo cubics haped α-Fe_2O_3 alcohol sensor: preparation and characterization, Sensors and Actuators B107(2005)915–920.

[87] S. Y. Wang, W. Wang, W. Z. Wang, Z. Jiao, J. H. Liu, Y. T. Qian, Characterization and gas- sensing properties of nanocrystalline iron (III)oxide films prepared by ultrasonic spray pyrolysis on silicon, Sensors and Actuators B69(2000)22–27.

[88] E. T. Lee, G. E. Jang, C. K. Kim, D. H. Yoon, Fabrication and gas sensing properties of α-Fe_2O_3 thin film prepared by plasma enhanced chemical vapor deposition (PECVD), Sensors and Actuators B77 (2001)221–227.

[89] Q. Hao, L. Li, X. Yin, S. Liu, Q. Li, T. Wang, Anomalous conductivity-type transition sensing behaviors of n-type porous α-Fe_2O_3nanostructures toward H_2S, Materials Science and Engineering B176(2011)600–605.

[90] S. T. Navale, D. K. Bandgar, S .R. Nalage, G. D. Khuspe, M. A. Chougule, Y. D. Kolekar, S. Sen and V. B. Patil, Synthesis of Fe_2O_3 nanoparticles for nitrogen dioxide gas sensing applications, Ceramics International 39 (6) (2013)6453-6460.

[91] J. Zaanen, G. A. Sawatzky and J. W. Allen, “Band Gaps and Electronic Structure of Transition-Metal Compounds”, Phys. Rev. Lett.55 (1985)418.

[92] G. Yanfeng, N. Masayuki, Morphology Evolution of ZnO Thin Films from Aqueous Solutions and their application to solar cells, Langmuir 22 (2006)3936–3940.

[93] S. Ghosh, P. Srivastava, B. Pandey, S. Maurav, P. Bharadwaj, D. K. Avasthi, D. Kabiraj, S.M. Shivaprasad, Study of ZnO and Ni-doped ZnO synthesized by atom beam sputtering technique, Applied Physics A 90 (2008)765–769.

[94] S. Mochizuki, Electrical conductivity of α-Fe_2O_3, Phys. Status Solidi 41(2)(1977) 591-594.

[95] Y. Guo, S. J. Clark and J. Robertson, Electronic and magnetic properties of Ti_2O_3, Cr_2O_3, and Fe_2O_3 calculated by the screened exchange hybrid density functional, J. Phys.: Condens. Matter 24 (2012)325504.

[96] M. Egashira, M. Nakashima, S. Kawasumi and T. Seiyama, Temperature programmed desorption study of water adsorbed on metal oxides, Bulletin of the Chemical Society of Japan 51 (1978)3144-3149.

[97] Y. Shimizu, H. Ichinose, H. Arai and T. Seiyama, Ceramic humidity sensors: Microstructure and simulation of humidity sensitive characteristics, J. Chem. Soc. Jpn., (1985)1270-1277.

[98] J. H. Anderson and G. A. Parks, The electrical conductivity of silica gel in the presence of adsorbed water, Z Phys. Chem., 72(1968)3362-3368.

[99] H. T. Sun, M. T. Wu, P. Li and X. Yao, Porosity control of humidity-sensitive ceramics and theoretical model of humidity sensitive characteristics, Sensors and Actuators, 19 (1989)61-70.

[100] T. Suzuki and N. Matsui, Properties of humidity sensitive oxides with alkali additive, in T. Seiyama, K. Fueki, J. Shiokawa and S. Suzuki (eds.),Chemical Sensors, Kodansha, Tokyo/Elsevier, Amsterdam, 17 (1983)381-386.

[101] T. Y. Kim, D. H. Lee, Y. C. Shim, J. U. Bu and S. T. Kim, Effects of alkaline oxide additives on the microstructure and humidity sensitivity of $MgCr_2O_4$-TiO_2, Sensors and Actuators B, 9(1992)221-225.

[102] Y. Sadaoka, Y. Sakai and S. Mitsui, Humidity sensor using zirconium phosphates and silicates. Improvements of humidity sensitivity, Sensors and Actuators, 13 (1988)147-157.

[103] T. Seiyama, N. Yamazoe and H. Arai, Ceramic humidity sensors, Sensors and Actuators, 4 (1983)85-96.

[104] Y.Shimizu, M. Shimabukuro, H. Arai and T. Seiyama, Humidity- sensitive characteristics of La^{3+}-dope d and undoped $SrSnO_3$, J. Electrochem. Soc., 136 (1989)1206-1210.

[105] T. Usui, Y. Kurumiya, K. Nuri and M. Nakazawa, Gaspolarographic multifunctional sensor: oxygen-humidity sensor, Sensors and Actuators, 16 (1989)345-358.

[106] H. Yagi and K. Ichikawa, Humidity sensing characteristics of a limiting current type planar oxygen sensor for high temperatures, Sensors and Actuators B, 13 (1993)92.

[107] H. Yagi and K. Ichikawa, High temperature humidity sensor using a limiting current type plane oxygen sensor, J. Cerant Soc. Jpn., 100 (1992)282-286.

[108] H. Yagi and K. Horii, Humidity sensing characteristics of a limiting current type plane oxygen sensor in high temperature environment, Denki Kagaku, 60 (1992)220.

[109] E. Traversa, Ceramic sensors for humidity detection: the state-of-the-art and future developments, Sensors and Actuators B, 23 (1995)135-156.

Chapter two:

Elaboration and characterization of modified sepiolites and their humidity sensing features for environmental monitoring

Abstract

After precipitation under basic conditions and subsequent thermal treatment, different oxide/hydroxide nanoparticles (based on W^{4+}, Co^{2+}, Cu^{2+}, Gd^{3+}, La^{3+}, Mn^{2+}, Nd^{3+}, Sm^{3+}, Sr^{2+}, Y^{3+} and Zn^{2+}) were formed onto sepiolite grains. Thermogravimetric-Differential Thermal Analysis (TG-DTA) combined with X-Ray Diffraction (XRD), nitrogen adsorption at -196°C, Field Emission-Scanning Electron Microscopy (FE-SEM), Diffuse Reflectance UV-visible (DR-UV-vis) spectroscopy and Infra-Red (IR) spectroscopy were used to study both the particle size distribution, the morphology and the composition of the modified sepiolites.

Humidity sensors were prepared in the form of pellets, where powders were uniaxially pressed and thermally treated at 550°C for 1 h then, gold electrodes were screen-printed. Among the different studied compositions, tungsten-doped sepiolite with ratio of 15% that substituted the magnesium ions into the structure of sepiolite exhibited a significant response towards relative humidity (RH) at room temperature starting from 40% RH.

2.1 Introduction

Precipitation of metal ions onto clay minerals has been studied extensively because both metal ions and clays are easily found in nature and also because modified clays can be useful for different applications such as highly sensitive gas and humidity sensors, and environmental remediation of water polluted by heavy metal ions [1]. However, there are few papers dealing with clays for such specific applications [2-4]. By considering the large deposits of clay minerals, it is economically favorable to use clays as metal ions supports.

Sepiolite is a micro-fibrous clay (it is a hydrous magnesium silicate having the chemical formula $Mg_8Si_{12}O_{30}(OH)_4(H_2O)_4.8H_2O$). Sepiolite structural units are composed of two tetrahedral silica sheets and a discontinuous central layer of octahedral magnesium oxide. This gives rise to the formation of open channels with dimensions of 0.36 × 1.06 nm. It has a large external specific surface area (SSA) out of the channels (ca. 320 m^2g^{-1}) [5]and a low cation exchange capacity (CEC). The measured values of SSA are far from the calculated theoretical values, even when molecules smaller than N_2 are used as adsorbent, as the accessibility to the intra-crystalline tunnels is restricted both by the relative size of N_2 and the tunnels, and by the presence of the zeolitic water filling the tunnels[6].It has been found that when the fraction of Mg^{2+}cations leached from sepiolite (α) is greater than or equal to 0.33, the sepiolite crystalline structure collapses and an amorphous silica-based phase forms. This fact opens the possibility to obtain sepiolite with different substituted cations along octahedral sites (metal–sepiolite) [3]. Thus, the aim of this work is to substitute Mg^{2+} ions in sepiolite channels and to precipitate different oxide/hydroxide nanoparticles (based on W^{4+}, Co^{2+}, Cu^{2+}, Gd^{3+}, La^{3+}, Mn^{2+}, Nd^{3+}, Sm^{3+},

Sr^{2+}, Y^{3+} and Zn^{2+}) onto sepiolite grains. Microstructural characterization of the produced powders will be done by means of Thermogravimetric-Differential Thermal Analysis (TG-DTA) combined with X-Ray Diffraction (XRD), nitrogen adsorption at -196°C, Field Emission Scanning Electron Microscopy (FESEM), Diffuse Reflectance UV-visible (DR-UV-vis) spectroscopy and Infra-Red (IR) spectroscopy. Finally, the humidity sensing features of the synthesized powders will be evaluated and discussed on the basis of the doping element.

2. 2. Experimental

2.2.1. Materials

All the reagents were ACS grade from Sigma-Aldrich. Natural sepiolite mineral from Vicalvaro-Vallecas (TOLSA grade S9, Spain) was purified and micronized by a wet process to obtain a final product with a content of sepiolite higher than 95%, according to the producer. The resulting sepiolite needle-like particles have a length of 0.1 mm and a thickness of 10–30 nm [7]. The sepiolite powder was then dispersed at 10 wt% concentration in water by magnetic stirring. Acid leaching was done at pH equal to 0.00 by adding 37% HCl v/v for 2 h. The so obtained dispersion was vacuum filtered, washed several times with distilled water and the washed sample was then mixed with 1.0 L aqueous solution of the following salts (for precipitation of metal hydroxide): WCl_4, $Co(NO_3)_2.6H_2O$, $CuCl_2$, $Gd(NO_3)_2.6H_2O$, $La(NO_3)_2.6H_2O$, $Mn(NO_3)_2.4H_2O$, $Nd(NO_3)_2.6H_2O$, $Sm(NO_3)_2.6H_2O$, $Sr(NO_3)_2$, $Y(NO_3)_2.6H_2O$ and $Zn(NO_3)_2.6H_2O$. Their concentration was adjusted so that the final metal content in sepiolite was 15 wt% [8]. The pH of the dispersion was then adjusted with NaOH as reported in table 1.

Finally, the dispersion was vacuum filtered and washed with water, and then the filtration cake was dried at 115°C overnight. The obtained powder was heat treated at 550°C for1 h with a 2°C/min heating ramp. The calcined powder were uniaxially pressed at 300 MPa and interdigitated gold electrodes (ESL 520C, USA) were screen-printed. After drying, a second thermal treatment at 520°C for 20 min with a 2°C/min heating ramp was done to optimize the electrical conductivity of the electrodes, according to the ink's manufacturer recommendations.

No.	**Ions**	**pH value of precipitation**	**Ionic radius (pm)**
Reference	Mg^{2+}	-----	**89**
1	W^{4+}	10.0	66
2	Co^{2+}	9.0	65-74.5
3	Cu^{2+}	8.0	73
4	Gd^{3+}	8.0	93.8
5	La^{3+}	11.5	103.2
6	Mn^{2+}	9.0	67-83
7	Nd^{3+}	6.5	99.5
8	Sm^{3+}	6.5	96.4
9	Sr^{2+}	9.0	118
10	Y^{3+}	7.2	90
11	Zn^{2+}	8.0	74

Table 1. Precipitation pH of metal ions onto sepiolite and their ionic radius [9].

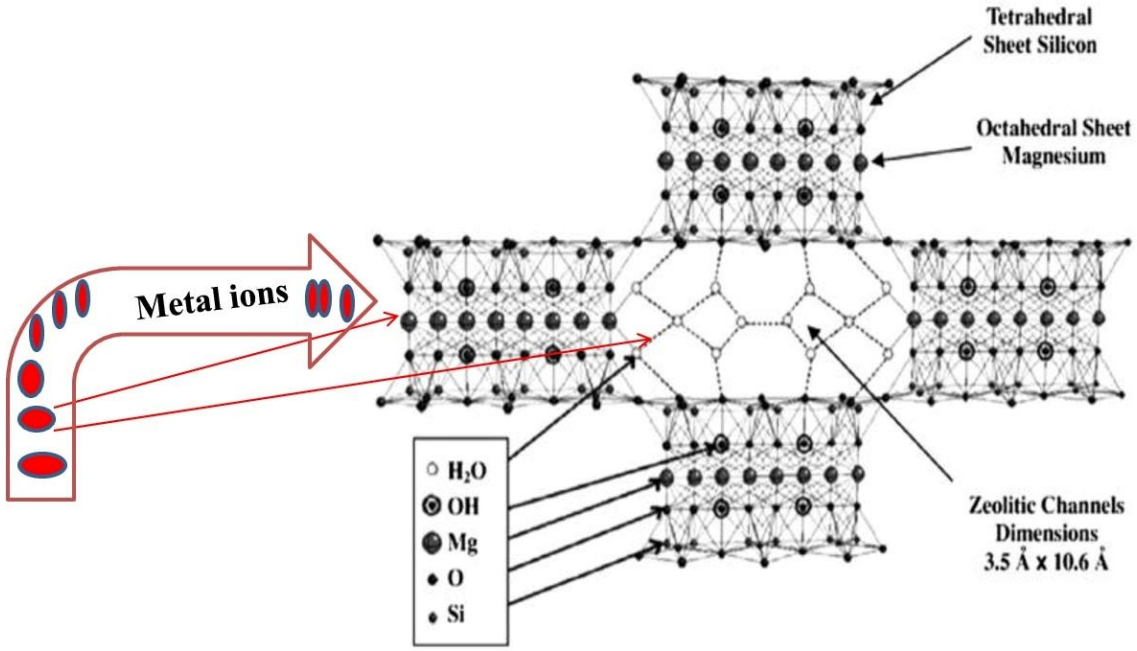

Fig. 1. Schematic representation of sepiolite structure and precipitation process

Humidity sensors were tested in a laboratory apparatus made of a thermostated chamber, operating at 25°C, in which RH could be varied between 0 and 96% [10]. The laboratory apparatus for sensors testing was calibrated to ensure a constant air flow during electrical measurements and relative humidity (RH) was varied by steps, each one of 3 min. An external alternating voltage (V = 3.6 V at 1 kHz) was applied on each tested sensor, acting as a variable resistance of the electrical circuit described above. The sensor response (SR), expressed in %, was defined as the relative variation of the starting resistance, compared with the resistance measured under gas exposure (eq. 1):

$$SR(\%) = 100\frac{|R_0 - Rg|}{R_0} \quad (1)$$

Where R_0 and R_g are the starting (in the absence of the test gas) and the gas exposed measured resistances of the sensors, respectively.

2.2.2. Methods

Particle size distribution was determined after powders calcination by means of a laser granulometer (Malvern 3600D) and after dispersion in ethanol and sonication for 10 min. X-ray diffraction patterns were collected on powders by means of a X'Pert High Score Philips Analytical Diffractometer, equipped with a Cu anticathode (λ Cu Kα anticathode = 0.154056 nm). Samples were scanned at a rate of 0.02°/s in the range 5° to 70° in 2θ.

About 50 mg of each powdered doped-sepiolite was also put in an opened platinum crucible for simultaneous thermogravimetric–differential thermal analysis (TG–DTA, Neztsch STA 409) and heated at 10°C/min up to 800°C, under static air.

Samples were uniaxially pressed in the form of thin, self-supporting wafers (optical density of about 20 $mg.cm^{-2}$) and studied in a standard vacuum frame (residual pressure below 10^{-3} mbar) in a home-made IR cell, equipped with KBr windows. Spectra were recorded at 2 cm^{-1}resolution on a Bruker Equinox 55 spectrophotometer equipped with a mercury cadmium telluride cryodetector. Specific Surface Area (SSA), total porous volume (Vp) and average pore diameter (Dp) were measured by N_2 physisorption at -196°C (Micrometrics ASAP 2020) on samples previously outgassed at 200°C for 4 h to remove water and other atmospheric contaminants. Samples specific surface area was calculated using the BET method and pore diameters were evaluated by applying the Barrett-Joyner-Halenda (BJH) algorithm to isotherms desorption branch.

Diffuse Reflectance (DR) UV–vis spectra on powder samples outgassed at room temperature were recorded on a Cary 5000 UV–vis-NIR spectrophotometer (Varian instruments).The morphology of the powders was first inspected by means of field emission scanning electron microscopy (FE-SEM, Zeiss Merlin)and then, by means of

high resolution electron transmission microscopy (HR-TEM) using a JEOL 3010-UHR instrument (acceleration potential: 300 kV; LaB6 filament), equipped with an Oxford INCA X-ray energy dispersive spectrometer (X-EDS) with a Pentafet Si(Li) detector. For FE-SEM and HR-TEM observations, the powders were deposited on carbon adhesive disks and chromium sputtered and ‘‘dry’’ dispersed on lacey carbon Cu grids, respectively.

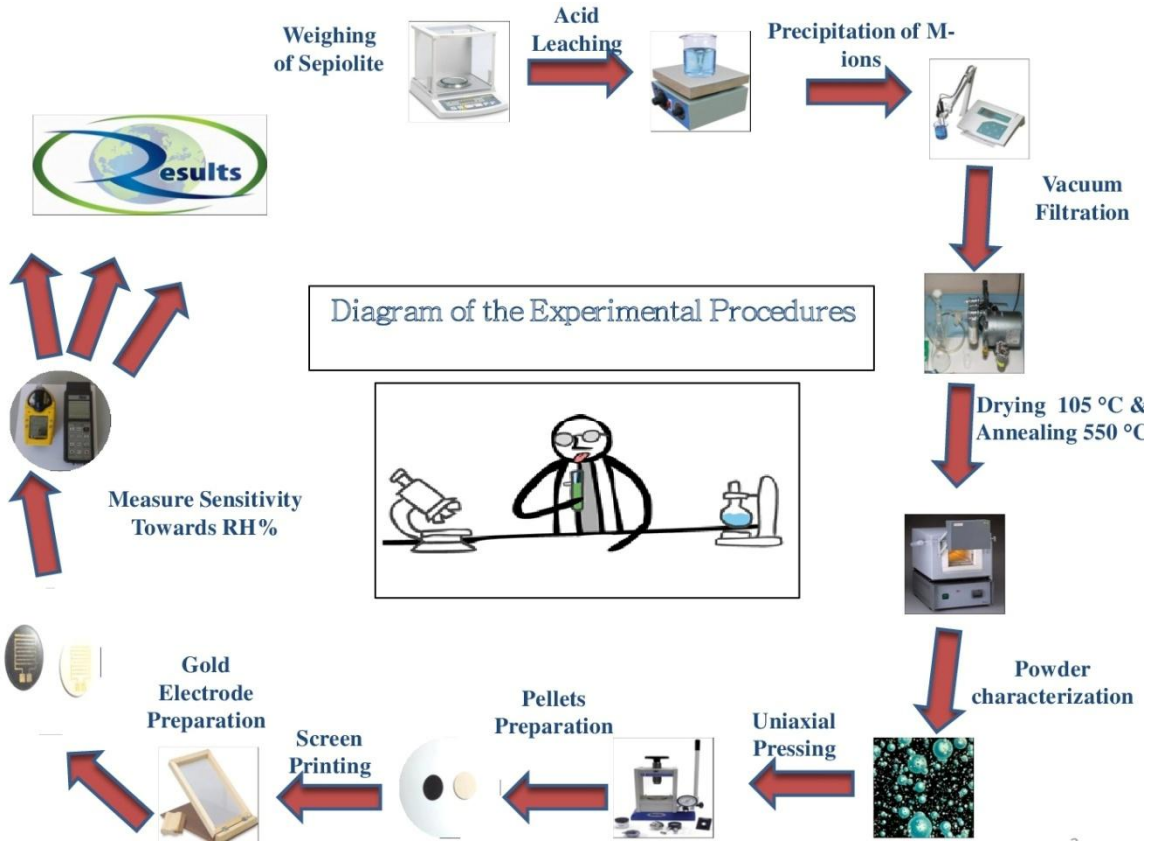

Fig. 2. Schematic diagram of the experimental procedures

2.3 Results and discussion

3.1. Materials characterization

3.1.1 Particle size distribution

Results showed that the thermal treated at 550°C for 1 h samples have a comparable or a larger particle size distribution with respect to pure sepiolite (Table 2). These results may be related to the particles agglomeration during leaching and washing, as the attachment force leading to the formation of agglomerates can be provided either by electrostatic or van der Waals forces or by material bridges developed through the use of a liquid which dried to form a solid bridge [11]. The observed differences in the measured diameters may be due to the different hydroxides formed during precipitation.

Cumulative wt%	**Pure sepiolite**	**W^{4+}**	**Co^{2+}**	**Cu^{2+}**	**Gd^{3+}**	**La^{3+}**	**Mn^{2+}**	**Sr^{2+}**	**Y^{3+}**	**Zn^{2+}**	**Nd^{+3}**	**Sm^{+3}**
10%	6.2	4.8	5.2	5.2	5.2	5.2	5.9	6.3	4.8	5.2	5.4	4.8
50%	16.3	11.6	15.6	15.8	14.9	22.9	20.0	19.6	14.9	15.8	15.4	14.22
90%	56.7	43.4	82.3	71.3	54.0	>136	108.9	111.4	51.9	65.4	50.52	48.48

Table 2. Diameter in micron of the metal ions doped-sepiolite powders.

2.3.1.2 XRD Characterization

XRD patterns of pure sepiolite as such and of pure sepiolite after 2 h of acid leaching and heat treated at 550°C for 1 h are reported on Fig. 3. The XRD pattern of the as received material is indexed on sepiolite JCPDS card 13-0595, while the leached heat treated sample is indexed on anhydrous sepiolite [12].

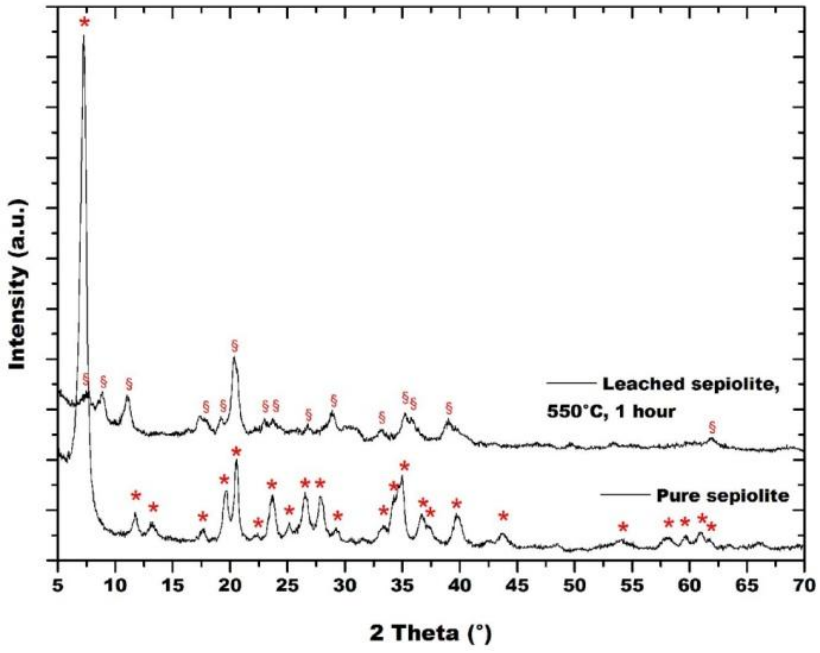

Fig. 3.XRD patterns of natural sepiolite as it is and after leaching, heat treated at 550°C (*: sepiolite, JCPDS card 13-0595; §: anhydrous sepiolite [12].

Acid treatment of sepiolite removes Mg^{2+} located in its octahedral layer but leaves Si^{4+} coordinated in its tetrahedral layer [13]. The Si-O-Mg-O-Si bond in sepiolite turns into two Si-O-H bonds after acid treatment with H_2SO_4 as illustrated in Fig. 4 [14].

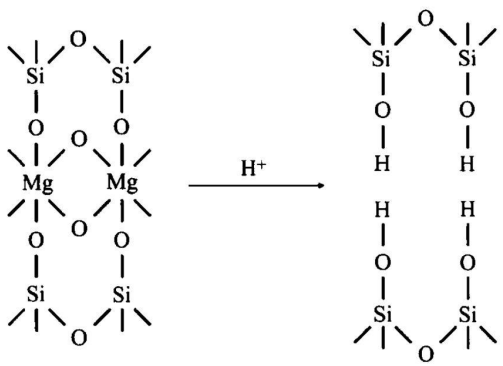

Fig. 4. **Sketch map of ion exchange in sepiolite during acid treatment [14].**

Therefore, the internal channels are enlarged, and the specific surface area becomes larger. When most magnesium ions are removed, part of micropores and mesopores expand to macropores. Nonetheless, acid treatment of sepiolite causes the formation of silica. When sepiolite is acid pre-treated and enough silica is formed, all the ribbons that conform the structure are not interconnected, because some of them have lost their octahedral sheet forming a layer structure [12]. So, a channel structure coming from the sepiolite crystal and a sheet structure corresponding to silica coexist in a singular fiber. Thus, only ribbons present on the channel structure have a tendency to fold, whereas unconnected neighboring silica do not participate in this process. Hence, the torque necessary to fold the structure is not applied, and therefore the crystal remains unfolded with the open channels but without the water of coordination (this fact stabilizes the structure of the original sepiolite) [12]. According to these experimental results, which concluded that an anhydrous sepiolite structure with nanosize channels was formed, in which, the coexistence of both sepiolite and silica in the same fiber was responsible for the thermal stabilization of the structure [12]. This novel structure of the sepiolite is of particular interest, since it can permit the insertion of other molecules into the channels; in our case, metal oxides.

The formation of the anhydride sepiolite structure is clearly evidenced when comparing both X-ray diffraction patterns of sepiolite, before and after the thermal treatment [12]. That is, several reflections, such as the reflection of the main peak of the pristine sepiolite that occurs at 1.200 nm (7.36° in 2θ, (110)) or reflections at 0.757 nm (11.68° in 2θ, (130)), 0.662 nm (13.36° in 2θ, (040)) and 1.970 nm (4.48° in 2θ, (060)) disappeared, whereas two new reflection peaks at 0.999 nm (8.84° in 2θ, (110)) and 0.795 nm (11.12°

in 2θ, (120)) corresponding to the folded monoclinic structure appear [12]. In this case, the reflection of the main peak occurs at 0.439 nm (20.21° in 2θ, (121)). The presence of both folded and unfolded sepiolite has been confirmed by XRD patterns are reported on Fig. 3. On the contrary, silica was not observed, probably because the amount formed was not sufficient to be detected by the instrument. It is also known in the literature that hydrochloric-, sulfuric-, or nitric-acid treatment at or below 80°C not only leaches Mg^{2+} from sepiolite, but also forms micro-pores, thereby increasing the specific surface area of sepiolite. The leached amount increases with the soaking time, temperature, and concentration of the acid, and the sepiolite phase disappears over time [13]. Fig.5. reports the XRD patterns of the investigated modified-sepiolite compositions.

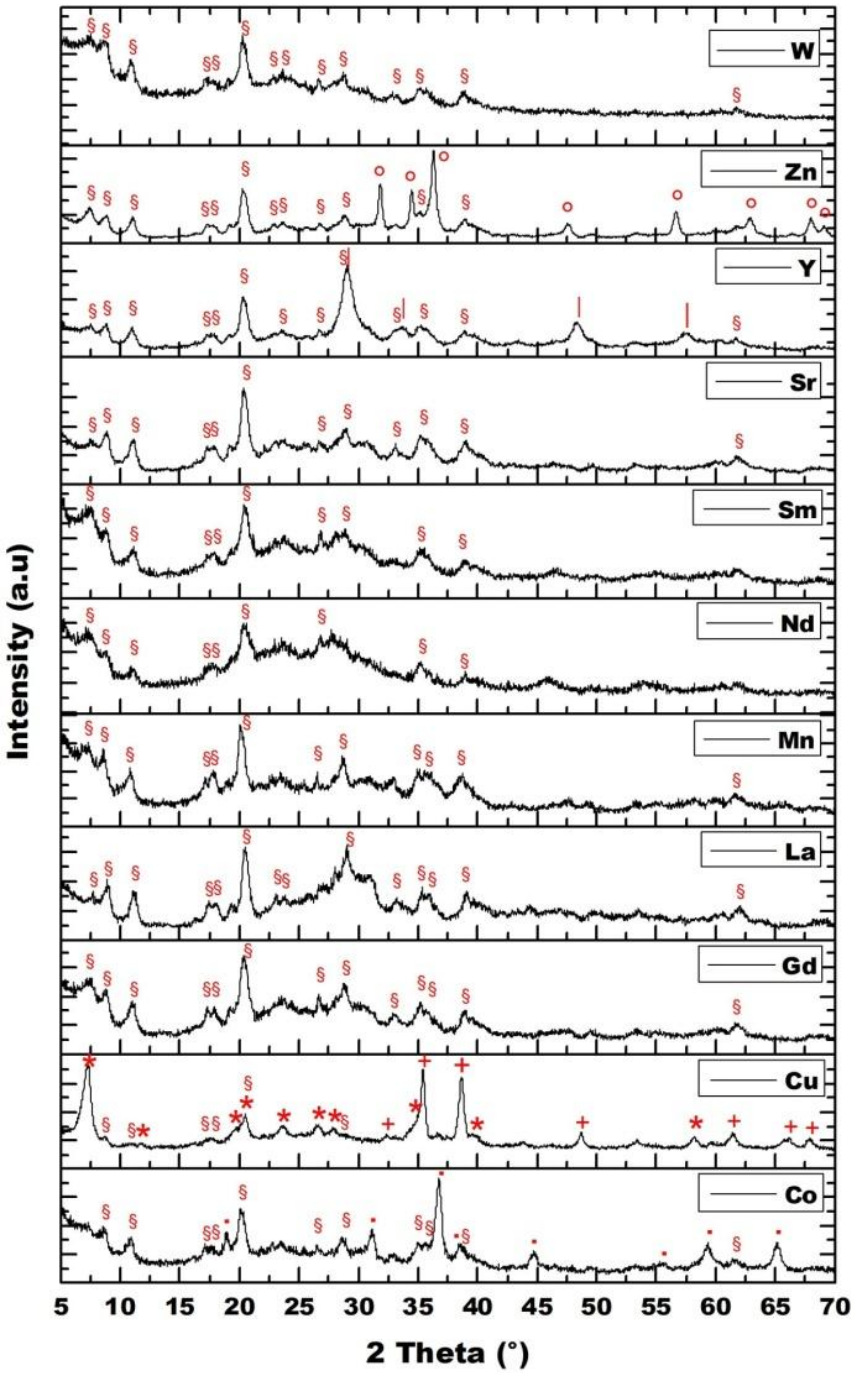

Fig. 5. XRD patterns corresponding to the different metal ions doped–sepiolite, heat treated at 550°C(*: sepiolite, JCPDS card 13-0595; §: anhydrous sepiolite[12]; Co_3O_4, JCPDS card 42-1467; +: CuO, JCPDS card 48-1548; |: Y_2O_3, JCPDS card 41-1105; °: ZnO, JCPDS card 36-1451).

No.	Compound	Temperature of formation	Reference
1	Strontium oxide	530-700°C (from decomposition of $Sr(OH)_2$)	[17]
2	Samarium Oxide	399-810°C (from samarium oxycarbonate)	[18]
3	Neodymium Oxide	400-600°C (from decomposition of $Nd(OH)_3$)	[19]
4	Manganese Oxide	>500°C (from Ni–Mn layered double hydroxide)	[20]
5	Lanthanum oxide	see text for details	[15]
6	Gadolinium oxide	>500°C (from gadolinium hydroxide)	[16]
7	Tungsten oxide	500°C (from WO_3 gel)	[21]

Table 3. Temperature of formation of different oxides.

Only in the case of cobalt, copper, yttrium and zinc additions, the corresponding oxide was evidenced on XRD patterns. This could be due to the temperature of formation of the oxide from their respective hydroxide, which is higher respect to the thermal treatment done in this work (Table 3) or because the formed phase is amorphous at the investigated temperature. In air, the path of dehydration of $La(OH)_3$ to A-La_2O_3 is a function of thermal history of the sample, as the thermal evolution of $La(OH)_3$ reflects the competition between dehydration and carbonation kinetics, and thus is highly dependent upon environment and experimental conditions [15]. The first dehydration step yields to LaOOH, but under relatively slow heating or long dwell times carbonation results in a full conversion of LaOOH to I and Ia-$La_2O_2CO_3$. The domain of existence of I-$La_2O_2CO_3$ is very narrow, from about 370 to 420°C, when it is assumed to convert to Ia phase. Upon heating, Iaoxycarbonate may either transform to form II or convert straightforward to La_2O_3. The occurrence of one or another phase will depend on dwell times used in the 500–600°C interval. II-$La_2O_2CO_3$, in turn, decomposes to A-La_2O_3 at 700°C [15]. However, none of these phases were detected by XRD. $Gd(OH)_3$dehydroxiles in $Gd_2O(OH)_4$ then in GdOOH, in the temperature range 157–327°C. However, GdOOH is an amorphous phase up to 500°C [16].

2.3.1.3 TG-DTA measurements

The thermal behavior of sepiolite has been extensively studied in literature [2, 12, 22-25] : in the first step, water superficially adsorbed and zeolitic water are removed up to 170°C (eq. 2), while, between 300 and 350°C, a half of the coordination water molecules is removed and the structure folds (eq. 3). These weight losses have been evidenced on pure sepiolite during thermal treatment, however, when sepiolite will rehydrate its structure

will also unfold [22]. When coordinated water is lost, a phase transformation takes place, folding the structure of the sepiolite. Consequently, the surface area of the sepiolite is reduced to half because the channels are collapsed [12]. The second half of the coordination water remains entrapped in the collapsed channels and is removed between 350 and 650°C (eq. 4), leading to the formation of anhydride sepiolite. In this case, the structure folding is irreversible at room temperature, even under 100% RH for three months [22]. Above 750-800°C, when dehydroxylation of Mg-OH occurs, the anhydride sepiolite transforms into enstatite (eq. 5).

$$Mg_8Si_{12}O_{30}(OH)_4.(H_2O)_4.8H_2O \rightarrow Mg_8Si_{12}O_{30}(OH)_4.(H_2O)_4 + 8H_2O \quad \text{(eq. 2)}$$

$$Mg_8Si_{12}O_{30}(OH)_4.(H_2O)_4 \rightarrow Mg_8Si_{12}O_{30}(OH)_4.(H_2O)_2 + 2H_2O \quad \text{(eq. 3)}$$

$$Mg_8Si_{12}O_{30}(OH)_4.(H_2O)_2 \rightarrow Mg_8Si_{12}O_{30}(OH)_4 + 2H_2O \quad \text{(eq. 4)}$$

$$Mg_8Si_{12}O_{30}(OH)_4 \rightarrow 8MgSiO_3 + 4SiO_2 + 2H_2O \quad \text{(eq. 5)}$$

The TG-DTA curve of acid-washed sepiolite is similar to the one of heated pure sepiolite, with a reduced weight loss below 170°C (Fig. 6a). This indicates that a certain amount of sepiolite channels remains unfolded in the sample after thermal treatment. The two weight losses observed in the sepiolite are attributed to superficial adsorbed water and partial dehydroxilation of Mg–OH groups. By comparing leached with modified sepiolite, it was found that all samples underwent only two weight losses (Fig. 6b), except for sepiolite modified with Cu (Fig. 6c) and Sr, where three steps of dehydration were identified.

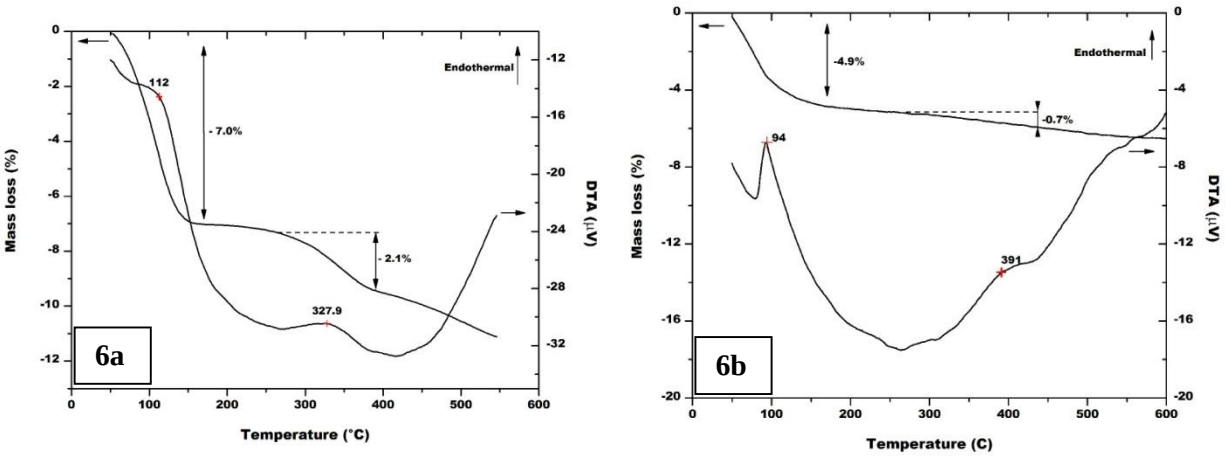

Fig. 6a.TG-DTA of acid-washed sepiolite and Fig. 6b.TG-DTA of tungsten-doped sepiolite.

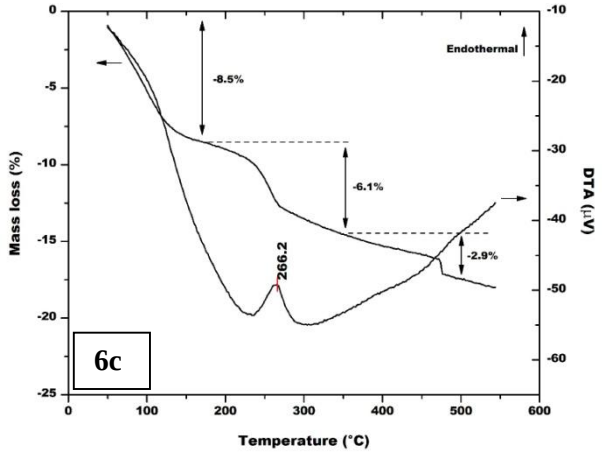

Fig. 6c.TG-DTA of copper-doped sepiolite

From the TG-DTA curve of tungsten-modified sepiolite (Fig. 6b), it was found that the second step of dehydration lays between 310 and 390°C. This delay may be due to the presence of tungsten species into the channels of sepiolite. The DTA curve in Fig. 6c is characterized by a large endothermic peakat 266°Cwhich corresponds to the dehydration of $Cu(OH)_2$ and the formation of CuO [26].

2.3.1.4 FE-SEM and HR-TEM observations and microanalysis

The surface morphologies of the treated powders were observed by FESEM as shown in Figs. 7a-d in which there is not a significant difference between the samples, before and after leaching and thermal treatment.

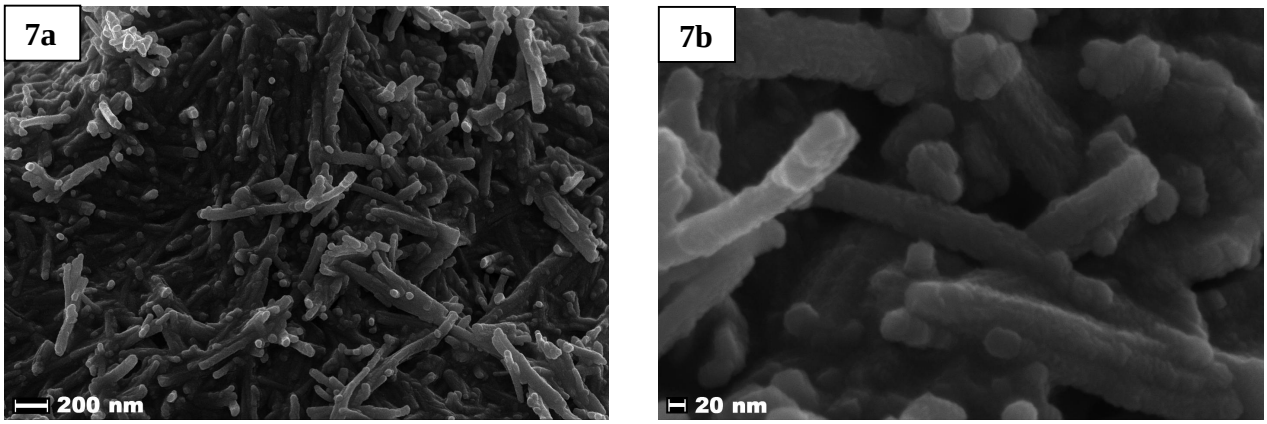

Fig. 7a and 7b. FESEM micrographs of sepiolite leached at pH 0 for 2 h and thermally treated at 550°C for 1h (magnification = 100,000× and 500,000× .

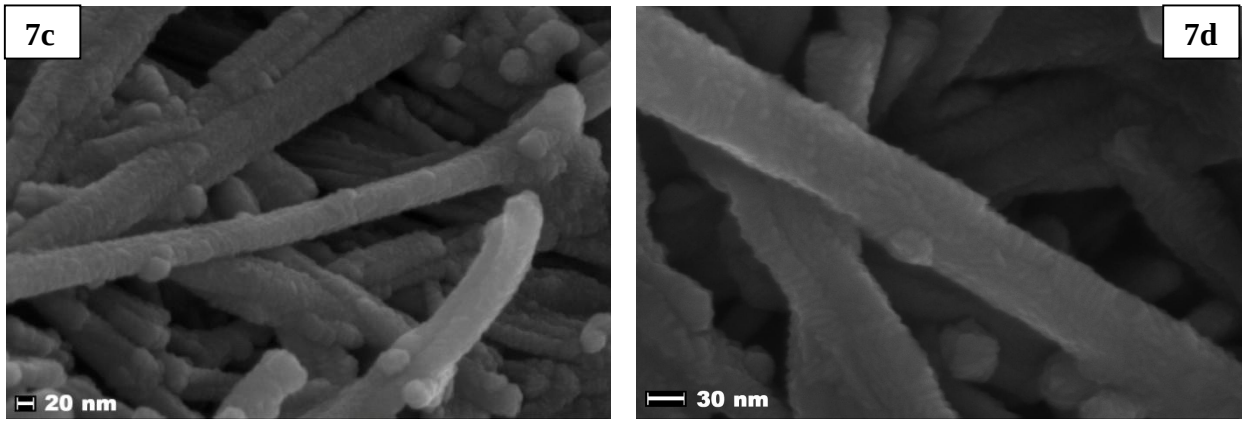

Fig. 7c. and 7d. FESEM micrograph of tungsten doped sepiolite thermally treated at 550°C for 1h (magnification = 500,000× and 750,000× respectively).

EDX maps of tungsten-doped sepiolite showed that Mg^{+2} and W^{4+} were well distributed in all the samples. Semi-quantitative elemental analysis (Table 4) indicated a tungsten content of 6.2 ±3.9 at% in the prepared powder.

Metals	At%
Mg	15.9±1.8
Si	77.9±2.8
W	6.2±3.9

Table 4. EDX analysis results of tungsten doped sepiolite sample.

HR-TEM observations showed that in Zn-doped sepiolite, ZnO nanoparticles were mostly located on the surface of sepiolite needles (Figs. 8a, b) and that their diameter was in the range 5-10 nm (Figs. 8c, d). Same results can be hypothesized for other dopants.

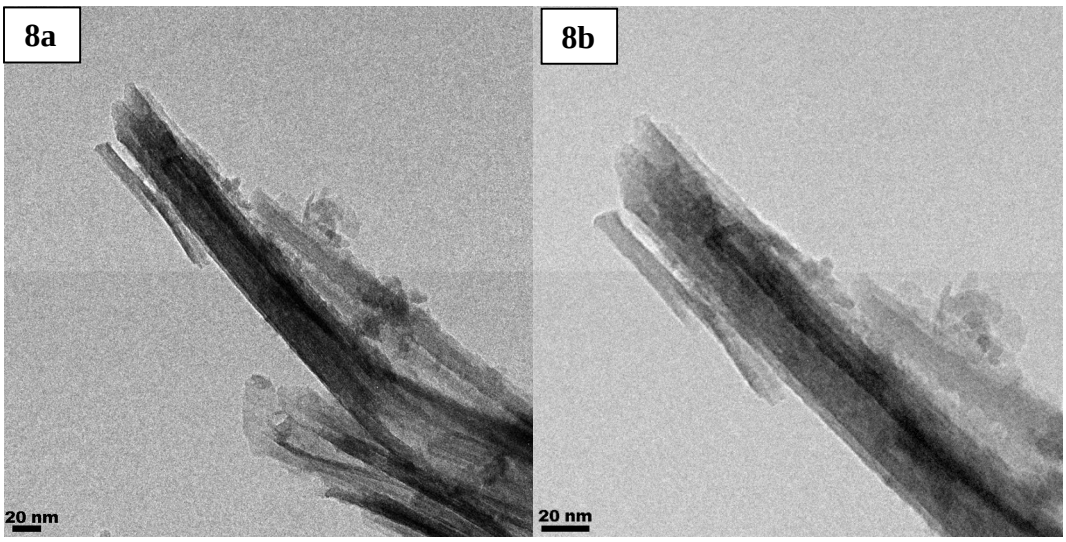

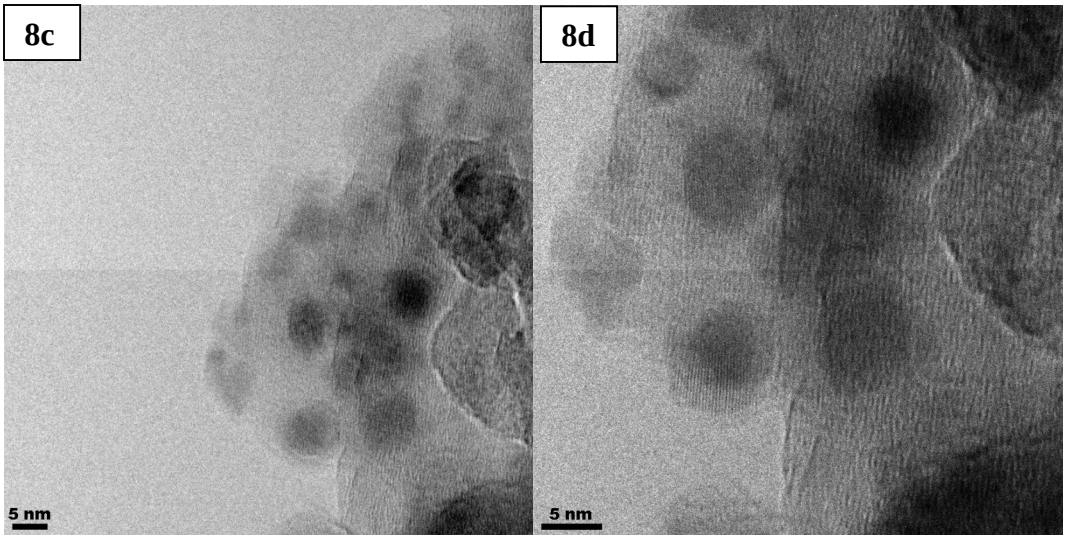

Fig. 8: HR-TEM micrographs of: acid-washed sepiolite (a, b), and detail of ZnO nanoparticles on an acid-washed sepiolite grain (c,d)

2.3.1.5 BET surface area and porosity

Specific Surface Area (SSA) decreases after leaching of sepiolite as shown in Table 5, whereas after doping, some tungsten oxo/hydroxides formed, as confirmed by UV-Vis spectroscopy that could contribute to the increase in SSA.

Sample	S.S.A. (m^2/g)	Porosity (cm^3/g)	Pore size (nm)
Leached sepiolite at 550°C	136	0.36	10
Tungsten doped sepiolite at 550°C	155	0.36	10

Table 5. Specific surface area of leached and tungsten doped sepiolite.

2.3.1.6- UV-Vis spectra

FIG. 9 reports UV-Vis spectra of leached sepiolite (curve S), tungsten and copper doped sepiolites (curves S+W and S+Cu, respectively). With respect to sepiolite, the tungsten doped sample showed two additional bands: that at 215 nm is ascribed to isolated WOx species, which according to the literature absorb at about 220 nm; the broad signal at higher wavelengths is composed by several bands, indicating the presence of clusters of tungsten oxides/hydroxides [27]. Similarly, the UV-Vis spectrum of the copper exchanged sepiolite shows a band at 267 nm, due to charge transitions from oxygen to isolated Cu^{2+} ions, and a broad absorption at higher wavelengths, due to the d-d transition of Cu^{2+} ions in copper oxo/hydroxides species [28].

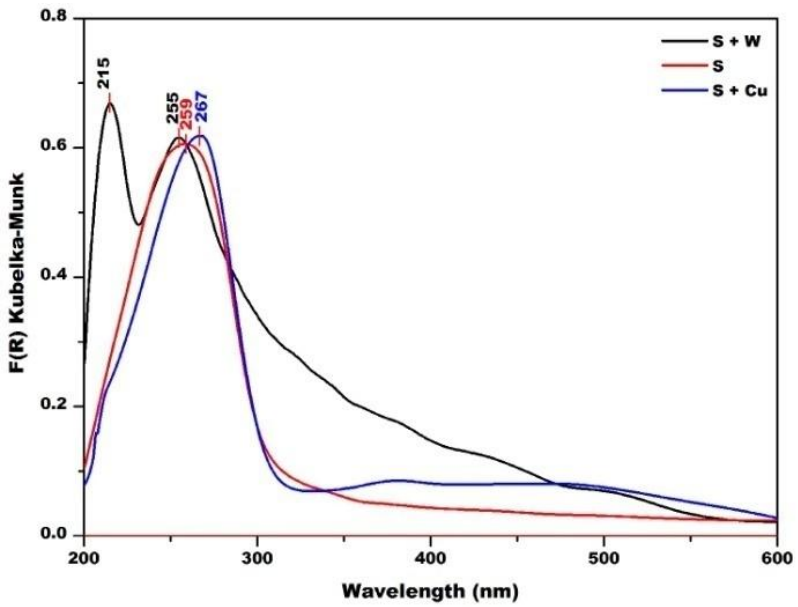

Fig. 9. UV-vis absorption spectra of leached sepiolite (S), tungsten doped sepiolite (S+W) and copper doped sepiolite (S+Cu).

2.3.1.7 FTIR measurements

FIG. 8 shows IR spectra of samples S and S+W: as a whole, the IR spectra of the prepared samples shows several absorptions bands in the 3800–3000 cm^{-1} region and a band at about 1660 cm^{-1}. The latter is assigned to the bending mode of molecular water: its intensity decreased within the S+W sample. In the OH stretching region (3800-3000 cm^{-1}) several bands were observed in (S) sample, assigned to several kinds of hydroxyl groups and the OH groups of water. After doping, these bands decreased in intensity, due to the reaction between hydroxyls and WOx species [29]. The same effect is observed with copper exchanged sepiolite.

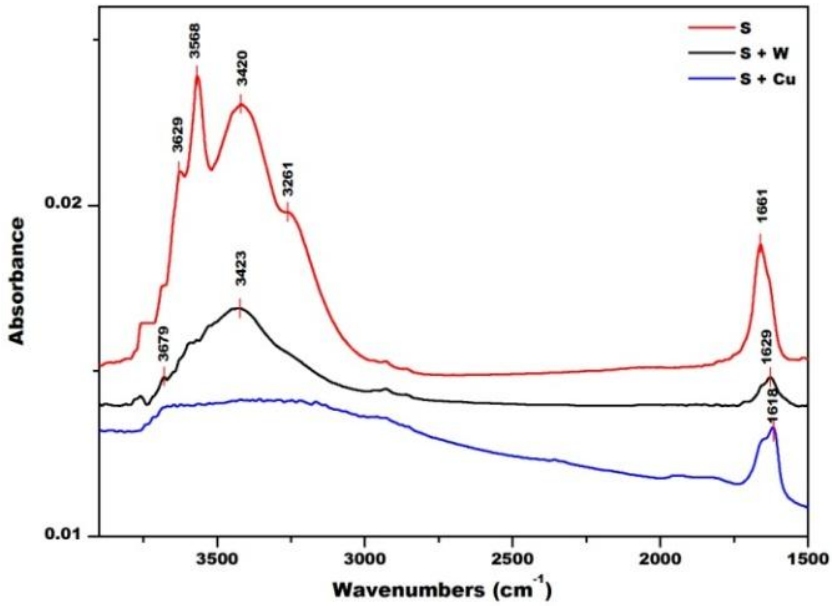

Fig. 10. IR spectra of the leached sepiolite (S), tungsten doped sepiolite (S+W) and copper doped sepiolite (S+Cu).

2.3.2 Sensitivity towards humidity

FIG. 11 and 12 illustrate the sensors' response to RH. Among the different investigated compositions, tungsten doped sensors showed a significant response towards humidity at room temperature starting from 40% RH. It is well known in the literature that water molecules chemisorb on the available sites of the oxide surface by a dissociative mechanism of the water molecules [30, 31].

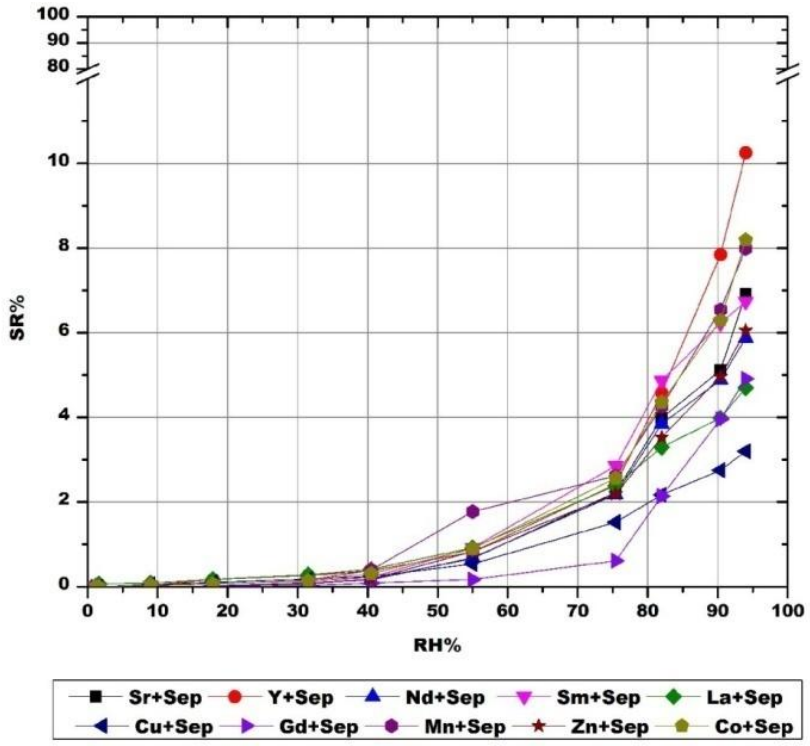

Fig. 11. Sensors response to RH after Co^{2+}, Cu^{2+}, Gd^{3+}, La^{3+}, Mn^{2+}, Nd^{3+}, Sm^{3+}, Sr^{2+}, Y^{3+} or Zn^{2+} ions precipitation onto sepiolite.

As already explained in Chapter 1, the hydroxyl groups adsorb on the metal cations and the protons react with an adjacent surface O^{2-} group to form a second OH^- group. Once formed, this chemisorbed layer is no more affected by surrounding humidity. At

temperatures lower than 100°C, subsequent layers of water molecules are physically adsorbed on the first hydroxyl layer when RH increases. Water molecules in the succeeding physisorbed layers are singly bonded, dissociate to H_3O^+ and form a liquid-like network. The conduction mechanism depends on the surface coverage of adsorbed water. When only hydroxyl ions are present on the oxide surface, the charge carriers are protons, from hydroxyl dissociation, which hop between adjacent hydroxyl groups. When water is present, while surface coverage is incomplete, H_3O^+ diffusion on hydroxyl groups dominates, but proton transfer between adjacent water molecules in clusters also takes place.

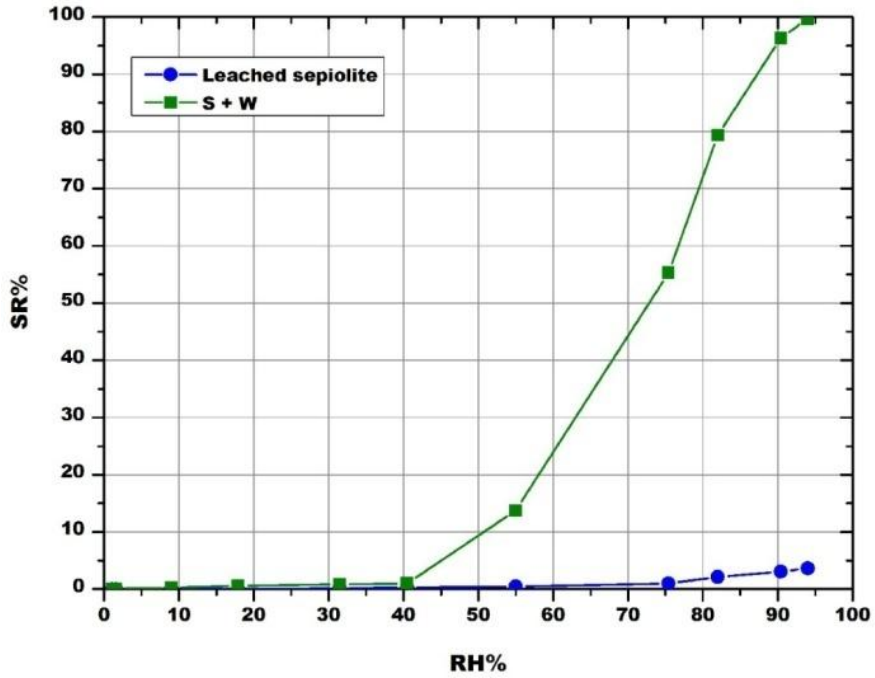

Fig. 12. Sensors response to RH after Tungsten ions precipitation onto sepiolite.

When the first physisorbed water layer is continuous, charge transport is governed by proton hopping between neighboring water molecules in the continuous film (Grotthus

chain reaction). This mechanism means that a higher resistivity of the oxides is observed at low RH values [30, 31], as experimentally verified. The sensing characteristic of an ionic-type humidity sensor is mainly determined by capillary condensation of water in all cylindrical pores, with one end closed, having radii up to the Kelvin radius given by [31]:

$$\ln\left(\frac{P_s}{P}\right) = -2\frac{\gamma M}{\rho RTr} \quad \text{(eq. 6)}$$

Where P and P_s are water vapor pressures in the surrounding environment and at saturation, respectively. M, γ and ρ are the molecular weight, surface tension and density of water, respectively. Because the precipitated oxides/hydroxides particles overlap sepiolite grains, pores of minor dimensions may be hypothesized in the doped samples, with respect to pure sepiolite. Then, these pores may be first filled with condensed water, leading to impedance variations for lower relative humidity values, from 40 to 57 RH%, whatever the precipitated ion considered.

The hydration process of clays has been investigated too [32] and the mechanism of water retention is similar to the one above described for metal oxide semiconductors: the adsorption of water on hydrophilic sites happens at low relative water vapor pressure then, followed by a multilayer adsorption on free surfaces (on porous or non-porous surfaces) and finally, capillary condensation occurs at high relative pressures in pores. It was found that the hydrophilic behavior of sepiolite is due to the four water molecules coordinated to magnesium ions and that their elimination, in our case by acid leaching and by thermal treatment, changes the character of sepiolite to hydrophobic [24]. Taking into consideration the response to humidity of the investigated sensors, we can suppose that tungsten-doping gives back its hydrophilic character to sepiolite.

Moreover, among the different investigated compositions, tungsten-doped sensors showed a significant response towards humidity at room temperature starting from 40% RH. This result may be imputed to the small size of the tungsten ion which possesses a high local charge density and, thus, generates a strong electrostatic field, resulting in an increase of adsorption sites for water-vapor adsorption, with respect to the other selected ions.

Finally, response times are rather long (Fig. 13and Table 6): for example, it takes 18 min to a tungsten-doped sepiolite sensor to reach 90% of its sensor response when RH changes from 0% to 90%. On the contrary, recovery times are much faster: it takes 1.5 min to reach 90% of the sensor response when RH changes from 90% to 0%. Long response times may be imputed to low-accessible porosity for water molecules, because of the precipitated oxides/hydroxides that cover sepiolite grains. Fast recovery times indicate that only physisorption is involved when water molecules bind with the sensing materials.

Response time	**Tungsten-doped sepiolite**
From 0% to 40% RH	39.5 min.
From 0% to 70% RH	30.1 min
From 0% to 90% RH	18.1 min.
Recovery time	-
From 40% to 0% RH	0.9 min.
From 73% RH a 0% RH	0.2 min.
From 90% RH a 0% RH	1.5 min.

Table 6. Response and recovery time of tungsten doped sepiolite sensor.

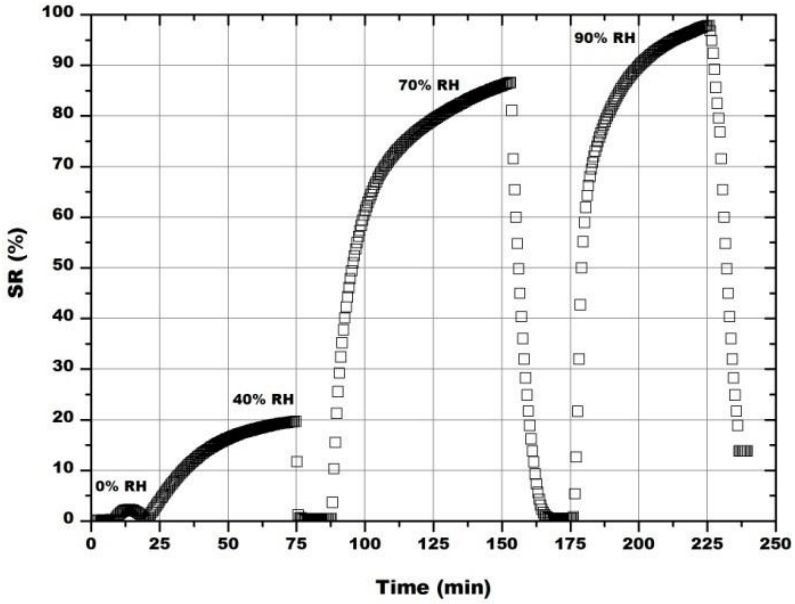

Fig.13. Response and recovery times for tungsten-doped sepiolite to RH.

3.4 Doping different ratio of Tungsten oxide onto sepiolite

Due to the interesting results obtained by doping sepiolite with 15% of tungsten oxide, samples were also prepared having different contents of tungsten oxide: 10, 20 and 25%. These samples are labeled from now on as WO10, WO20 and WO25, respectively. XRD patterns of these materials are illustrated in Fig. 14.No significant changes compared to the pattern reported in Fig.5 and related to the composition containing 15% of tungsten oxide are evidenced.

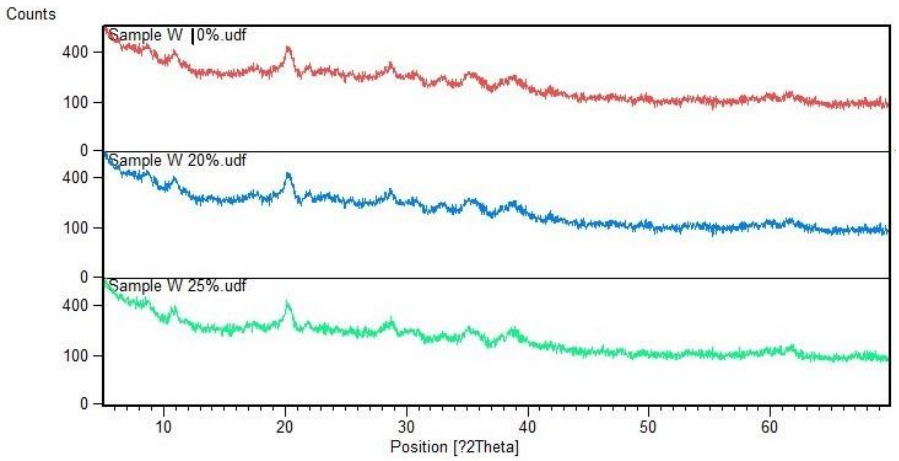

Fig. 14. XRD patterns of W10, WO10 and WO25 tungsten doped–sepiolite, heat treated at 550°C

The response towards RH of these new samples was similar and poor responses compared to the sample with 15% tungsten oxide doped sepiolite can be visible in Fig. 15, in which these samples start to detect water vapor around 30%RH.Moreover, there is no strong response, even at high RH values.

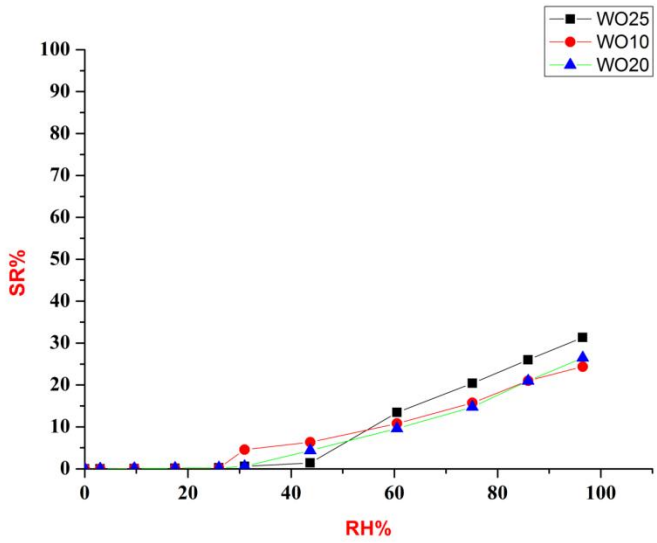

Fig. 15. Sensors response to RH of different ratio of tungsten doped–sepiolite.

2.4. Conclusion

Different oxide/hydroxide nanoparticles were obtained on sepiolite grains following a simple low cost wet chemical route. The fact that these nanoparticles appear supported on an inert matrix makes possible to avoid manipulation, agglomeration and harmful character that pure nanoparticles usually have.

Among the investigated compositions, tungsten-doped sepiolite with 15% of tungsten oxide seems to be the most interesting one, even, if its composition has to be optimized, in order to have responses to lower RH values.

References

[1] Ding, Z., Frost, R. L. 2004. Study of Copper Adsorption on Montmorillonites using Thermal Analysis Methods, J Colloid Interface Sci. 269, 296-302.

[2] Nagata, H., Shimoda, S., Sudo, T. 1974. Dehydration of bound water of sepiolite, Clays & Clay Mineral. 22, 285–293.

[3] Esteban-Cubillo, A., Tulliani, J. M., Pecharromán, C., Moya, J. S., 2007. Iron oxide nanoparticles supported on sepiolite as a novel humidity sensor. J. Eur. Ceram. Soc. 27, 1983–1989.

[4] Debliquy, M., Baroni, C., Boudiba, A., Tulliani, J.-M., Olivier, M., Zhang, C. 2011. Sensing characteristics of hematite and barium oxide doped hematite films towards ozone and nitrogen dioxide. Procedia Eng. 25, 219 – 222.

[5] Hibino, T., Tsunashima, A., Yamazaki, A., Otsuka, R. 1995. Model calculation of sepiolite surface areas. Clays Clay Miner. 43, 4, 391-396.

[6] Suárez, M., García-Romero, E. 2012. Variability of the surface properties of sepiolite, Applied Clay Sci. 67–68, 72–82.

[7] García-Romero, E., Suárez, M. 2014. Sepiolite-palygorskite polysomatic series: Oriented aggregation as a crystal growth mechanism in natural environments. Am. Mineral. 99, 8-9, 1653-1661.

[8] Esteban-Cubillo, A., Pina-Zapardiel, R., Moya, J. S., Barba, M. F., Pecharromán, C.2008. The role of magnesium on the stability of crystalline sepiolite structure. J. Eur. Ceram. Soc. 28, 1763–1768.

[9] Kleber, E. V., Love, B. 1963. The Technology of Scandium, Yttrium and the Rare Earth Metals. Pergamon, London; Macmillan, New York.

[10] Tulliani, J.-M., Bonville, P. 2005. Influence of the dopants on the electrical resistance of hematite-based humidity sensors. Ceram. Int. 31, 507–514.

[11] Simons, S. J. R., Fairbrother, R. J. 2000. Direct observations of liquid binder–particle interactions: the role of wetting behaviour in agglomerate growth, Powder Technol. 110, 44–58.

[12] Valentin, J. L., López-Manchado, M. A., Rodríguez, A., Posadas, P., Ibarra, L.2007. Novel anhydrous unfolded structure by heating of acid pre-treated sepiolite, Applied Clay Sci. 36, 245-255.

[13] Miura, A., Nakazawa, K., Takei, T., Kumada, N., Kinomura, N., Ohki, R., Koshiyama, H.2012. Acid-, base-, and heat-induced degradation behavior of Chinese sepiolite, Ceram. Int. 38, 4677–4684.

[14] Wang, F., Liang, J. S.,Tang, Q.-G., Meng, J.-P., Wu, Z.-Z., Li, G.-S. 2006. Microstructure of sepiolite and its adsorbing properties to dodecanol, Trans. Nonferrous Met. Soc. China, 16, s406-s410.

[15] Orera, A., Larraz, G., Sanjuan, M. L. 2013. Spectroscopic study of the competition between dehydration and carbonation effects in La_2O_3-based materials, J. Eur. Ceram. Soc. 33, 2103-2110.

[16] Logvinenko, V., Bakovets, V., Trushnikova, L.2014. Dehydroxylation kinetics of gadolinium hydroxide, J. Therm. Anal. Calorim. 115, 517–521.

[17] Dinescu, R., Preda, M. 1973. Thermal decomposition of strontium hydroxide, J. Thermal Anal., 465-473.

[18] Doreswamy, B. H., M. Mahendra, J. Shashidhara Prasad, P. A. Varughese, G. Varghese, 2011. Samarium Coordinated Polymer: Structural, Vibrational and Thermal Studies of $[Sm_2(C_3H_2O_4)_3(H_2O)_6]_n$, J. Inorg. Organomet. Polym. 21, 376–383.

[19] Tong, J., Eyring, L.1995. The evolution of a thin, amorphous neodymium hydroxide film to the C-type oxide-an HREM study, J. Alloys Compd. 225, 139-141.

[20] Kovanda, F., Grygar, T., Dornicák, V.2003. Thermal behaviour of Ni–Mn layered double hydroxide and characterization of formed oxides, Solid State Sci. 5, 1019–1026.

[21] Varshney, P. K., Nidhi, R. Ramachadran, Agnihotry, S. A. 1999. Colloidal tungstic oxide films for electrochromic applications: Preliminary studies, Indian J. Pure & Applied Phys. 37, 262-265.

[22] Serna, C., Ahrlichs, J. L., Serratosa, J. M. 1975. Folding in sepiolite crystals, Clay Clay Miner. 23, 452 -457.

[23] Torró-Palau, A., Fernández-García, J. C., Orgilés-Barceló, A. C. 1997. Structural modification of sepiolite (natural magnesium silicate) by thermal treatment: effect on the properties of polyurethane adhesives, Int. J. Adhes. Adhes. 17, 111 – 119.

[24] Molina-Sabio, M., Caturla, F., Rodríguez-Reinoso, F., Kharitonova, G. V.2001. Porous structure of a sepiolite as deduced from the adsorption of N_2, CO_2, NH_3 and H_2O, Micropor. &Mesopor. Mat. 47, 389-396.

[25] Kok, M. V., 2013. Thermal Characterization of Sepiolite Samples, Energy Sources A, 35, 173–183.

[26] Cudennec, Y., Lecerf, A. 2003. The transformation of $Cu(OH)_2$ into CuO, revisited. Solid State Sci. 5, 1471–1474.

[27] Ross-Medgaarden, E. I., Wachs, I. E. 2007.Structural Determination of Bulk and Surface Tungsten Oxides with UV- vis Diffuse Reflectance Spectroscopy and Raman Spectroscopy. J. Phys. Chem. C. 111, 15089-.

[28] Montanari, B.; Vaccari, A.; Gazzano, M.; Käßner, P.; Papp, H.; Pasel, J.; Dziembaj, R.; Makowski, W.; Lojewski, T. 1997. Characterization and activity of novel copper-containing catalysts for selective catalytic reduction of NO with NH_3. Appl. Catal. B 13, 205-217.

[29] Socrates, G., 2004. Infrared and Raman Characteristic Group Frequencies Tables and Charts, 3rd ed., John Wiley and Sons, Ltd, Chichester, United Kingdom.

[30] McCofferty, E., Zettlemoyer, A. C. 1971. Adsorption of water vapour on α-Fe_2O_3. Discussion Faraday Soc., 52, 239-254.

[31] Traversa, E., 1995. Ceramic sensors for humidity detection: the state-of-the-art and future developments, Sens. Actuators B, B23, 135-156.

[32] Prost, R, Koutit, A., Benchara E., Huard, E., 1998. State and location of water adsorbed on clay minerals; consequences of the hydration and swelling-shrinkage phenomena,Clays Clay Miner. 46 (2), 117-131.

Chapter Three:

Synthesis, characterization of ‘sepiolite-like’ and determination of its sensing features towards humidity

Abstract

Synthesis of clay minerals, specifically sepiolite, gives the possibilities to obtain new materials with better performances towards a specific application. However, few papers deal with the synthesis of sepiolite-like powders. Therefore, in this part of the research a new magnesium silicate nanopowder was prepared by a simple sol gel route.

The obtained powders were characterized by X-ray powder diffraction, thermogravimetric-differential thermal analysis (TG-DTA), nitrogen adsorption at -196°C (BET), infrared spectroscopy, X-ray photoelectron spectroscopy (XPS) and Field Emission Scanning Electron Microscopy. The synthesized powders, when doped with iron ions, exhibit interesting features for humidity detection.

3.1 Introduction

Clay minerals form due to the chemical weathering of other silicate materials at the surface of the earth[1].They have a layered structure and can be used in various applications depending on their high specific surface area, ion exchange capacity and hydration process [2-4].Developing of new materials which act as the naturally occurring clays attract great attention these days in order to control the intrinsic properties of them and to create new functional materials [5].The purpose of controlling the composition of the new materials is to overcome the existence of impurities in the original clays hence, the synthetic or the modified materials can be used in many applications such as adsorption, catalysis and sensing features [6-8].The nomenclature committees of the Association Internationale pour l'étude des Argiles (AIPEA) permits the use of the term 'synthetic sepiolite' or 'sepiolite -like' for these new materials [9].As illustrated in the first chapter, sepiolite is a hydrous magnesium silicate having the chemical formula $Mg_8Si_{12}O_{30}(OH)_4(H_2O)_4.8H_2O$), its structural units are composed of two tetrahedral silica sheets and a discontinuous central layer of octahedral magnesium oxide which, gives rise to the formation of open tunnels with dimensions of 0.36 × 1.06 nm along the fibrous structure. It has a large external specific surface area (SSA) out of the channels (ca. 320 m^2g^{-1}) as that of zeolite and silica gels and a low cation exchange capacity (CEC)[10].

The first attempt to synthesize sepiolite was by hydrothermal synthesis at 150-200°C in the presence of sepiolite seeds [14]. In this part of my research activity, I tried to synthesize an amorphous magnesium silicate by a sol–gel technique [15].

3.2. Experimental

3.2.1 Materials and methods

All reagents were ACS grade. The preparation of synthetic sepiolite was as follows: 32.4 mL of tetraethyl orthosilicate ($Si(OC_2H_5)_4$,TEOS) was first mixed with ethanol for 1 h at 75°C and pH was adjusted to 5 by HNO_3 addition. In the meantime, a solution of $Mg(NO_3)_2.6H_2O$was prepared in distilled water and then, added dropwise to the former solution and refluxed for 1-1.5 h until the formation of gel(labeled from now on as S1).The obtained gel was dried in an oven at 120°C overnight, prior to calcination at 500°C for 5 h to eliminate all by-products.

Then, a second sample (labeled as S5) was synthesized, and respect to the stoichiometric composition of sepiolite, 10% Mg^{2+}ions were replaced by Fe^{3+} ones by using 0.01 mole of $Fe(NO_3)_3.9H_2O$. In this case, the gelation time became 7 h. In this process, the formed gel was washed for several times (20 wt% of solid) in 1:1, 1.5:1 and 3:1 ethanol: distilled water solutions respectively, while pure ethanol was used for the last washing. It is worth mentioning that the formed gel was centrifuged at 3800 rpm for 20 min to separate the solid content from the liquid before re-dispersing it into the new solution after each washing. After re-dispersion into the new washing solution, sonication of the gel was performed by means of an ultrasonic bath for 15 min and the solution was kept under magnetic stirring for 1 h. After preliminary tests (samples S2-S4), more attention was paid to avoid the loss of a certain amount of iron ions after the first washing step, (the centrifuged solution was red brownish colored): a solution of ammonia was used to precipitate iron(and probably also magnesium) hydroxides at pH 10. Finally, 2 g of the

washed sample (Fig. 1) was added to 19.5 mL solution of 0.3M NH_4OH and put in an oven at 80°C in a sealed container for about 48 h in order to peptize the washed gel [16], to obtain very small particles in solution for (i.e. after transformation into a sol) (Fig. 2). After that, the prepared sol is dried in an oven, and then heat treated at 500°C for 2 h. Finally, a third series of samples was also prepared (sample S6), where the stoichiometric synthetic sepiolite (S1) is doped with 10% Fe^{3+} ions. The preparation process is the same as with the sample S5.

Fig.1. Gel S5 after final washing

3.2.2 Sensors preparation.

A screen-printing ink was obtained by dissolving completely 0.4 g of $Fe(NO_3)_3.9H_2O$ in 0.625 mL EtOH, under magnetic stirring, followed by the addition of 0.066 mL monoethanol amine + 0.625 mL terpenol (Emflow, Emca Remex, USA) under continuous stirring. Then, the powder S1 (0.68 g) was added progressively to this solution. The obtained ink was screen-printed onto an alumina substrate with interdigitated Pt electrodes and dried overnight at room temperature (Fig. 2).Finally, the films were fired at 550°C for 1 h. It is worth mentioning that the obtained sensing film exhibited poor adhesion onto the alumina substrate as there was a high shrinkage of the film which can be clearly observed in FESEM in the result section.

Concerning the S5and S6 powders, after drying, they were mixed directly with the Emflow to prepare the ink. Then, these inks were screen-printed onto interdigitated Pt electrodes and the same condition of drying and firing as above-mentioned for S1were used. These films also were fired at 550°C for 1 h. These samples (S5 and S6) showed a better adhesion onto the substrates than S1.

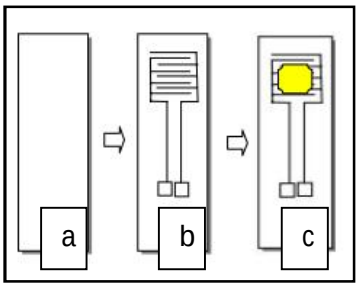

Fig.2.Diagram of the preparation of the sensing film a) Al_2O_3 substrate, b) Pt electrode screen-printed onto the Al_2O_3 substrate and c) sensing film over Pt electrodes.

3.2.3 Testing of the sensors

Sensors were tested in a laboratory apparatus made of a thermostated chamber, operated at 25°C, in which relative humidity (RH) could be varied between 0 and 96%by steps, each one of 3 min [17].The laboratory apparatus was calibrated to ensure a constant air flow during electrical measurements (0.05L/s). The sensors resistance was determined by means of a LCR meter (Hioki 3533-01, Japan). During the measurements, the sensors were alimented by an AC tension of 1 V at 1 kHz.

The sensor response (SR), expressed in %, was defined as the relative variation of the starting resistance, compared with the resistance measured under gas exposure (eq. 1):

$$SR(\%) = 100\frac{|R_0 - Rg|}{R_0} \quad \text{(eq. 1)}$$

Where R_0 and R_g are the starting (in the absence of the test gas) and the gas exposed measured resistances of the sensors, respectively.

3.2.4 Material Characterizations

Particle size distribution was determined after powders calcination by means of a laser granulometer(Malvern 3600D) and after dispersion in ethanol and sonication for 10 min. X-ray diffraction patterns were collected on powders by means of a X'PertHighScore Philips Analytical Diffractometer, equipped with a Cu anticathode (λ Cu Kα anticathode= 0.154056 nm). Samples were scanned at a rate of 0.02°/ s in the range from 5° to 70° in 2θ.

Samples were uniaxially pressed in the form of thin, self-supporting wafers (optical density of about 20 $mg.cm^{-2}$) and studied in a standard vacuum frame (residual pressure

below 10^{-3} mbar) in a home-made IR cell, equipped with KBr windows. Spectra were recorded at 2 cm^{-1}resolution on a Bruker Equinox 55 spectrophotometer equipped with a mercury cadmium telluride cryodetector.

About 50 mg of the prepared powder was placed into a platinum crucible for simultaneous thermogravimetric–differential thermal analysis (Neztsch STA 409, Germany) and then, heated at 10°C/min up to 800°C, under static air.
X-ray photoelectron spectroscopy (XPS) was carried out on K-Alpha1063 spectrometer.
Finally, samples were gold or chromium sputtered for Scanning Electron Microscopy (SEM) observations.

3.3. Results and discussion

3.3.1 Particle size distribution

Results showed that the thermal treated powders at 500°C S5 and S6 have a lower particle size distribution (PSD) with respect to S1 (Table 1). These results may be related to the peptization process which led to less agglomerated powders in samplesS5 and S6.

Cumulative wt%	**S1**	**S5**	**S6**
10%	8.5	5.1	3.9
50%	88.5	26.4	18.5
90%	140	111.4	98.5

Table 1. PSD of S1, S5 and S6 powders fired at 500°C

3.3.2 XRD

XRD patterns of S1, S5 and S6show that thefired powders are amorphous (Fig. 3, 4 and 5). It seems that ammonium nitrate was not formed during precipitation at pH=10 of iron and magnesium species in samples S5 and S6.

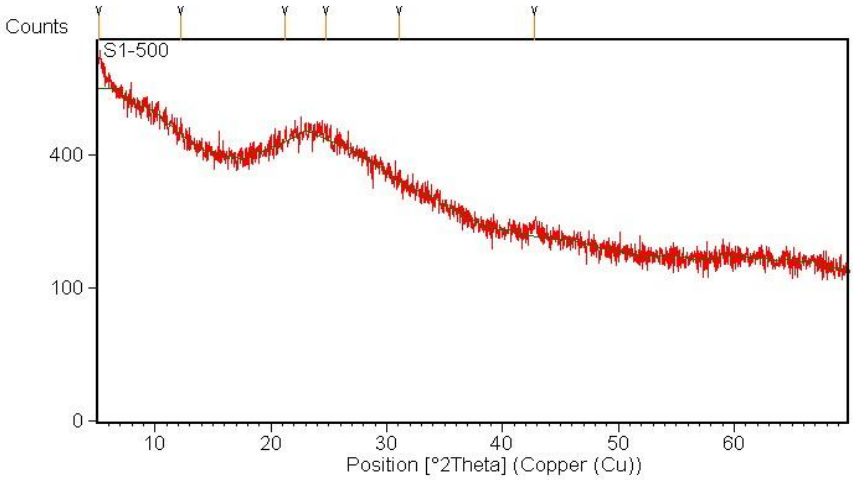

Fig.3. XRD pattern of S1 powder fired at 500°C for 5 h

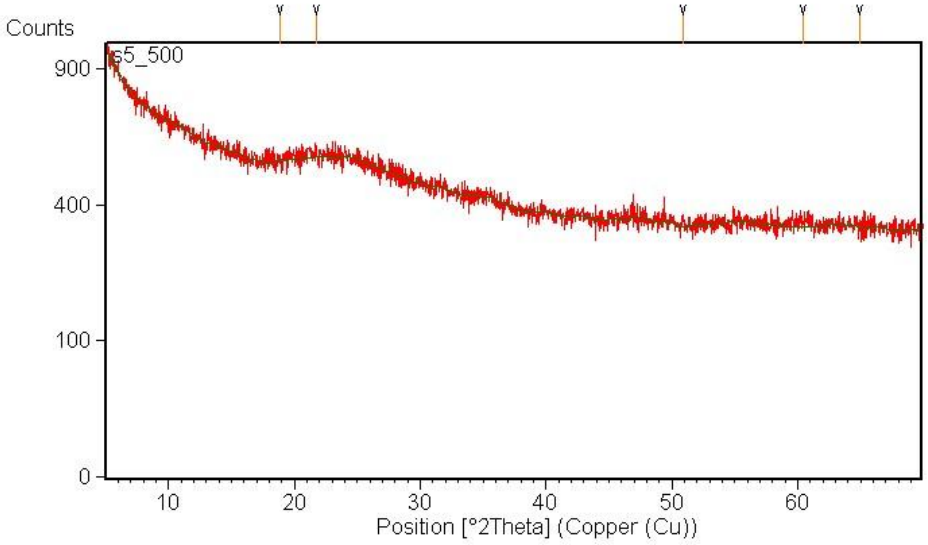

Fig.4.XRD pattern of S5 powder fired at 500°C for 2 h

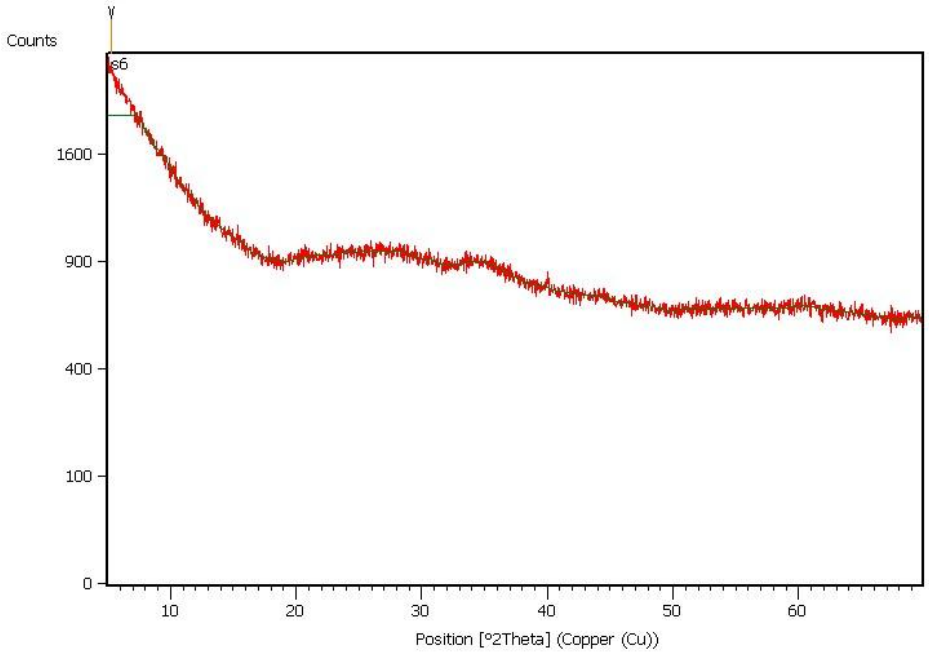

Fig.5. XRD pattern of S6 powder fired at 500°C for 2 h

3.3.3 FTIR

Fig.6. shows the IR spectra of S1 and S5 where the peaks in the higher wave number region at 3600–3300 cm^{-1} are ascribed to O–H stretching vibration. In addition, the band at 3686 cm^{-1} corresponds to the triple bridge group Mg-OH; another broad band at 3432 cm^{-1} is due to stretching vibrations of hydroxyl groups from iron oxide and water [18]. The band at 1653 cm^{-1} is attributed to hydrogen bond of water molecules in the structure [18].Bands in the range of 1200–400 cm^{-1} are characteristic of silicate: the sharp absorption peaks at 1035 cm^{-1} corresponds to the stretching vibration of Si–O bond. The peaks at 472 cm^{-1} may be attributed to the antisymmetric stretching modes of Si–O–Si bonds [19]. Finally, the band at 588 cm^{-1} is characteristic of Fe–O bonds, which demonstrates the presence of iron species [20].These results clearly show that the

samples exhibit characteristic vibrations for magnesium silicates, whatever the presence of iron atoms or not [15].

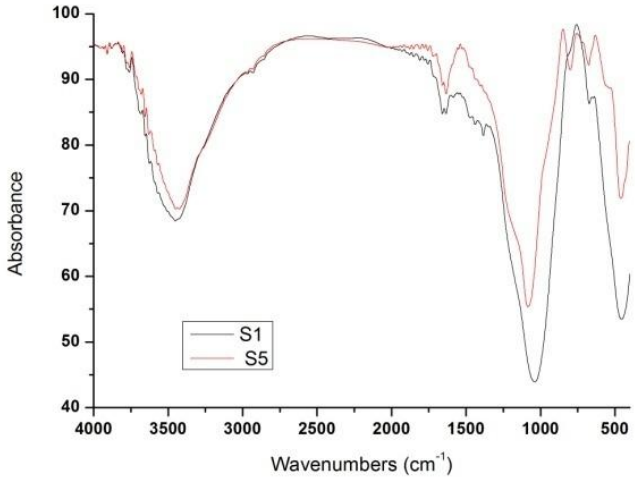

Fig.6. FTIR spectra of S1 and S5 powder fired at 500°C

3.3.4 TG-DTA

At 500°C, mass loss of sample S5 was about 23% while mass loss of sample S1 was 60.6%, these differences can be explained on the basis of the washing steps S5 underwent, which led to less by-products in the dried powder. In the case of pure sepiolite, adsorbed and zeolitic water are removed up to 200°C, while the loss of the coordination water leading to the formation of the anhydride sepioliteoccurs in the region 350-650°C [21]. However, these last peaks are absent in sample S5 (Fig.7b).

It is reported in the literature that between 200 and 400°C the presence of an exothermic peak is a sign for the development of α-Fe_2O_3 [22] and the structural rearrangement is

indicated by an exothermic for well-ordered hematite [23]. This peak was not evidenced in Fig.8b, as also expected from XRD pattern reported in Fig.3, 4and 5.

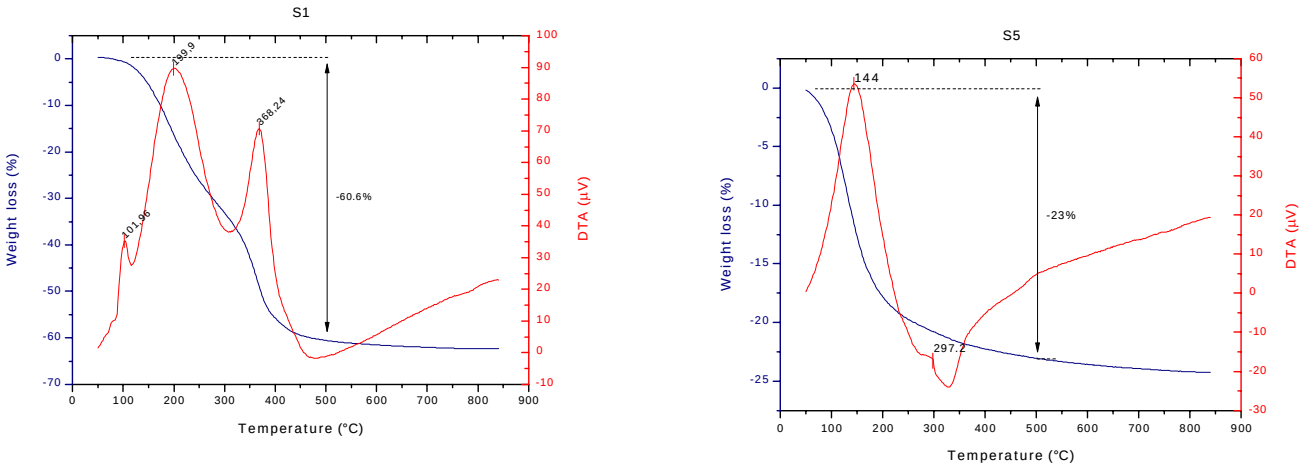

a) b)

Fig.7.TG-DTA of: a)S1and b)S5 powder

3.3.5 BET surface area and porosity

Specific Surface Area (SSA) of sample S1 is much higher that of sample S5,as shown in Table 2.Theformed iron species could contribute to the decrease in SSA or the expected substitution of magnesium ions by iron ones was not effective and the synthetic sepiolite formed partly.

Sample	S.S.A. (m^2/g)	Porosity (cm^3/g)	Pore size (nm)
S1	151.3	0.31	8.1
S5	81.3	0.20	9.4

Table2. Specific surface area of S1 and S5 powders fired at 500°C

3. 3.6 FESEM observations

FESEM micrographs show strong agglomeration of S1 fired powder and confirm laser granulometry measurements (Fig.8).

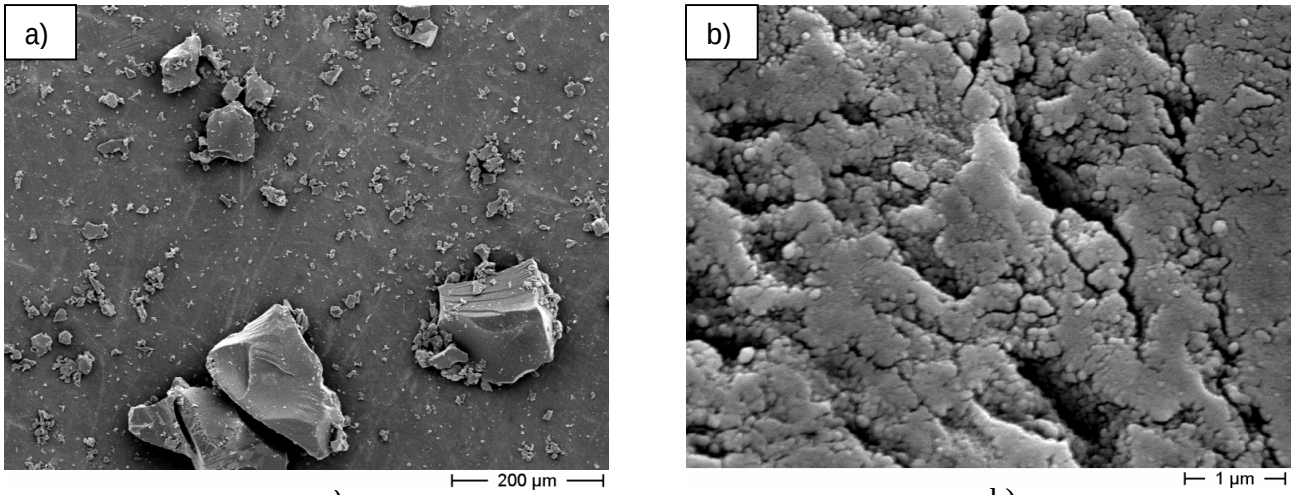

a) b)

Fig.8. FESEM micrographs of S1 powder fired at 500°C 5h:a) x150and b) x20,000

Sol gel used for adhesion of the powder S1onto the alumina substrates is clearly visible at higher magnification observations (Fig.9 c, d and e).While Fig. 10 reports the FESEM observations of the S5 peptized and oven dried powder: fine grains are obtained, confirming the effective sol formation during peptization.

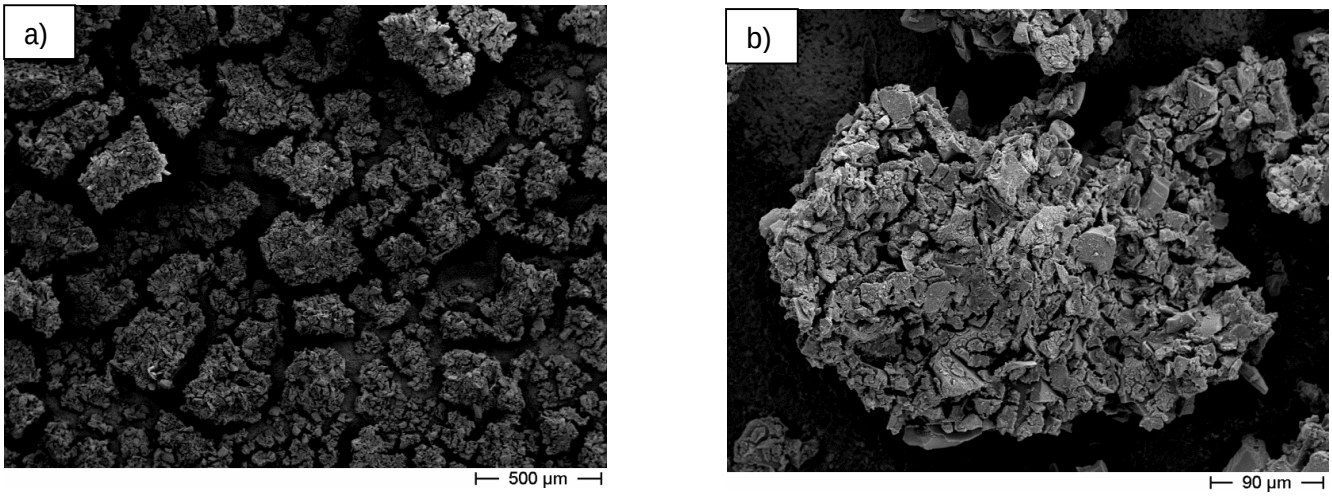

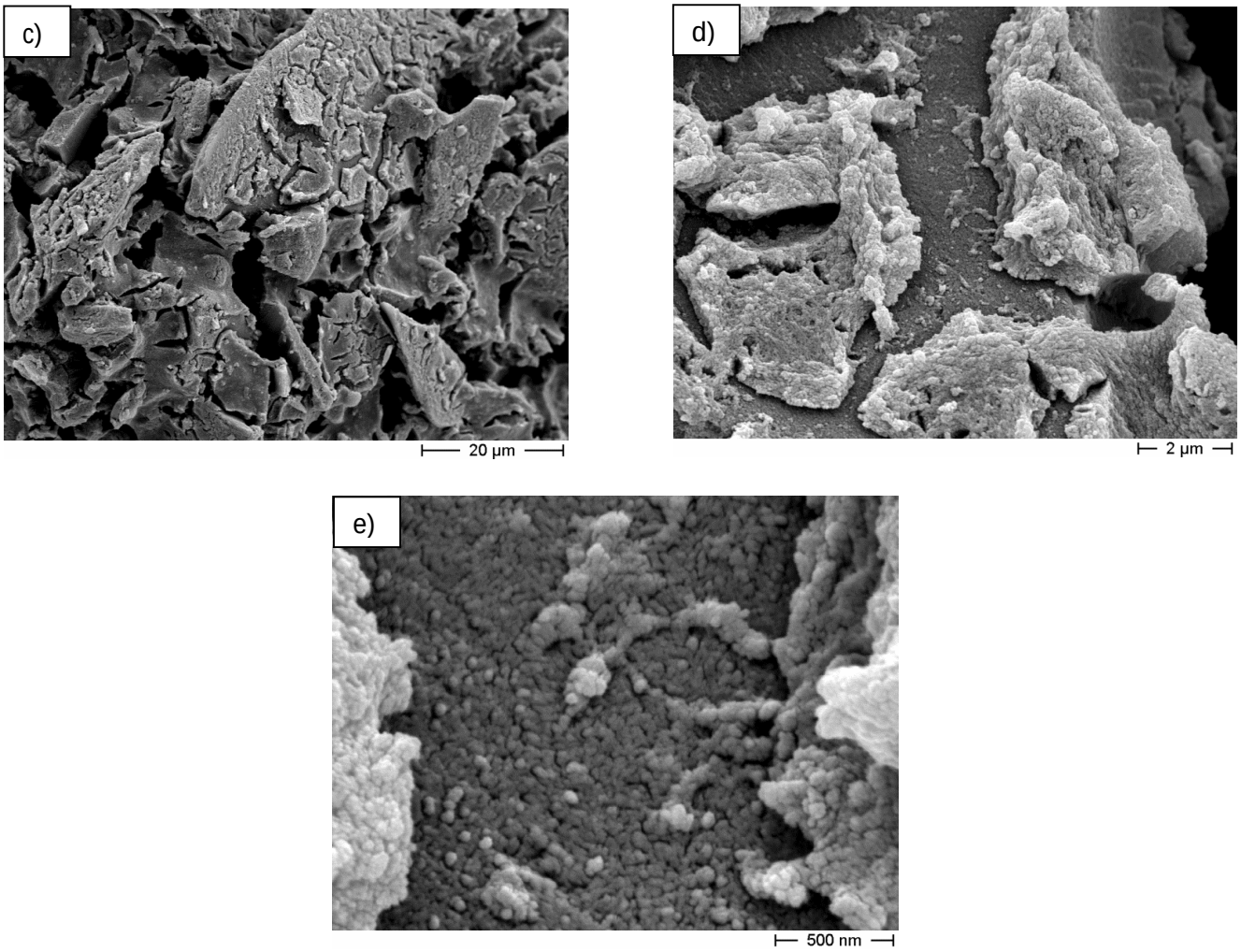

Fig.9. Screen printed S1 fired sensor at 550°C for 1 h:a) x50, b) x250, c) x1,500, d) x10,000 and e) x50,000

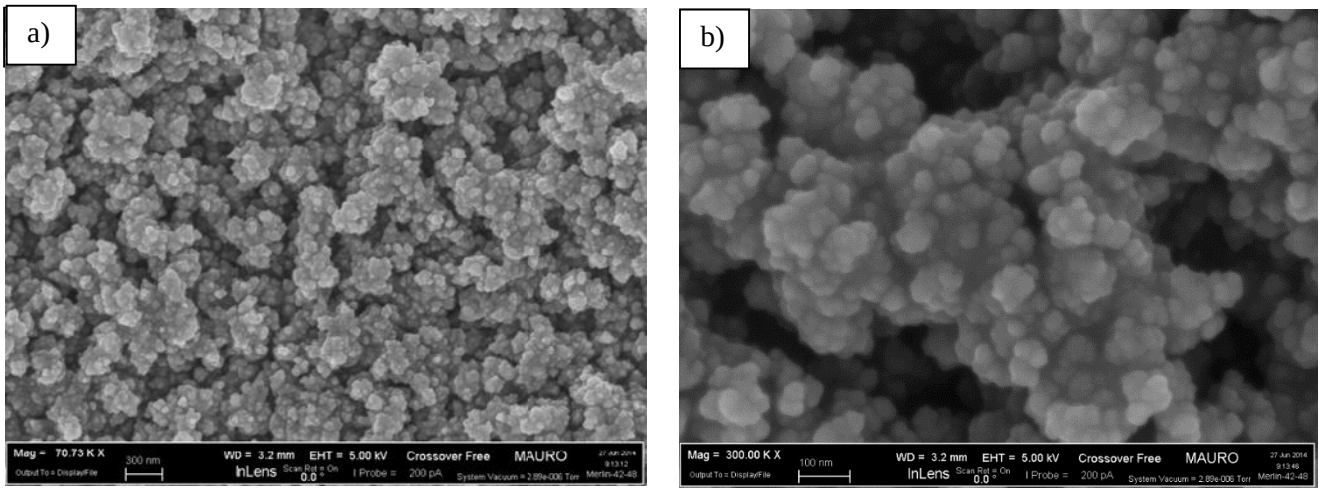

Fig.10. FESEM micrographs of oven dried S5 sol: a) x70,730 and b) x300,000

Figs.11&12 illustrate FESEM micrographs of S5 and S6 porous films.

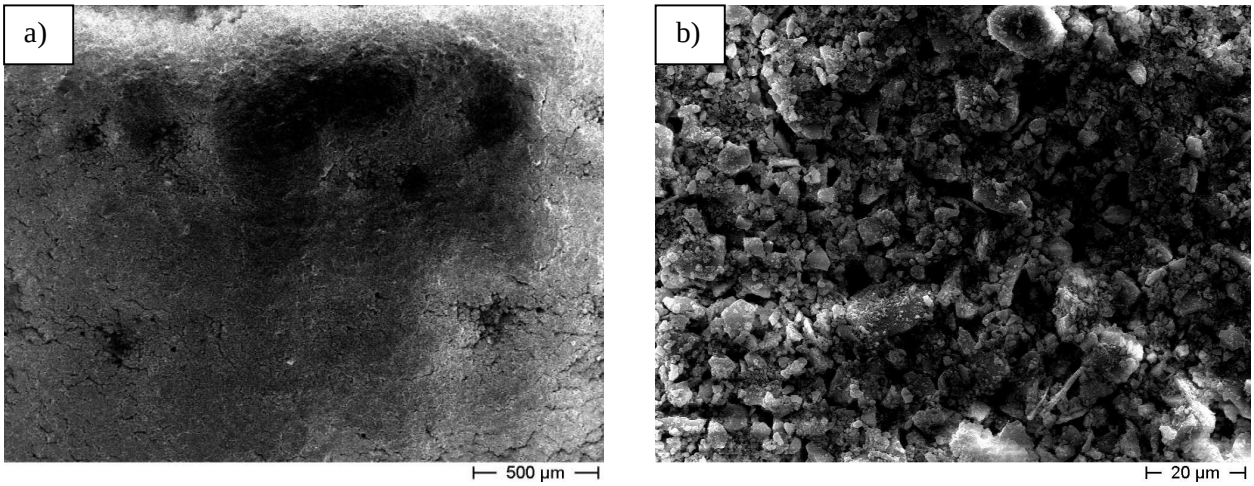

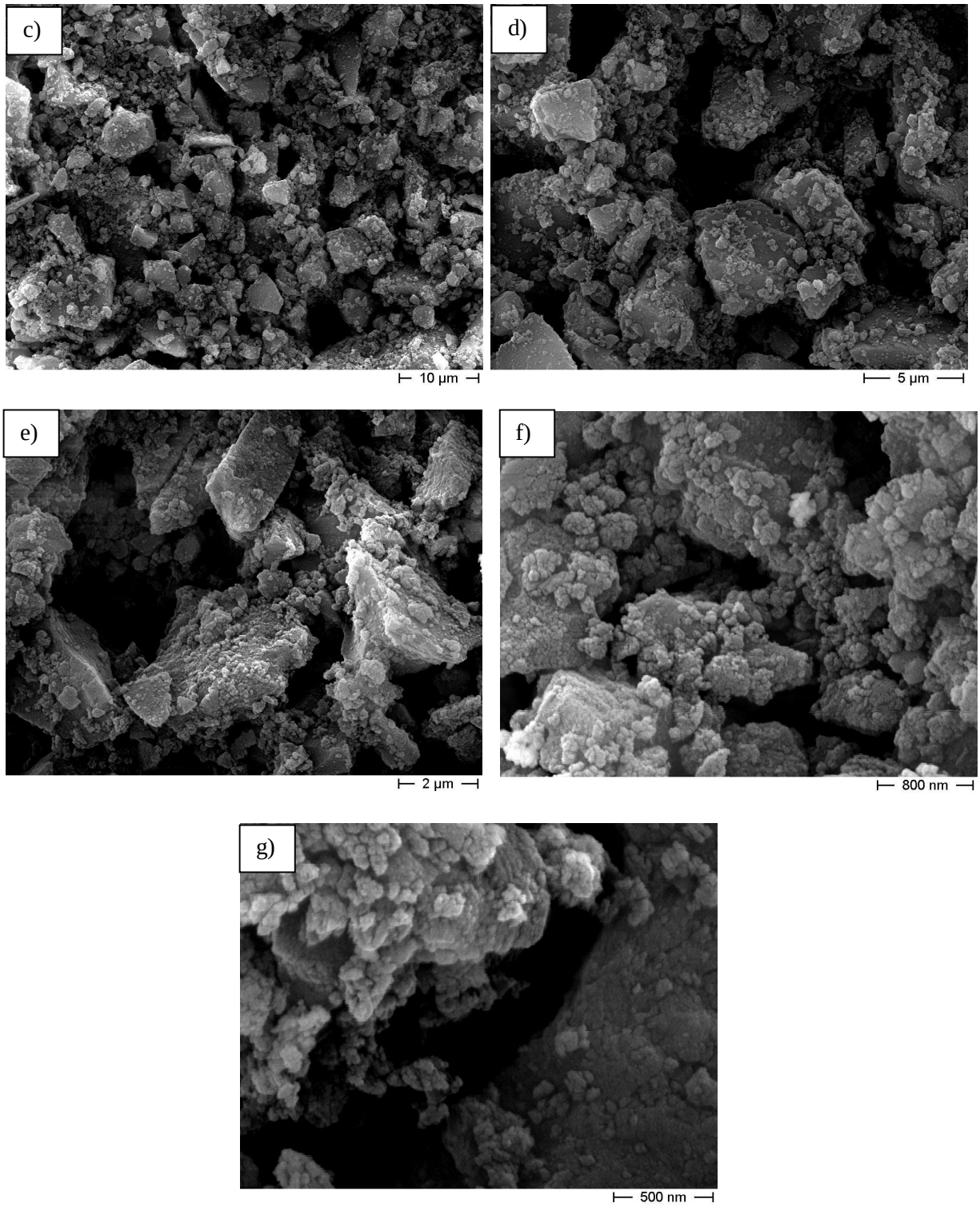

Fig.11. FESEM micrographs of S5 screen-printed films: a) x50, b) x1,000, c) x2,000, d) x5,000, e) x10,000, f) x30,000 and g) x50,000

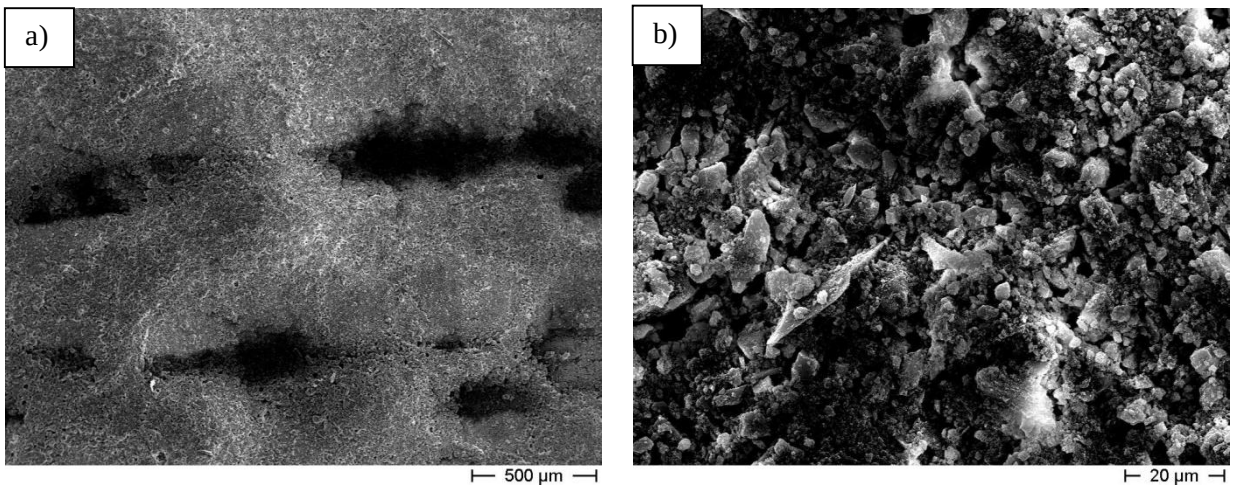
a)
500 µm
b)
20 µm
c)
10 µm
d)
5 µm

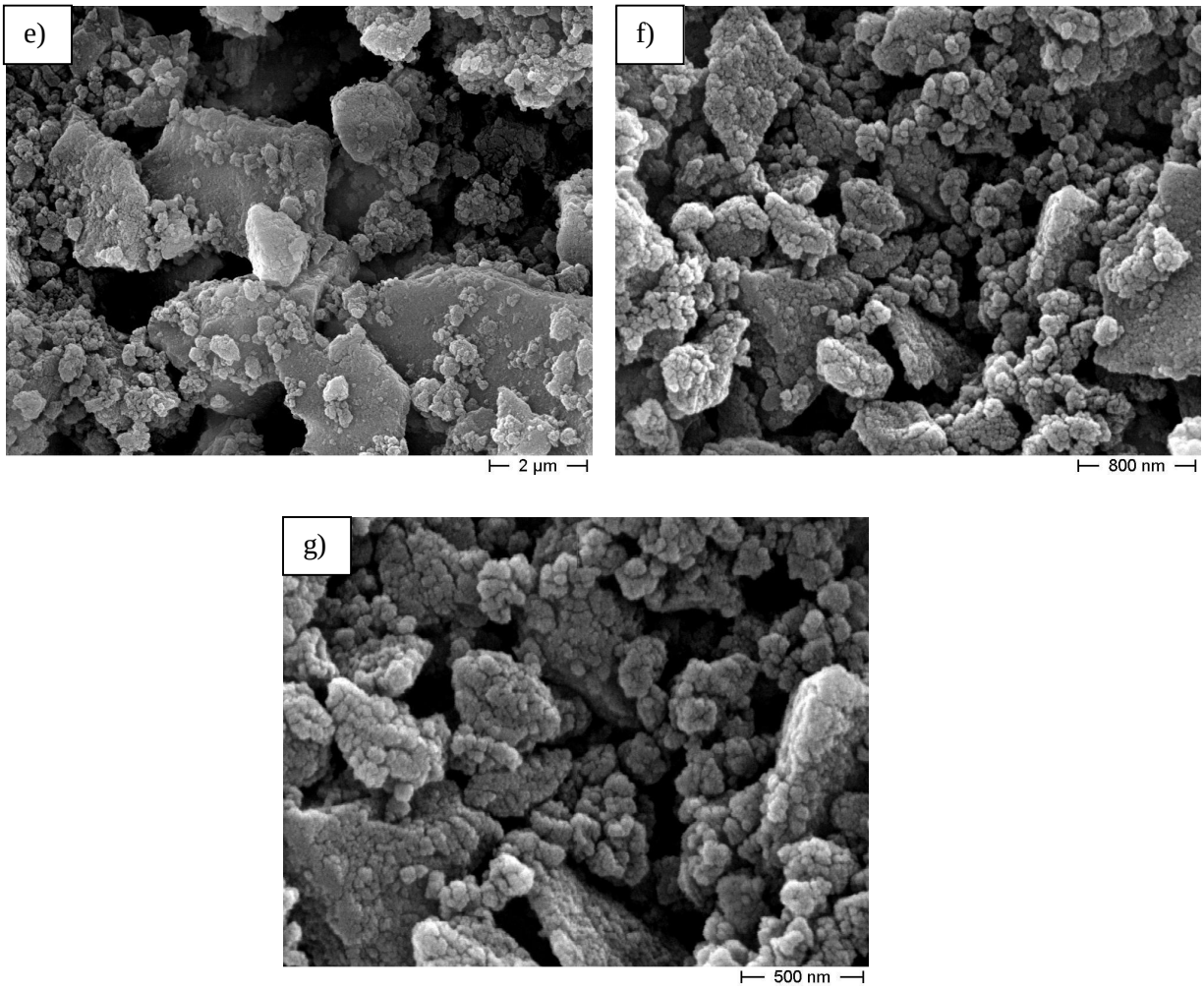

Fig.12. FESEM micrographs of S6 screen-printed films: a) x50, b) x1,000, c) x2,000, d) x5,000, e) x10,000, f) x30,000 and g) x50,000

XPS is an effective measurement method to study the surface composition and chemical states of samples without destruction. Thus, powders S1, S5 and S6 were studied by this technique and compared to pure sepiolite (Tolsa Pangel S9) (Fig. 13).

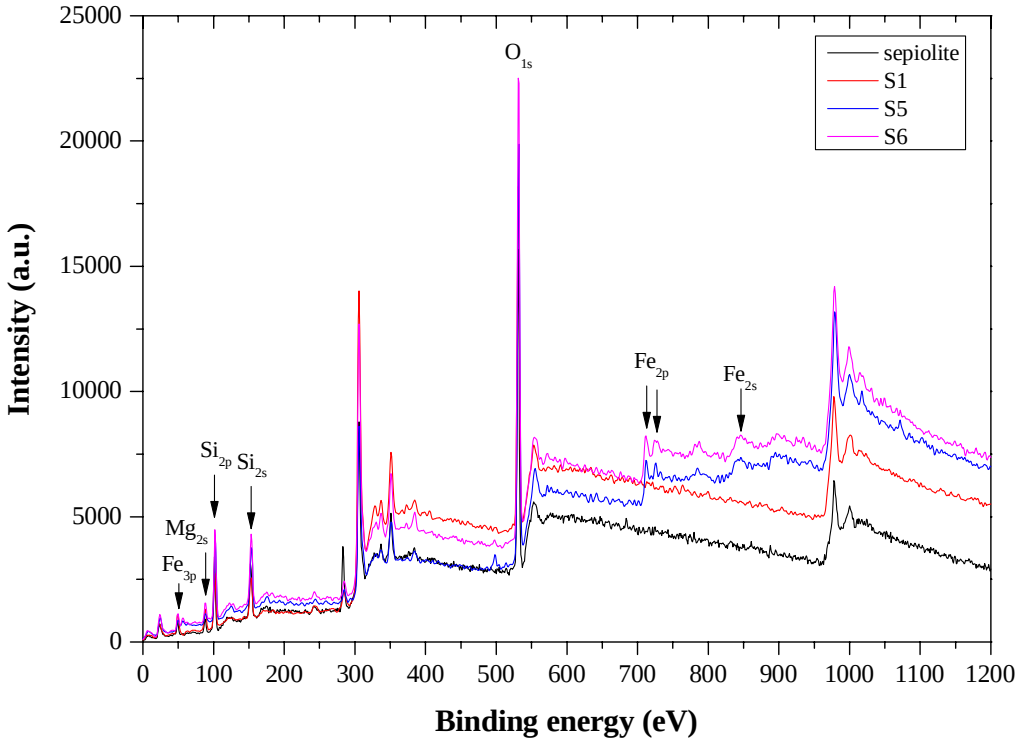

Fig.13.XPS survey spectra of pure natural sepiolite (Tolsa Pangel S9), S1, S5 and S6 powders

As can be seen in fig. 13 is the XPS survey spectra of the powders, in which the photoelectron lines at binding energy of 50.1, 88.3, 102, 152.7, 531.7, 711.6and 846.9 eV are attributed to Fe_{3p}, Mg_{2s}, Si_{2p}, Si_{2s}, O_{1s},Fe_{2p} and Fe_{2s}, respectively [24]. The nature of broad Fe 2p peak is very complicated: the photoelectron peaks approximately at 711–724 eV correspond to the binding energies of $2p_{3/2}$and $2p_{1/2}$ of Fe^{2+} and Fe^{3+} as shown in fig 14 [24].

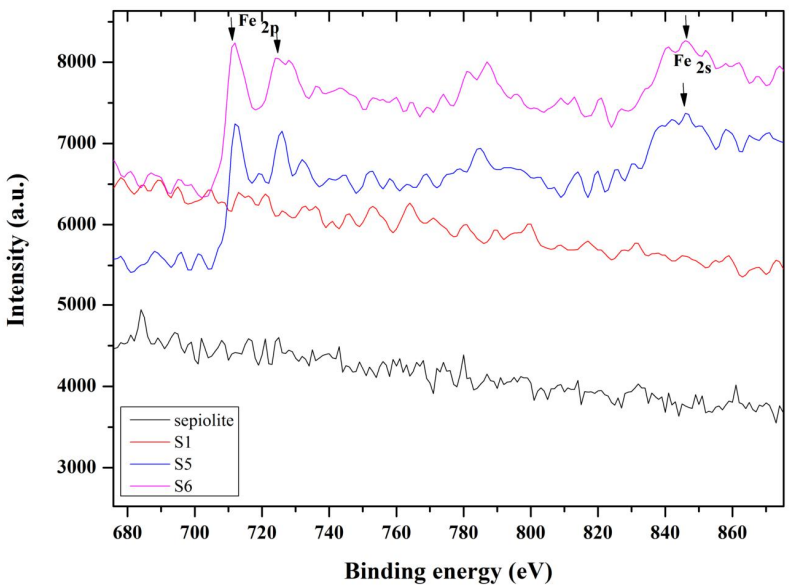

Fig 14 High-resolution XPS spectra of Fe $_{2p}$ and Fe region taken on the samples

Additionally, the high resolution spectra of O_{1S} could be deconvoluted as three peaks at 531.5, 532.4 and 533.4 eV, corresponding to hydroxyl groups (O_{OH}), lattice oxygen (O_L) and H_2O (O_{H2O}), respectively [25].

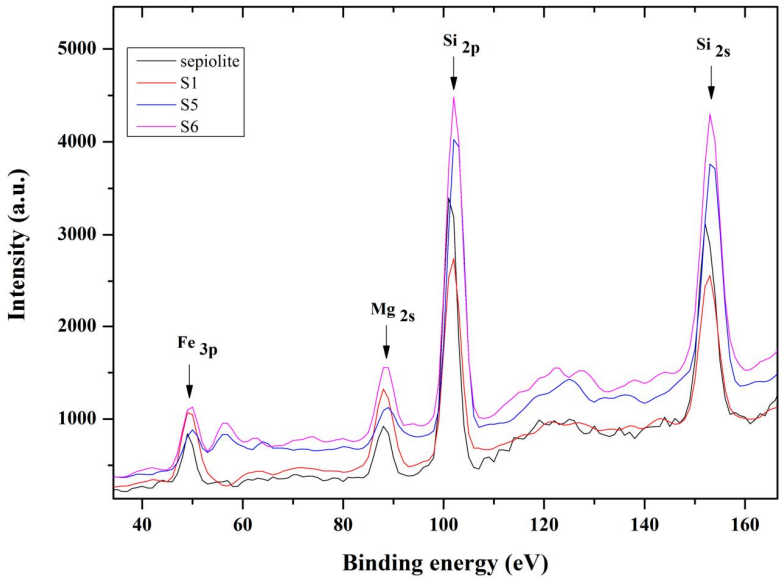

Fig 15 High-resolution XPS spectra of Fe $_{3p}$, Mg $_{2s}$, Si $_{2p}$, and Si $_{2s}$ region taken on the samples

It is well known that the value of the binding energy for a given core level measured by XPS depends on its chemical environment. A change in this chemical environment produces a shift of the core-level binding energy due to a spatial rearrangement of the valence charges and to a different potential created by the nuclear and electronic charges on all the others atoms in the compound. These shifts in the chemical energy are used as a fingerprint of the atom binding state and are very useful for identifying different compounds using XPS measurements. The peaks for Fe 3*p* and Fe 2*p*3/2 show an energy shift to higher binding energy of 1.1 and 0.5 eV. These shifts clearly indicate that iron silicides phases were formed as in fig 15[26- 28].

3.3.8 Sensitivity towards relative humidity

The sensors response to humidity is reported in Fig. 14. All the investigated compositions were highly sensitive to humidity from 40 RH%. The samples S5 and S6, showed a slight response to water vapor from about 18 RH%, probably due to the presence of hematite.

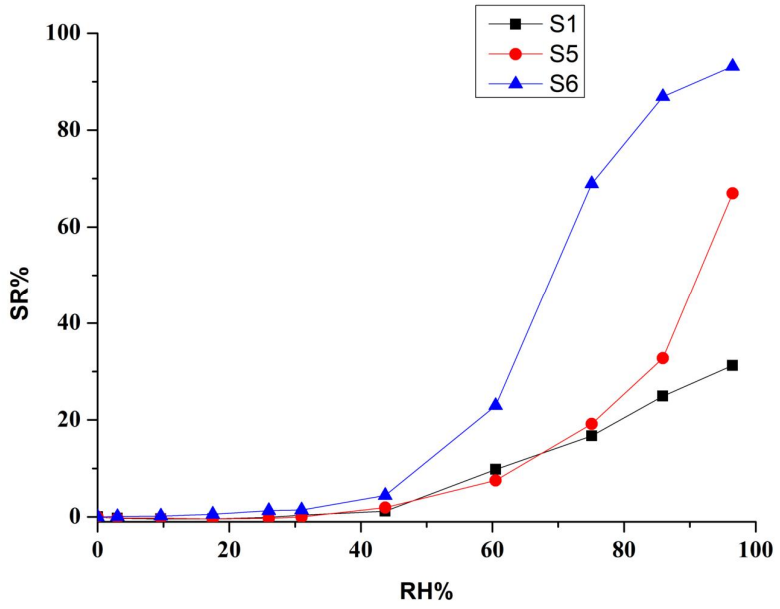

Fig.14. Sensors response to humidity at room temperature.

Response and recovery times (Table 3) are shorter for S6 respect to S5, indicating that hematite is probably more accessible to water molecules. Fast recovery times indicate that mostly thephysisorption is involved when water molecules bind with the sensing materials.

Response time (min)	**S5**	**S6**
From 0% to 60% RH	5.1	2.8
From 0% to 90% RH	5.3	4.9
Recovery time(min)	-	
From 60% to 0% RH	1.6	0.8
From 90% RH a 0% RH	1.5	2

Table 3. Response and recovery time of S5 and S6 sensors

3.4 Conclusion

An iron-doped magnesium silicate nanopowder was successfully synthesized by a sol gel processwith a simple and low cost method. Once screen-printed, thehumidity sensor was able to detect water vapor from 18 RH% with reasonableresponse and recovery times, even, if its composition has to be optimized, in order to respondto lower RH values. Cross-sensitivity measurements with interfering gases like carbon dioxidehave to be investigated.

References

[1] Martin, R. T., Bailey, S. W., Eberl, D. D., Fanning, D. S., Guggenheim, S., Kodama, H., Pevear, D. R., Srodon, J., Wicks, F. J., 1991. Report of the clay minerals society nomenclature committee: revised classification of clay materials. Clays Clay Miner. 39 (3), 333–335.

[2] Konta, J., 1995. Clay and man: clay raw materials in the service of man. Appl. Clay Sci. 10 (4), 275–335.

[3] Murray, H. H., 2000. Traditional and new applications for kaolin, smectite, and palygorskite: a general overview. Appl. Clay Sci. 17 (5–6), 207–221.

[4] Choy, J.-H., Choi, S.-J., Oh, J.-M., Park, T., 2007. Clay minerals and layered double hydroxides for novel biological applications. Appl. Clay Sci. 36 (1–3), 122–132.

[5] Zhou, C. H., Li, X. N., Ge, Z. H., Li, Q. W., Tong, D. S., 2004. Synthesis and acid catalysis of nanoporous silica/alumina–clay composites. Catal. Today 93 (5), 607–613.

[6] Adoor, S. G., Sairam, M., Manjeshwar, L. S., Raju, K. V.S. N., Aminabhavi, T. M., 2006. Sodium montmorillonite clay loaded novel mixed matrix membranes of poly(vinyl alcohol) for pervaporation dehydration of aqueous mixtures of isopropanol and 1, 4-dioxane. J. Membr. Sci. 285 (1–2), 182–195.

[7] Bergaya, F., Lagaly, G., 2006. General Introduction: Clays, Clay Minerals, and Clay Science. In: Bergaya, F., Theng, B. K. G., Lagaly, G. (Eds.), Handbook of Clay Science: Developments in Clay Science, vol. 1. Amsterdam, Elsevier, 1–18.

[8] Ahmed S. Afify, M. Hassan, M. Piumetti, I. Peter, B. Bonelli, J. -M. Tulliani, 2015 "Elaboration and characterization of modified sepiolites and their humidity sensing features for environmental monitoring", Applied Clay Science, Vol. 115: 165–173.

[9] Guggenheim, S., Adams, J.M., Bain, D. C., Bergaya, F., Brigatti, M. F., Drits, V.A., Formoso, M. L. L., Galan, E., Kogure, T., Stanjek, H., 2006. Summary of recommendations of nomenclature committees relevant to clay mineralogy: report of the Association Internationale pour l'Etude des Argiles (AIPEA) Nomenclature Committee for 2006. Clay Miner. 41, 863–877.

[10] Hibino, T., Tsunashima, A., Yamazaki, A., Otsuka, R. 1995. Model calculation of sepiolite surface areas. Clays Clay Miner. 43, 4, 391-396.

[11] Nitta, T.; Hayakawa, S. Ceramic Humidity Sensors. IEEE Trans. Components Hybrids Manuf. Technol. 1980, 3, 237–243.

[12] Yamazoe, N.; Shimizu, Y. Humidity Sensors: Principles and Applications. Sens. Actuators 1986, 10, 379–398.

[13] Traversa, 1995, E. Ceramic Sensors for Humidity Detection: The State-of-the-Art and Future Developments. Sens. Actuators B Chem., 23, 135–156.

[14] Mizutani, T., Fukushima, Y., Okada, A., Kamigaito, O., 1991. Hydrothermal synthesis of sepiolite. Clay Miner. 26 (3), 441–445.

[15] K. Narasimharao, M. Mokhtar, S. N. Basahel, S. A. Al-Thabaiti, Synthesis, characterization, and catalytic activity of nitridated magnesium silicate catalysts, J Mater Sci (2013) 48:4274–4283

[16] Laura Montanaro, 1990, Élaboration des poudres céramiques par voie sol-gel : zircone et à la zircone yttriée-Application au dispersoïde alumine, Ph.D. thesis, Ecole Nationale Supérieure des Mines de Saint-Etienne

[17] Tulliani, J.-M., Bonville, P. 2005. Influence of the dopants on the electrical resistance of hematite-based humidity sensors. Ceram. Int. 31, 507–514.

[18] R. L. Frost, G. A. Cash, J. T. Kloprogge, 1998, Vibrat. Spectrosc. 16, 173.

[19] E. Doelsch, W. E. E. Stone, S. Petit, A. Masion, J. Rose, J. Y. Bottero, D. Nahon, Speciation and Crystal Chemistry of Fe(III) Chloride Hydrolyzed in the Presence of SiO_4 Ligands: 2. Characterization of Si - Fe Aggregates by FTIR and ^{29}Si Solid-State NMR.

[20] Serna, C., Ahrlichs, J.L., Serratosa, J.M. 1975. Folding in sepiolite crystals, Clay Clay Miner. 23, 452-457.

[21] Valentin, J.L., López-Manchado, M.A., Rodríguez, A., Posadas, P., Ibarra, L.2007. Novel anhydrous unfolded structure by heating of acid pre-treated sepiolite, Applied Clay Sci. 36, 245-255.

[22] Mária Földvári, 2011. Handbook of thermogravimetric system of minerals and its use in geological practice, Geological Institute of Hungary,57-59.

[23] Cornell RM, Schwertmann U. 1996. The iron oxides. Weinheim:VCH Verlag, 570.

[24] T. Yamashita, P. Hayes, 2008, Analysis of XPS spectra of Fe^{+2} and Fe^{+3} ions in oxide materials, Appl. Surf. Sci. 254, 2441–2449.

[25] C. Liu, Y. Li, P. Xu, M. Li, P. Huo, 2014, Supercritical-assistant liquid crystal template approach to synthesize mesoporous titania/multiwalled carbon nanotube composites with high visible-light driven photocatalytic performance, Mater. Res. Bull., 174–182.

[26] S. Y. Ji, G. M. Lalev, J. F. Wang, M. Uchikoshi, and M. Isshiki, 2005, Mater. Lett. 59, 2370.

[27] Z. Yang, K. P. Homewood, M. S. Finney, M. A. Harvey, and K. J. Reeson, 1995, J. Appl. Phys. 78, 1958.

[28] D. R. Miquita, J. C. González,a_ M. I. N. da Silva, W. N. Rodrigues, M. V. B. Moreira, R. Paniago, R. Ribeiro-Andrade, R. Magalhães-Paniago, H.-D. Pfannes, and A. G. de Oliveira, 2008, Identification and quantification of iron silicide phases in thin films, J. Vac. Sci. Technol. A 26, 1138-1148.

Chapter Four:

Studying the effect of doping hematite with metal ions for environmental application

Abstract

Humidity sensors have several applications in both industrial processing and environmental control. Pure and doped hematite have proved to exhibit remarkable humidity sensing properties. The aim of this part of my Ph.D. thesis is to study the effect of doping with some metal ions (Li^{+},Mg^{+2}, Ba^{+2}, Sr^{+2}, and Na^{+}) crystalline hematite and to determine their sensitivity towards humidity. The obtained crystalline samples were characterized by X-Ray Diffraction (XRD) combined with Field Emission Scanning Electron Microscopy (FESEM). The doped sodium metal ions (Na^{+}) hematite sample showed a significant response towards relative humidity at room temperature.

4.1 Introduction

Adding metal ions to humidity sensing materials have been widely reported in literature due to their abundance in nature and efforts were exerted to investigate their effects [1]. Doping with metal ions affects the microstructure and creates surface defects or oxygen vacancies in the sensing material [2-4]. Ferric oxide has a wide range of applications as a magnetic material [5], in addition, it is very sensitive to humidity thus, it can be used as a humidity sensing material [6]. α-Fe_2O_3 is an n-type semiconductor, it is the most stable iron oxide under ambient conditions and it is nontoxic, corrosion-resistant, low cost and abundant. These features drove it into numerous promising applications, such as catalysts/photocatalysts [7-9], contrast reagents/drug delivery [10] and gas sensors [11]. Nanocomposite materials containing α-Fe_2O_3 doped with noble metals (e.g., Pd, Pt, and Au) can lead to a synergetic effect depend on the preparation condition, chemical composition, sintering temperature, sintering time and doping of additives [12]. Different techniques were used for producing hematite films on the solid substrate like sputtering [13], laser ablation[14], electrodeposition [15], spray pyrolysis (SP) [16, 17], ion beam induced chemical vapor deposition (IBICVD) [18], plasma enhanced chemical vapor deposition (PECVD) [19], and the aerosol- assisted chemical vapor deposition (AACVD) [20]. The aim of this part of my Ph.D. thesis is to investigate the doping effect of some metal ions (Mg^{+2}, Ba^{+2}, Sr^{+2}, Li^{+}, and Na^{+}) onto hematite and to determine the sensitivity towards humidity of these materials. The investigated sensors were prepared by screen printing technique.

4.2 Experimental

4.2.1 Powder synthesis

All reagents were ACS grade from Sigma-Aldrich. 1 mole of α-Fe_2O_3 powder (Aldrich >99%, particle size distribution lower than 2 μm) was dispersed in distilled water, then a dispersing agent was added (Darvan C 2 wt% of the used powder), prior to ultrasonication for 2 h in an ultrasonic bath. The prepared dispersed solution was mixed stepwise with 1.0 L aqueous solution of the salts of 1 M (for precipitation of metal hydroxide as the pH was adjusted with NaOH): Li_2CO_3, $MgCO_3$, $Ba(NO_3)_2$, $Sr(NO_3)_2$ and Na_2CO_3.

The dispersed solution was ultrasonicated again for 1 h, the solid content in solution was diluted to 4 wt% by adding distilled water. Finally, the dispersion was dried at 115°C overnight.

The dried powder was treated at 800°C for 1 h with a 2°C/min heating ramp. The powders were then manually ground by means of an agate mortar and an agate pestle before screen printing process.

4.2.2. Powder characterization

Particle size distribution was determined after powders calcination by means of a laser granulometer (D Malvern3600) and after dispersion in ethanol and sonication for 10 min. X-ray diffraction patterns were collected on powders by means of a X'Pert HighScore Philips Analytical Diffractometer, equipped with a Cu anticathode (λ Cu Kα anticathode= 0.154056 nm). Samples were scanned at a rate of 0.02°/s in the range from 5° to 70° in

2θafter calcinations of the prepared powder. Finally, samples were chromium sputtered for FESEM (Field Emission Scanning Electron Microscopy, Zeiss Merlin) investigations.

4.2.3. Humidity sensor preparation and testing

Sensors were screen printed onto an α- alumina substrates with platinum electrode fired at 980°C for 20 min. (with a 2°C/min heating ramp) [21, 22]. Screen printing inks were made of the doped α-Fe_2O_3 powders and an organic vehicle (Terpenol, Emflow, Emca Remex, USA), which confers the appropriate rheological properties to the paste.

After deposition samples were dried in air at room temperature prior to be heat treated at 800°C, (with a 2°C/min heating ramp) for 1 h. Humidity sensors were tested in a laboratory apparatus made of a thermostated chamber, operated at 25°C, in which relative humidity (RH) could be varied between 0 and 96% [23].

The laboratory apparatus for testing the sensors was calibrated to ensure a constant air flow during electrical measurements (0.05 L/s) and RH was varied by steps, each one of 3 min. An external alternating voltage (V = 3.6 V at 1 kHz) was applied on each tested sensor, acting as a variable resistance of the electrical circuit described above. A 2000 series Keithley digital multimeter was used to measure the tension V_{DC} at the output of the circuit.

The sensor resistance was determined by a calibration curve drawn substituting the sensors, in the circuit, by known resistances. The sensor response (SR), expressed in %, was defined as the relative variation of the starting resistance, compared with the resistance measured under gas exposure (eq. 1):

$$SR(\%) = 100\frac{|R_0 - Rg|}{R_0} \quad \text{(eq. 1)}$$

Where R_0 and R_g are the starting (in the absence of the test gas) and the gas exposed measured resistances of the sensors, respectively.

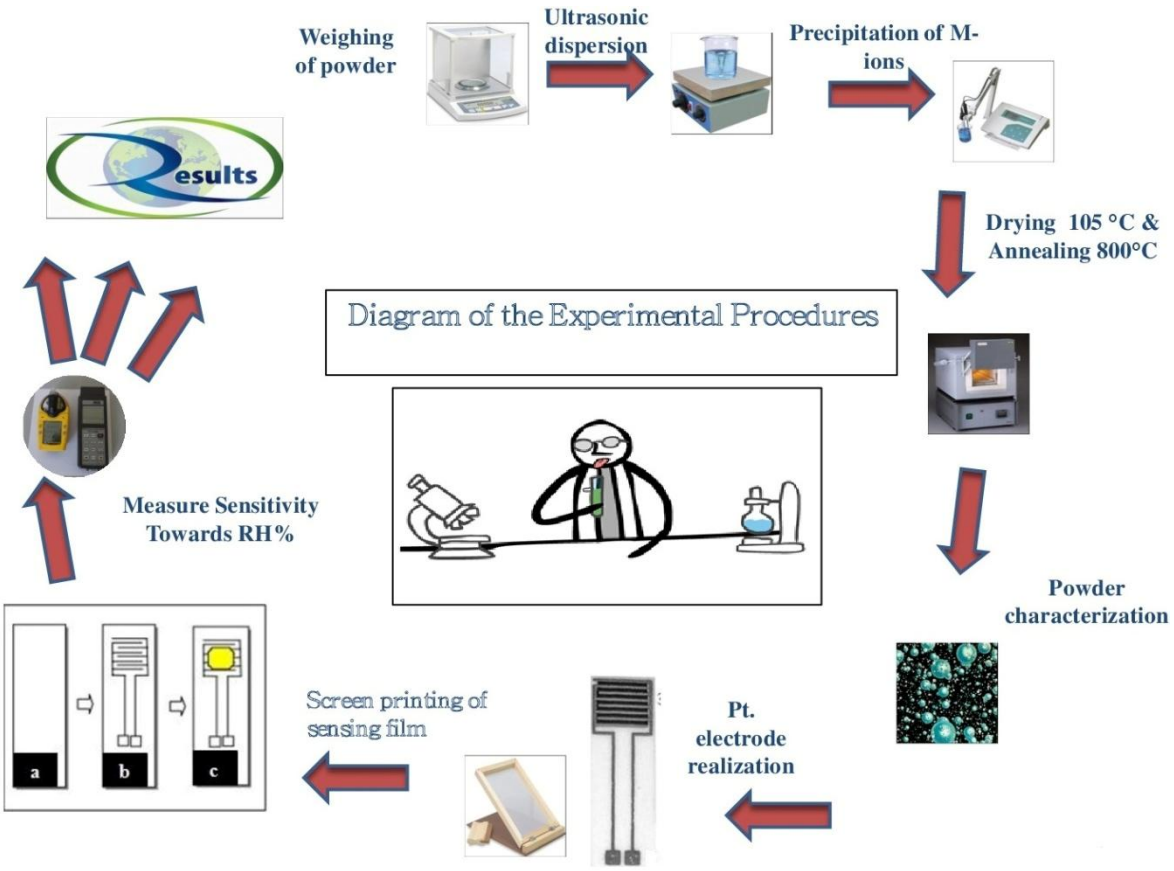

Fig. 1. Schematic diagram of the experimental procedures

4.3. Results and discussion

4.3.1. Materials characterization

4.3.1.1 Particle size distribution

Commercial α-Fe_2O_3 has particle size distribution lower than 2 µm. Generally, doped metal ion–hematite samples thermally treated at 800°C for 1 h present larger particle size distribution as shown in Table 1. This could be attributed to particles agglomeration during the drying process and the thermal treatment.

Cumulative wt%	Na^+ (α-Fe_2O_3) [µm]	Li^+ (α-Fe_2O_3) [µm]	Sr^{2+} (α-Fe_2O_3) [µm]	Ba^{2+} (α-Fe_2O_3) [µm]	Mg^{2+} (α-Fe_2O_3) [µm]
10%	7.03	5.58	5.61	14.55	1.92
50%	91.13	25.36	13.19	122.62	4.7
90%	149.2	85.33	65.88	220.72	19.19

Table1.Diameter of the doped metal ions hematite powders (µm)

When the cumulative weight below 90% of the hematite doped powder is less than 40 µm, the powder can pass through the openings of the screen-printing mesh (325 mesh). All powders were then sieved, except magnesium one, to obtain particle sizes below 40 µm as shown in Fig.2.

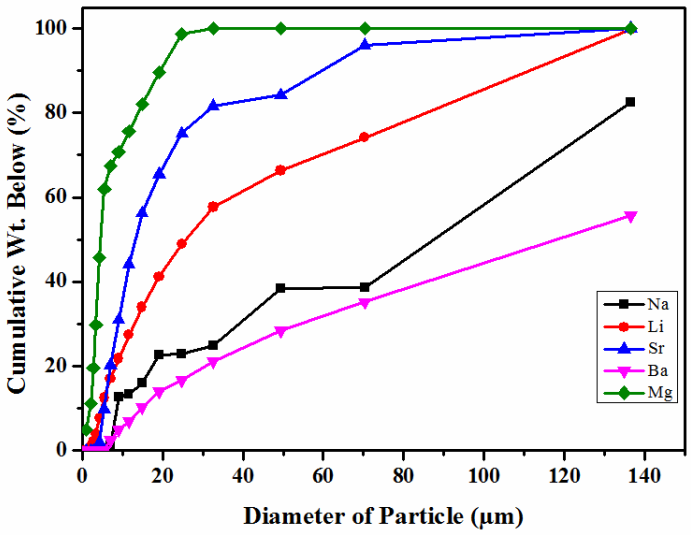

Fig.2. Particle size distribution of metal ions doped hematite powders

4.3.1.2 XRD measurements

For the sake of comparison with the metal-ions doped hematite, XRD pattern of the commercial used α-Fe_2O_3 powder is shown in Fig. 3a (indexed with JCPDS card n°33-664). XRD patterns of the different doped α-Fe_2O_3 powders present in Fig.3b, 3c, 4a, 4b showed well crystallized phases.

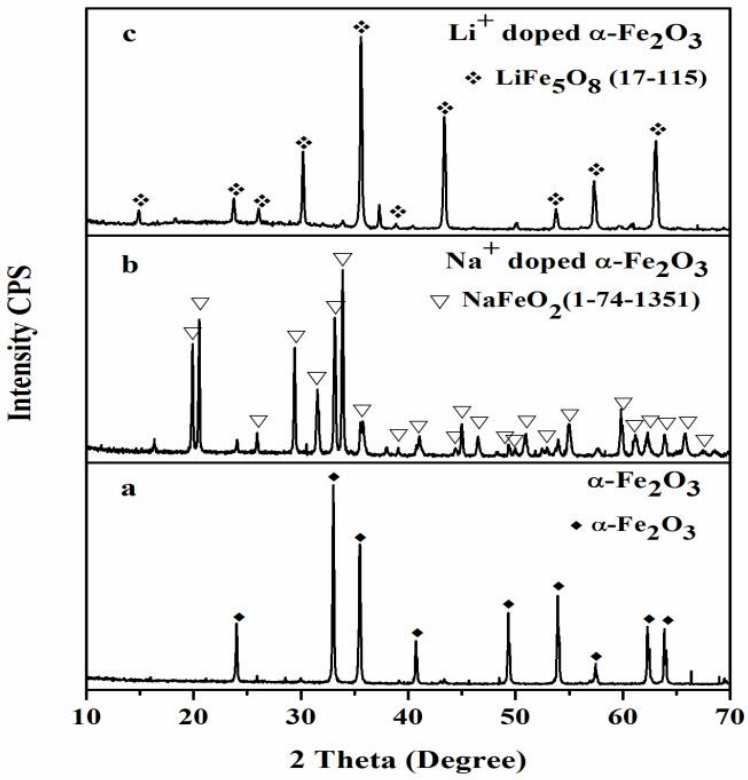

Fig.3. XRD pattern of a) α-Fe_2O_3, b) sodium-doped hematite and c) lithium-doped hematite

Sodium doped hematite was crystallized in $NaFeO_2$ form, according to JCPDS card n°1-74-1351.$LiFe_5O_8$ (JCPDS card n°17-115) with a cubic spinel structure derived from lithium-doped hematite [24].The $Sr_4Fe_6O_{13}$ phase was obtained according to JCPDS card n°1-78-2403 from strontium doped hematite sample. This phase formed when the powder is calcined above775°C, which matches the thermally treated powder at 800°C [25].

$Ba_{10}Fe_{10}O_{28}$ (JCPDS cards n°54-966) and $Fe_{1.9}Mg_{0.16}O_3$ (JCPDS cards n°1-70-2674) are detected inbarium and magnesium doped hematite, respectively.

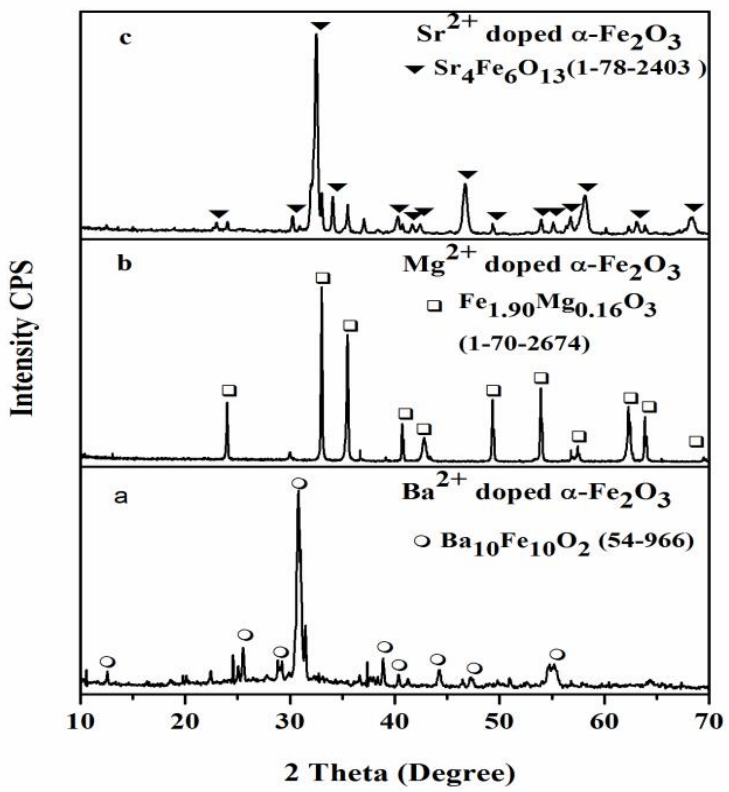

Fig.4. XRD pattern of a) barium-doped hematite, b) magnesium-doped hematite and c) strontium-doped hematite

4.3.1.3 FE-SEM observation and microanalysis

FESEM micrographs of unfired, fired at 800°C commercial hematite and as well as Na^{+} doped hematite heat treated at 800°C are shown in Figs.5a, 5b and 5c respectively in order to distinguish the morphological difference between them.

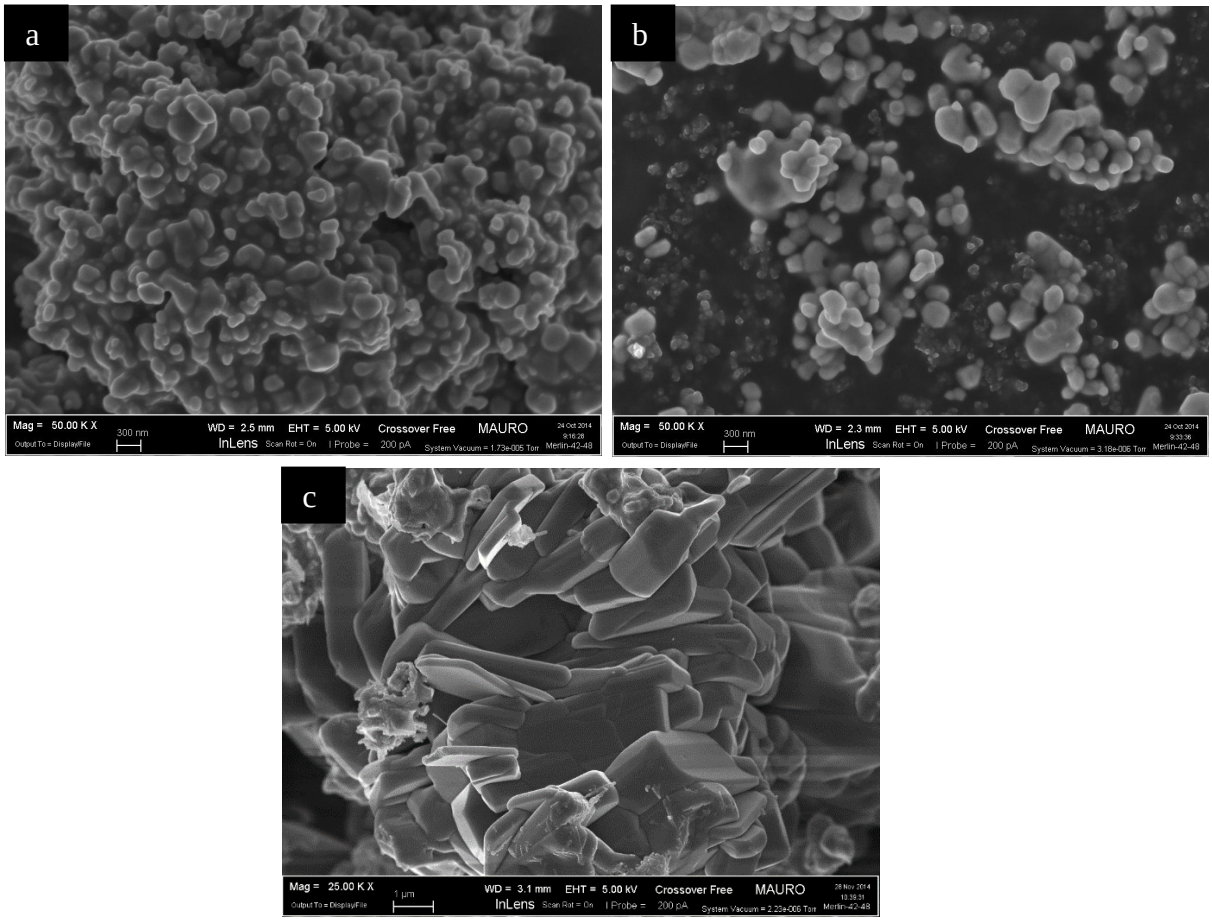

Fig. 5. FESEM micrographs of a) unfired hematite powder, b) hematite powder heat treated at 800°C for 1 h and c) Na^+ doped hematite heat treated at 800°C for 1 h.

According to the FESEM observations, unfired hematite appears denser with less porosity than fired hematite (Figs 5a, and 5b). Fired Na^+ doped hematite powder has the biggest grain size in comparison with the particle size of the fired and unfired pure hematite (Figs 5a, 5b and 5c). This could be attributed to the diffusion of sodium ions into the crystalline hematite lattice and to the resultant formation of the sodium ferrite, as well as to grain growth during heat treatment.

FESEM micrographs also showed that the fired sodium doped hematite film is characterized by well distributed porosity, which makes this material appropriate as a gas sensor.

4.3.2 Sensitivity towards humidity

Fig.6 illustrates the sensors' response towards RH. Among the different investigated samples, Na^{+} doped hematite showed a significant response towards RH at room temperature starting from 32% RH, while the other doped hematite samples show a poor sensitivity towards RH.

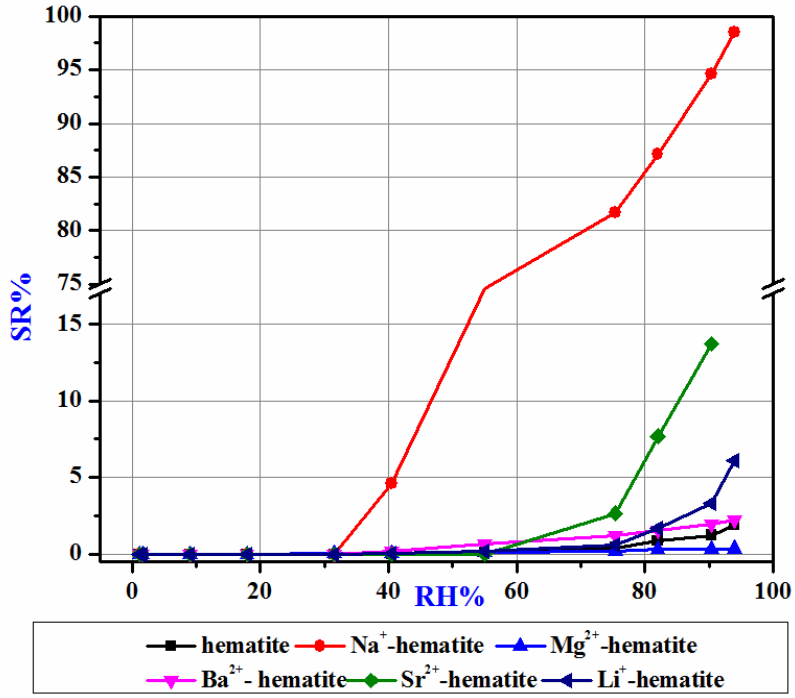

Fig.6. Sensors response toward relative humidity changes

From the change in V_{DC} in function of time reported inFig.7 response and recovery time can be estimated. The response times (the time taken by a sensor to achieve 90% of the total resistance change in the case of gas adsorption) and the recovery times (the time necessary to reach 90% of the total resistance changes in the case of gas desorption) are reported in Table 3. These response and recovery times are quite fast.

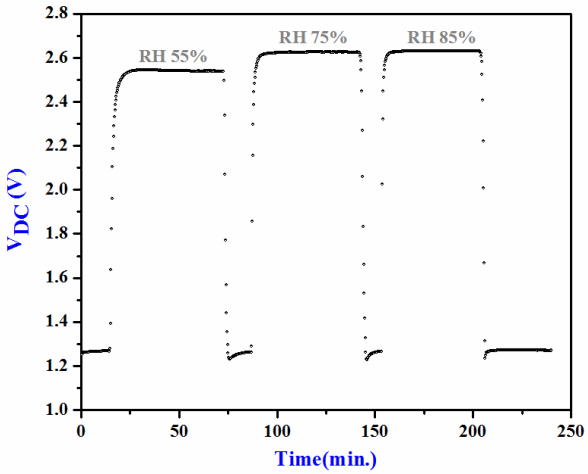

Fig.7. Changes in V_{DC} in function of relative humidity changes at room temperature of Na^+ doped hematite sensor.

Humidity change	*0-55% RH*	*0-75% RH*	*0-85% RH*
Response time (min.)	2.5	2.1	1.2
Humidity change	*55-0% RH*	*75-0% RH*	*85-0% RH*
Recovery time (min.)	1.0	2.5	2.5

Table 3. Response and recovery time of the Na^+ doped hematite based sensor

4.4. Conclusion

A simple and low cost chemical method was used for synthesizing different alkali and alkaline-earth metals doped hematite. Screen printing technique was used to prepare humidity sensors with the prepared powders.

Doping hematite with metal ions can lead to surface defects or oxygen vacancies and introduces in the sensing material ions which possess high local charge density able to increase the adsorption sites for water vapor. Among the investigated compositions, Li^{+}, Mg^{+2}, Ba^{+2}, and Sr^{+2} doped hematite based sensors exhibited low sensitivity towards RH. On the contrary, Na^{+} doped hematite based sensor showed a significant response towards RH.

Further work should be devoted to improve the response of the sodium doped hematite to lower RH values and to examine its selectivity towards other gases such as NO_x and CO_2, for example. Durability should be investigated too.

References

1. E. Traversa, *Sens. Actuators B*, **23**, 135 (1995).

2. T. Y. Kim, D. H. Lee, Y.C. Shim, J. U. Bu, S. T. Kim, *Sens. Actuators*, B, **9**, 221(1992).

3. Y. C. Yek, T. Y. Tseng, *IEEE Trans. Compon. Hybrids Manufact. Technol.*, **12**, 259 (1989).

4. B. M. Kulwicki, *J. Am. Ceram. Soc.*, **74**, 697 (1991).

5. S. S. Nair, M. Mathews, P. A. Joy, S. D. Kulkarni, M. R. Anantharaman, *J. Mag. Mag. Mater.*,**283**, 344 (2004).

6. C. L. Zhu, Y. J. Chen, R. X. Wang, L. J. Wang, M. S. Cao, X. L. Shi, *Sens. Actuators B*,**140**, 185 (2009).

7. Weiss, W., Zscherpel, D., Schlögl, R., *Catal. Lett.*, **52**, 215 (1998).

8. Faust, B. C., Hoffmann, M. R., Bahnemann, D.W., *J. Phys. Chem.*, **93**, 6371(1989).

9. Ohmori, T., Takahashi, H., Mametsuka, H., Suzuki, E., *Phys. Chem. Chem. Phys.*, **2**, 3519 (2000).

10. Gupta, A. K., Gupta, M., *Biomaterials*,**26**, 3995 (2005).

11. Comini, E., Guidi, V., Frigeri, C., Riccò, I., Sberveglieri, G., *Sens. Actuators B*,**77**,16 (2001).

12. A. Y. Lipare, P. N. Vasambekar, A. S. Vaingankar, *J. Magn. Magn Mater*, **279**, 160 (2004).

13. E. L. Miller, D. Paluselli, B. Marsen, R. E. Rocheleau, *Thin Solid Films*, **466**, 307 (2004).

14. F. Zhou, S. Kotru, R. K. Pandey, *Thin Solid Films*, **408**, 33 (2002).

15. Y. S. Hu, A. Kleiman-Shwarsctein, A. J. Forman, D. Hazen, J. N. Park, E.W. McFarland, *Chem. Mater.*, **20**, 3803 (2008).

16. A. Duret, M. Grätzel, *J. Phys. Chem. B.*, **109**, 17184 (2005).

17. F. Le Formal, M.M. Grätzel, K. Sivula, *Adv. Funct. Mater.*, **20**, 1099 (2010).

18. L. Yuberto, M. Ocaña, A. Justo, L. Conttreras, A. R. González-Elipe, *J. Vac. Sci. Technol. A*, **18**, 2244 (2000).

19. B. J. Kim, E. T. Lee, G. E. Jang, *Thin Solid Films*, **341**, 79 (1999).

20. A. A. Tahir, K.G. Upul Wijayantha, S. Saremi-Yarahamadi, M. Mazhar, V. McKee, *Chem. Mater.*, **21**, 3763 (2009).

21. J. Savage, Handbook of Thick Film Technology, P. J. Holmes, R.G. Loasby Eds., Electrochemical Publications Ltd., Scotland, 1976, p. 51.

22. W. Qu, *Solid State Ionics*, **83**, 257 (1996).

23. M. Viret, D. Rubi, D. Colson, D. Lebeugle, A. Forget, P. Bonville, G. Dhalenne, R. Saint-Martin, G. Andre´, F. Ott, *Mater. Res. Bull*., **47**, 2294 (2012).

24. F. O. Ernst, H. K. Kammler, A. Roessler, S. E. Pratsinis,W. J. Stark, J. Ufheil, P. Nova´k, *Mater. Chem. Phys.*, **101**, 372 (2007).

25. Anita Fossdal, Mari-Ann Einarsrud, Tor Grande, *J. Solid State Chem.,* **177**, 2933 (2004).

Chapter Five:

Fabrication of humidity sensor based on carbon films by using micro carbonized bamboo

Abstract

In this part of my Ph.D. thesis, eco-friendly, low cost and efficient humidity sensors were prepared from micro-sized pyrolyzed bamboo. Two types of pyrolyzed particles were investigated: as such (CB) and annealed ones (CBA). After pyrolysis, the materials were first manually ground and then, attrition milled. The synthesized particles were characterized by using field emission-scanning electron microscopy, Raman spectroscopy, specific surface area (SSA) measurements and thermogravimetric analysis. The sensing materials were screen-printed onto commercial α-alumina substrates with platinum electrodes prior to firing at 300°C for 1 hour. The humidity sensing properties of the pyrolyzed bamboo based sensors were investigated at room temperature in the relative humidity (RH) range from 0.0 to 96.0%. The pyrolyzed bamboo based humidity sensors exhibited an excellent response towards humidity starting from 10% RH, while CBA showed a response starting from 20% RH. These differences can be explained on the basis of SSA results: annealing led to drastic reduction of open porosity. Finally, the response and recovery times were reasonably fast (less than 2 minutes).

5.1 Introduction

The most common types of humidity sensors are composed of metal oxide semiconductors, conducting polymers, carbon nano-tubes and graphene oxides in which the adsorption of water vapor changes the electrical properties such as resistivity and capacity of the device [1-10].However, most of these sensors have some limitations such as high costs and complicated manufacturing process or limited humidity sensing range. To meet these challenges, I developed a new type of humidity sensor from micro carbonized bamboo particles (CB), as biomass is a qualified carbon raw material for the synthesis of valuable carbon materials because it is available in high quality and huge amount, and it is an environmental friendly renewable resource. Moreover, there are very few papers in the literature dealing with gas sensors from pyrolized carbonaceous raw materials.

5.2. Experimental procedures

5.2.1. Micro carbonized particles synthesis

The bamboo, used for the production of micro-sized carbonized particles was obtained from the Piedmont region, Italy. The schematic diagram of the synthesis of micro-sized carbonized particles is shown in Figure 1. The bamboo pieces were chopped down into small (~1-5 mm) fragments to obtain higher surface area in subsequent operations. The chopped bamboo pieces were washed with distilled water and dried in an oven for 48 h at 105±5^{o}C. The dried bamboo pieces were immersed in 0.25M (1% w/v) aqueous solution of sodium hydroxide (NaOH) for 10 days to achieve partial disintegration of the

cellulosic structure of thebamboo material. Literature shows that chemically treated bamboo can produce micro sized inert carbonized particles of improved quality [11, 12]. After chemical treatment, the bamboo pieces were washed with distilled water and dried in an oven. The dried bamboo pieces were further pyrolyzed in a quartz reactor at 800°C for 1 h under an inert atmosphere. A flow of argon gas (50mL/min) was used to maintain the inert atmosphere. During pyrolysis, the heating ramp of the furnace was kept at 10°C/min.

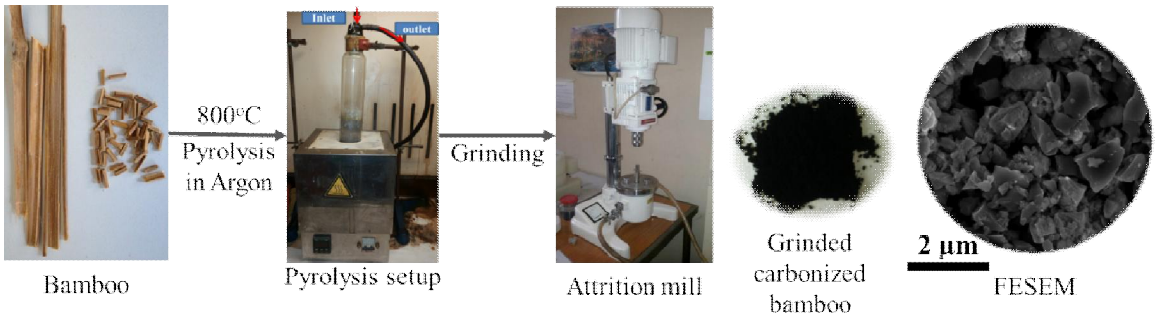

Fig.1. Schematic diagram of carbonized bamboo particles synthesis

After the completion of pyrolysis, the CB and carbonized bamboo annealed at 1000°C (CBA)pieces were manually grounded in an agate mortar with an agate pestle and then with the help of an attrition mill. In the process of attrition milling, 2 mm diameter alumina balls were used for 1 h with distilled water as grinding media. The finally pulverized material was dried in an oven and stored in airtight containers for further use.

5.2.2. Characterization of carbonized bamboo

Particle size distribution of CB and CBA powder was determined by laser granulometry (Malvern 3600D, Great Britain) after dispersing the carbonized bamboo in ethanol with the help of sonication (10 min in an ultrasonic bath).

Thermo-gravimetric (TGA, Mettler 851, Switzerland) analysis on raw bamboo, CB and CBA was carried out to study their thermal degradation behavior in pyrolysis. The temperature range of 25-1000°C was set with a heating ramp rate of 10°C/min. The analysis was performed in an inert atmosphere by using argon (30 mL/min) and under an oxidising atmosphere based onsynthetic air (30 mL/min).

Specific surface area (SSA) were measured by N_2 physisorption at -196°C (Micrometrics ASAP 2020, USA) on samples previously outgassed at 200°C for 4 h to remove water and other atmospheric contaminants.SSA was calculated using the BET method and pore diameters were evaluated by applying the Barrett-Joyner-Halenda (BJH) algorithm to isotherms desorption branch.

X-ray diffraction patterns were collected on powders by means of a X'PertHighScore Philips Analytical Diffractometer, equipped with a Cu anticathode (λ Cu Kα anticathode= 0.154056 nm). Samples were scanned at a rate of 0.02°/s in the range from 5° to 70° in 2θ.

The CB particles were also analyzed by Raman spectroscopy (Renishaw Micro-Raman, United Kingdom) with a green laser (514.5 nm wavelength).

The surface and structural morphology, and elemental composition were analyzed by Field emission scanning electron microscopy (FESEM, ZeissSupra-40, Germany) equipped with energy dispersive X-ray spectroscopy (EDX).

The powders were submitted to X-ray diffraction (XRD) analysis. Patterns were recorded on a Pan'AnalyticalX'Pert Pro instrument (Pan'Analytical, The Netherlands) operating with Cu K□ radiation (0.1541874 nm) and acquired in the range 5–70° 2θ. Diffraction patterns were indexed by using the software X'PertHighscore from Pan'Analytical (ver. 1.0c).

5.2.3 Preparation of humidity sensors

The humidity sensors were screen-printed ontoα-alumina substrates with interdigitated platinum electrodes fired at 980°C for 15 min. (with a 2°C/min heating ramp). Screen printing inks were preparedfrom the carbonized bamboo powderdispersed in an organic vehicle (Terpenol, Emflow, Emca Remex, USA), which provides the appropriate rheological properties to the paste/ink. After screen printing,the humidity sensors were dried in air at room temperature before being heat-treated at 300°C (with a 2°C/min heating and cooling ramp) for 1h.

Finally, sensors were tested to study their response to relative humidity (RH) in a laboratory apparatus made of a thermostated chamber, operated at 25°C. RH can vary between 0 and 96% by steps, each one of three minutes. The laboratory apparatus for testing the sensors was calibrated to ensure a constant airflow during the electrical measurements (0.05 L/s).

5.2.4. Performance testing of humidity sensors

During measurements under variable RH atmospheres, the sensors resistance was determined by means of a LCR meter (Hioki 3533-01, Japan). During the measurements, the sensors were alimented by an AC tension of 1 V at 1 kHz. The sensor response (SR), expressed in %, is defined as the relative variation of the starting resistance (R_0), compared with the resistance measured under gas/humidity (R_g) exposure (eq. 1):

$$SR(\%) = 100 \frac{|R_0 - Rg|}{R_0} \qquad \text{(eq. 1)}$$

Where R_0 and R_g are the starting (in the absence of the test gas) and the gas exposed measured resistances of the sensors, respectively.

5.3. Results and discussions

5.3.1. Materials characterization

5.3.1.1 Particle size distribution

Results after pyrolysis of the bamboo and grinding in attrition milling show that the particle size d_{50} is in the range 1-2 µm as illustrated in Table 1.

Cumulative wt%	Pyrolyzed Bamboo Diameter (µm)	Annealed Bamboo Diameter (µm)
10%	1	1
50%	1.7	2.3
90%	3.9	5.07

Table 1. Diameter in micron of the carbonized bamboo.

5.3.1.2 TGA results

Analysis of the raw and treated bamboo was carried out, and their mass loss curves are presented in Fig. 2.

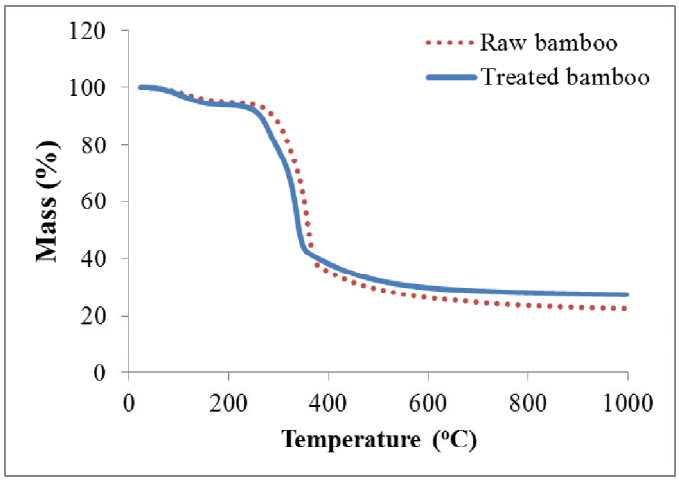

Fig. 2. Thermogravimetric analysis of the raw and treated bamboo under argon

The results indicate that the mass losses of the untreated and treated bamboodividedinto three temperature ranges (Table 2).In the first temperature range 25-220°C, mass loss occurs due to the evaporation of the moisture from the organic material [13].

In the second temperature range 220-375°C, where major weight loss was observed,there is the simultaneous decomposition of hemicellulose and cellulose and the partial decomposition of lignin [14-16]. In the last temperature range 375-1000°C, a slow mass loss was observed due to the decomposition of lignin in the bamboo. The yield of carbonized material obtained from raw and treated bamboo was 27.3% and 22.4% respectively. The thermal decomposition of chemically treated bamboo showed higher weight losses in second and third temperature ranges as of untreated bamboo. This

phenomenon is attributed to the partial degradation of cellulose, lignin and other organic impurities from the chemical treatment process before pyrolysis [11].

Pyrolysis characteristic	First step			Second step			Third step			Residue
	Start	**End**	**Mass loss**	**Start**	**End**	**Mass loss**	**Start**	**End**	**Mass loss**	
	(^{o}C)	**(^{o}C)**	**(%)**	**(^{o}C)**	**(^{o}C)**	**(%)**	**(^{o}C)**	**(^{o}C)**	**(%)**	**(%)**
Raw bamboo	25	220	**6.44**	220	375	**53.12**	375	1000	**13.11**	**27.33**
Treated bamboo	25	220	**5.29**	220	375	**57.04**	375	1000	**15.68**	**22.42**

Table 2: Thermal degradation behavior of bamboo in Argon

The carbonized and pulverized bamboo was analyzed by TGA under a constant flow of air to qualitatively assess the purity of the carbonized material (Fig. 3). It was observed that the material is sufficiently stable up to 400°C under air. The treated carbonized bamboo started to oxidize at 400°C, as confirmed by its DTG curve (Figure 3).

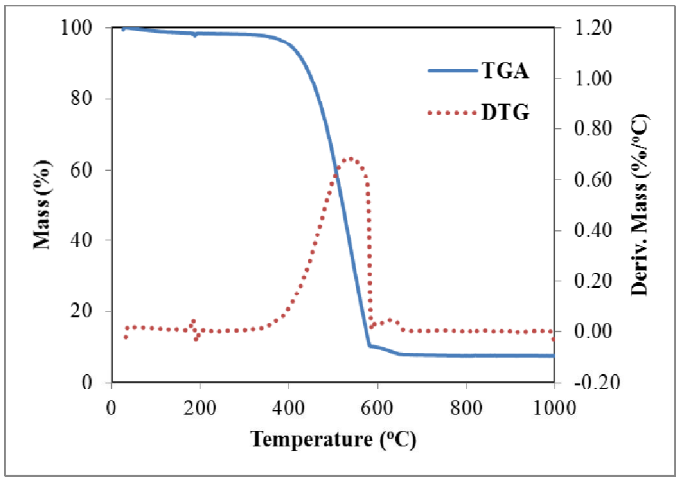

Fig.3:TGA curve of treated carbonized bamboo particles under air

5.3.1.3 BET results

Specific surface area (SSA) of CB is higher than that of CBA (Table 3) as annealing led to drastic reduction of open porosity.

Sample	S.S.A(m^2/g)
CB	17.23
CBA	0.47

Table 3: Specific surface area of carbonized bamboo (CB) and of carbonized and annealed bamboo (CBA).

5.3.1.4 XRD results

XRD patterns revealed that both CB (not shown here) and CBA powders were amorphous.

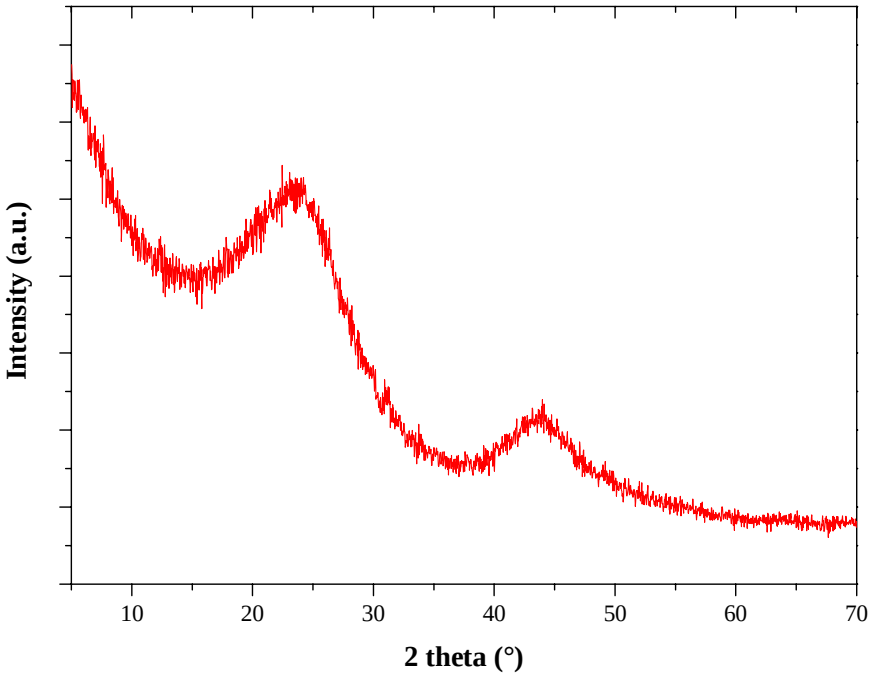

Fig. 4: XRD pattern of annealed bamboo powder (CBA)

5.3.1.5 Raman analysis

In the Raman spectrum (Fig. 5), two distinct peaks of the disordered carbon (sp^3) (D-band) at1350cm^{-1} and graphitic (sp^2) band (G-band) at 1600 cm^{-1}were observed. The intensity ratio of D and G peaks (I_D/I_G) is usually referred to the quality of the material. For carbonized bamboo, the I_D/I_G ratio is 0.77 indicating the presence of defects in the structure of the material [17, 18].

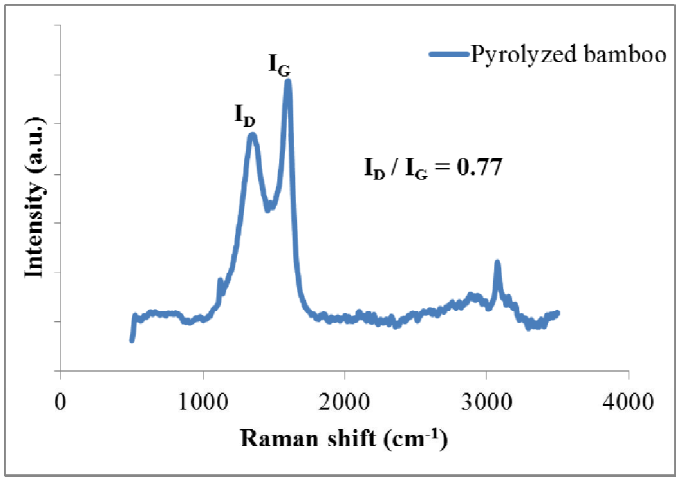

Fig. 5: Raman spectrum of carbonized bamboo powder

5.3.1.6 FESEM

The FESEM observations were conducted on treated and pulverized carbonized bamboo (Figure 6).The grinding process of the carbonized bamboo produced small fragments ranging from 100 nm to 2.0 µm, in agreement with laser granulometry results. The particles are angular with sharp edges, as expected in a fragile material after grinding, and show a glossy/smooth surface.

a)

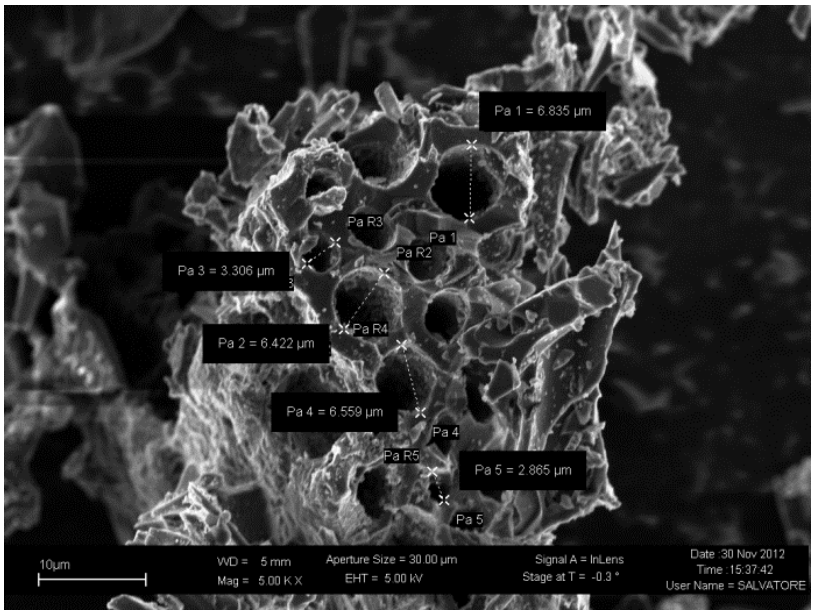
Pa 1 = 6.835 µm
Pa R3
Pa 1
Pa R2
Pa 3 = 3.306 µm
Pa R4
Pa 2 = 6.422 µm
Pa 4 = 6.559 µm
Pa 4
Pa R5
Pa 5 = 2.865 µm
Pa 5
10µm
VVD = 5 mm
Mag = 5.00 K X
Aperture Size = 30.00 µm
EHT = 5.00 kV
Signal A = InLens
Stage at T = -0.3 °
Date :30 Nov 2012
Time :15:37:42
User Name = SALVATORE

b)

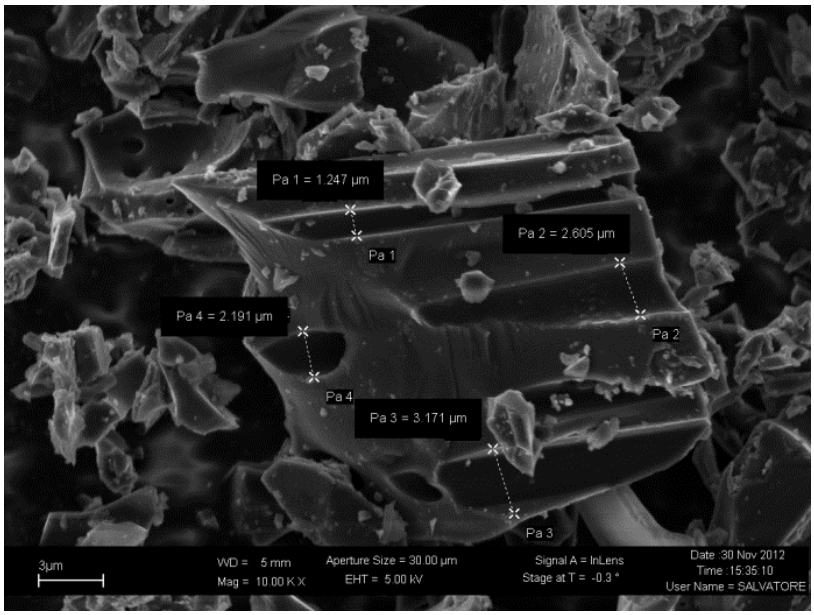
Pa 1 = 1.247 µm
Pa 1
Pa 2 = 2.605 µm
Pa 4 = 2.191 µm
Pa 2
Pa 4
Pa 3 = 3.171 µm
Pa 3
3µm
VVD = 5 mm
Mag = 10.00 K X
Aperture Size = 30.00 µm
EHT = 5.00 kV
Signal A = InLens
Stage at T = -0.3 °
Date :30 Nov 2012
Time :15:35:10
User Name = SALVATORE

c)

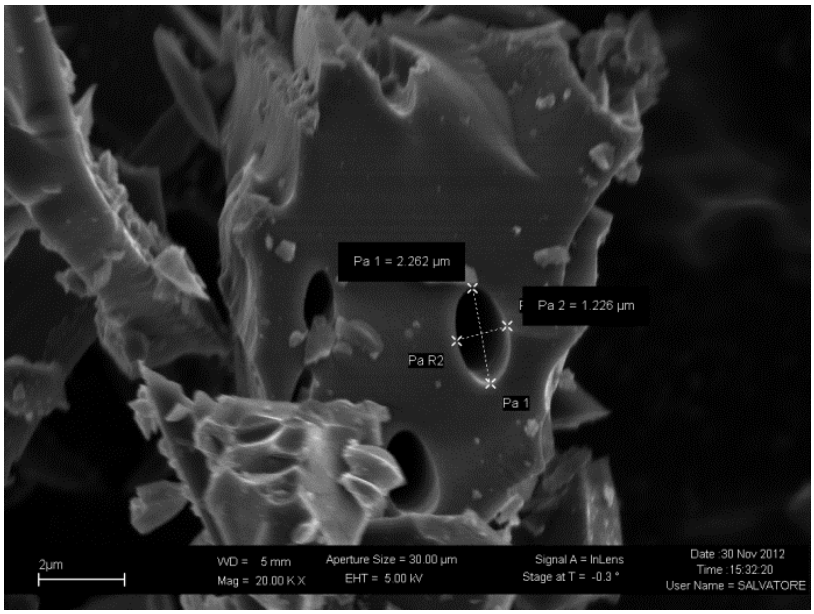

d)

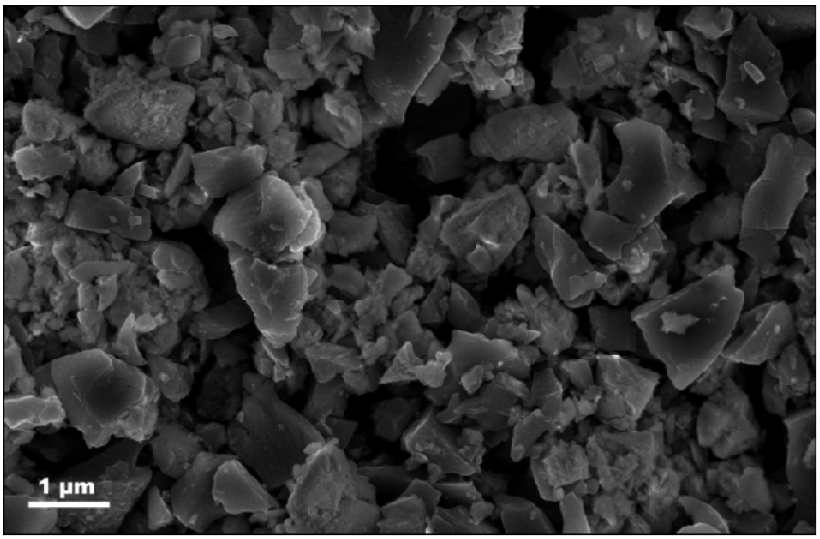

Figure 6: FESEM micrograph of treated carbonized bamboo (CB)after:a), b), c) manual grinding and d) after attrition milling

The elemental analysis (Table 4) of the powder CB indicated the presence of a substantial amount of carbon with few traces of silica and calcium as impurities.

Element	Carbon (C)	Oxygen (O)	Silica (Si) %	Calcium (Ca) %
Content (%)	**76.58**	**21.88**	**0.81**	**0.73**

Table 4: Elemental composition of treated carbonized bamboo

5.3.2. Electrical characterization of the carbonized bamboo based humidity sensors under different relative humidity (RH) conditions

Fig. 7 illustrates the sensors' response towards RH. CB showed a significant response towards RH at room temperature starting from 10% RH, while CBA shows a lower response towards RH starting from 20% RH. These differences can probably be explained on the basis of BET results: CB presents a much higher SSA respect to CBA (Table 3).The sensors resistance started from about 937 kOhm at 0% RH and decreased to 89 kOhm at 95% RH for CB (Fig. 8).

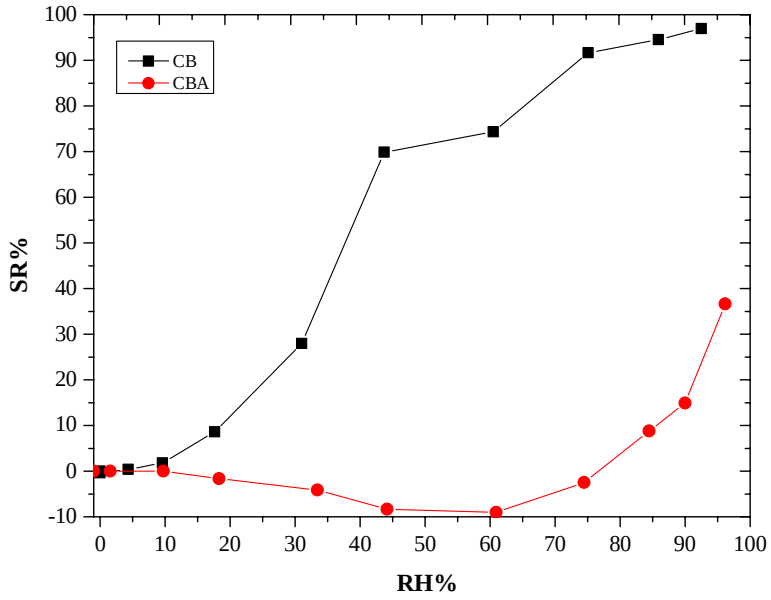

Fig.7: Sensors response toward relative humidity at room temperature

The response times (the time taken by a sensor to achieve 90%of the total resistance change in the case of gas adsorption) and the recovery times (the time necessary to reach 90% of the total resistance changes in the case of gas desorption), determined from the measurements reported in Fig. 8, are quite fast(about 2 min) and are reported in Table 5.

Recovery times are always shorter respect to response times (Table 5). Short response times may be due to the porosity of the film which gives accessibility for water molecules. Fast recovery times indicate that probably only the process of physisorption is the major reason for binding water molecules with the sensing materials.

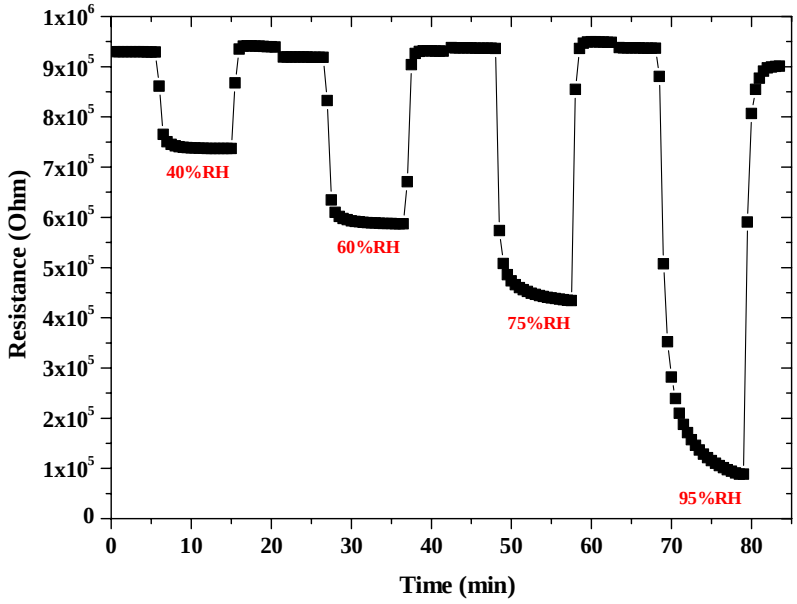

Figure 8: Response and recovery time of CB sensors

Response time	Min
From 0% to 40% RH	1.9
From 0% to 60% RH	2.1
From 0% to 75% RH	2.3
From 0% to 95% RH	2.7
Recovery time	**min**
From 40% to 0% RH	1.3
From 60% RH a 0% RH	1.6
From 75% RH a 0% RH	1.8
From 95% RH a 0% RH	2

Table 5: Response and recovery times of PB sensor

Finally, no ageing of the films was observed, as measurements repeated three months later confirmed the same results.

Water molecules can be adsorbed on the surface of C films because the hydrogen in water molecules can form a weak bond with one of the surface C atoms [20]. Moreover, the sensing performance can be improved by the presence of defects in carbon grains, as evidenced by Raman spectrum (Fig. 5). These defects can also act as sites for water molecules adsorption [20]. Pati et al. [21] reported that charge can transfer between the adsorbate and the C film. A quantitative analysis based on Mulliken approach showed a charge transfer of $0.03e^-$ from a single H_2O molecule to C film [22]. Thus, the more water molecules can be adsorbed on the surface, the more charge transfer happens between the water molecules and number of C.

Cross-sensitivity measurements were finally performed with respect to N_2O (150 ppm in He), CO_2 (500 ppm in He) and NH_3 (500 ppm in He). The variation of the resistance of the CB sensor exposed for 10 min to helium containing the different gases was compared to its response under pure helium after the same time (Table 6).

Gas	Resistance (kOhm)	Sensor response (%)
Pure He	914	---
N_2O (150 ppm in He)	798	12.7
CO_2 (500 ppm in He)	574	37.2
NH_3 (500 ppm in He)	1043	14.1

Table 6: Variation of CB sensor resistance with respect to some gases

Some interference with the investigated gases were then evidenced, in particular with carbon dioxide. The value of the measured resistance under 500 ppm of CO_2 (Table 6) was close to the one observed under air having 60% RH (Fig. 8). The selectivity of this sensing material need to be improved.

5.4. Conclusions

Biomass is a qualified carbon raw material for the synthesis of valuable carbon materials because it is available in high quality and huge amount, and it is an environmental friendly renewable resource. Moreover, different residues of biomass pyrolysis are becoming available from pilot plants producing energy.

Thus, in this part of my PhD research, a new sensing material based on pyrolyzed bamboo was successfully prepared by a simple and low-cost process. The humidity sensing properties of the pyrolyzed bamboo based sensors were investigated at room temperature in the relative humidity (RH) range from 0.0 to 96.0%. The pyrolyzed bamboo based humidity sensors exhibited an excellent response towards humidity starting from 10% RH, while CBA showed a response starting from 20% RH. These differences can be explained on the basis of SSA results: annealing led to drastic reduction of open porosity.

Finally, the response and recovery times were reasonably fast (less than 2 minutes). However, the selectivity of the CB sensor must be improved with respect to carbon dioxide

References

[1] Islam T, Nimal AT, Mittal U, Sharma MU. A micro interdigitated thin film metal oxide capacitive sensor for measuring moisture in the range of 175–625ppm. Sensors Actuators B Chem 2015;221:357–64. doi:10.1016/j.snb.2015.06.101.

[2] Nanto H, Minami T, Takata S. Zinc-oxide thin-film ammonia gas sensors with high sensitivity and excellent selectivity. J Appl Phys 1986;60:482–4. doi:10.1063/1.337435.

[3] Kim Y, Jung B, Lee H, Kim H, Lee K, Park H. Capacitive humidity sensor design based on anodic aluminum oxide. Sensors Actuators, B Chem 2009;141:441–6. doi:10.1016/j.snb.2009.07.007.

[4] Balde M, Vena A, Sorli B. Fabrication of porous anodic aluminium oxide layers on paper for humidity sensors. Sensors Actuators B Chem 2015;220:829–39. doi:10.1016/j.snb.2015.05.053.

[5] Feng X, Chen W, Yan L. Sensors and Actuators B : Chemical Free-standing dried foam films of graphene oxide for humidity sensing. Sensors Actuators B Chem 2015;215:316–22. doi:10.1016/j.snb.2015.03.068.

[6] Fernández-Ramos MD, Ordóñez YF, Capitán-Vallvey LF, Vargas-Sansalvador IMP De, Ballesta-Claver J. Optical humidity sensor using methylene blue immobilized on a hydrophilic polymer. Sensors Actuators B Chem 2015;220:528–33. doi:10.1016/j.snb.2015.06.006.

[7] Jung DY, Yang SY, Park H, Shin WC, Oh JG, Cho BJ, et al. Interface engineering for high performance graphene electronic devices. Nano Converg 2015;2:11. doi:10.1186/s40580-015-0042-x.

[8] Phan D-T, Chung G-S. Effects of rapid thermal annealing on humidity sensor based on graphene oxide thin films. Sensors Actuators B Chem 2015;220:1050–5. doi:10.1016/j.snb.2015.06.055.

[9] Su P-G, Shiu W-L, Tsai M-S. Flexible humidity sensor based on Au nanoparticles/graphene oxide/thiolated silica sol–gel film. Sensors Actuators B Chem 2015;216:467–75. doi:10.1016/j.snb.2015.04.070.

[10] Su PG, Wang CS. Novel flexible resistive-type humidity sensor. Sensors Actuators, B Chem 2007;123:1071–6. doi:10.1016/j.snb.2006.11.015.

[11] Awwad E, Mabsout M, Hamad B, Farran MT, Khatib H. Studies on fiber-reinforced concrete using industrial hemp fibers. Constr Build Mater 2012;35:710–7. doi:10.1016/j.conbuildmat.2012.04.119.

[12] Ahmad S., Khushnood RA, Jagdale P., Tulliani J., Ferro GA. High performance self-consolidating cementitious composites by using micro carbonized bamboo particles. Mater Des 2015;76:223–9. doi:10.1016/j.matdes.2015.03.048.

[13] Oyedun AO, Lam K, Gebreegziabher T, Hui C. Kinetic Modelling and Analysis of Waste Bamboo Pyrolysis. Chem Eng Trans 2012;29:697–702. doi:10.3303/CET1229117.

[14] Lopez-Velazquez MA, Santes V, Balmaseda J, Torres-Garcia E. Pyrolysis of orange waste: A thermo-kinetic study. J Anal Appl Pyrolysis 2013;99:170–7. doi:10.1016/j.jaap.2012.09.016.

[15] Byrne CE, Nagle DC. Carbonization of wood for advanced materials applications. Carbon N Y 1997;35:259–66. doi:10.1016/S0008-6223(96)00136-4.

[16] Kercher AK, Nagle DC. Microstructural evolution during charcoal carbonization by X-ray diffraction analysis. Carbon N Y 2003;41:15–27. doi:10.1016/S0008-6223(02)00261-0.

[17] Jiang Z, Liu Z, Fei B, Cai Z, Yu Y, Liu X. The pyrolysis characteristics of moso bamboo. J Anal Appl Pyrolysis 2012;94:48–52. doi:10.1016/j.jaap.2011.10.010.

[18] Malard LM, Pimenta MA, Dresselhaus G, Dresselhaus MS. Raman spectroscopy in graphene. Phys Rep 2009;473:51–87. doi:10.1016/j.physrep.2009.02.003.

[19] Park JS, Reina A, Saito R, Kong J, Dresselhaus G, Dresselhaus MS. band Raman spectra of single, double and triple layer graphene. Carbon 2009;47:1303–10. doi:10.1016/j.carbon.2009.01.009.

[20] Chu J, Peng X, Feng P, Sheng Y, Zhang J, Study of humidity sensors based on nanostructured carbon films produced by physical vapor deposition. Sensors and Actuators B 2013; 178: 508– 513.

[21] Pati R, Zhang Y, Nayak SK, Ajayan PM, Effect of H2O adsorption on electrontransport in a carbon nanotube. Applied Physics Letters 2002; 81:2638–2640

[22] Zahab A, Spina L, Poncharal P, Marliere C, Water-vapor effect on the electricalconductivity of a single-walled carbon nanotube mat. Physical Review B 2000; 62:10000–10003

Overall Conclusions

Humidity is one of the major parameters of environment which affects both living and non-living organisms. Hence, broad spectrum of research pays a great attention to create or improve new sensing materials for humidity sensor.

In this research the sensing performances of different oxide/hydroxide nanoparticles supported onto natural sepiolite, as well as for the first time, iron-doped magnesium silicate nanopowders were evaluated and compared to alkaline and alkaline-earth doped hematite. Finally, in the last part of my research, a new sensing material based on pyrolyzed bamboo was successfully prepared and used as a humidity sensor.

All of these materials were produced from simple low cost wet chemical routes.

Different oxide/hydroxide nanoparticles were first precipitated onto sepiolite grains and the fact that these nanoparticles were supported on an inert matrix makes possible to avoid manipulation, agglomeration and harmful character that pure nanoparticles usually have. Among the investigated compositions, tungsten-doped sensors showed a significant response towards humidity at room temperature starting from 40% RH

An iron-doped magnesium silicate nanopowder was then successfully synthesized by a sol gel process. After screen-printing of the prepared powder, the humidity sensors were able to detect RH from 18 RH% with reasonable response and recovery times.

Doping hematite with metal ions to create surface defects or oxygen vacancies and to introduce in the sensing material ions which possess high local charge density able to increase the adsorption sites for water vapor was investigated too. Among the different

prepared compositions, sodium-doped hematite showed a significant response towards from 32% RH.

To conclude, biomass is a qualified carbon raw material source for the synthesis of valuable carbon-based materials because it is available in high quality and huge amount, and it is an environmental friendly renewable resource. Thus, in my Ph.D research, a new sensing material based on pyrolyzed bamboo was studied. The humidity sensing properties of the pyrolyzed bamboo based sensors were investigated at room temperature in the relative humidity (RH) range from 0.0 to 96.0%. The pyrolyzed bamboo based humidity sensors exhibited an excellent response towards humidity starting from 10% RH, while pyrolyzed and annealed sensing materials showed a response starting from 20% RH. Finally, both of them displayed reasonably fast response and recovery times.

Further work should be devoted to improve the sensitivity of the promising materials (iron-doped magnesium silicate and pyrolyzed bamboo) with the best results we already got in order to reach novel RH sensors and to examine their sensitivity towards other gases as: NO_x, CO2, and ammonia. The durability of the examined materials should be also studied.

Appendix – Experimental procedures

This section lists the main experimental procedures used in my research for the characterization of the microstructure of prepared materials such as the laser granulometry, the XRD, DTA, and the FE-SEM. In addition to investigate a further information of the obtained powders by FTIR and using BET to determine their SSA before realizing the screen-printing ink in order to find a relation between the structure (morphology) and the electrical response.

1. Laser granulometry

When a laser beam strikes the particles suspended in an inert medium, the produced diffracted rays present intensity and diffraction angle that depend on the size of the impacted particle.

As illustrated in fig. 1, a laser granulorneter consists of a laser beam source, at a fixed wavelength, and a series of detectors (multidiode detector) to measure the diffracted light as a function of the diffraction angle.

The granulometer Malvern Master sizer 2000 was used to evaluate the particle size distribution of the powders dispersed in ethanol. The Mie theory is used by the instrument to calculate the particle size distribution. This theory takes into account both the diffraction index and the refractive index of both the sample and the medium. The powders were dispersed in ethanol and deagglomerated for 5 min, prior to each measurement.

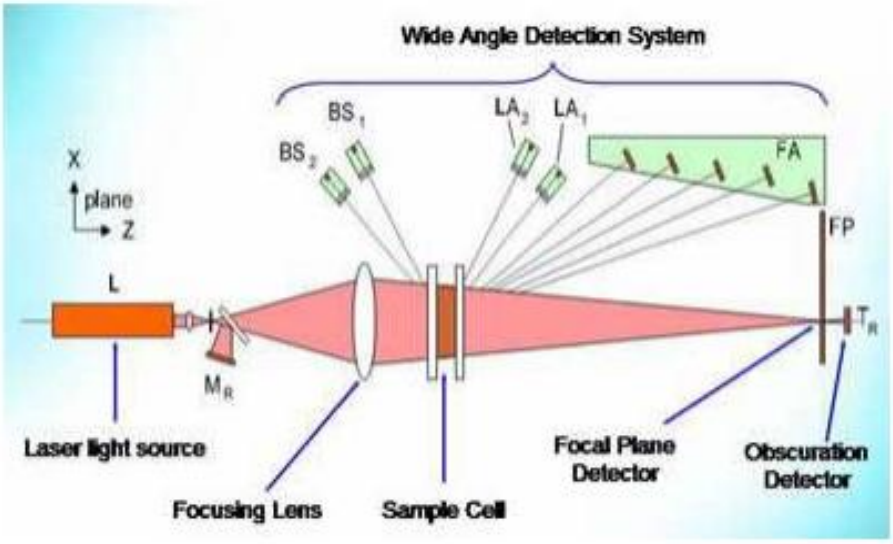

Fig.1. Schematic representation of a laser granulometer

2. X-ray diffraction

X-rays are electromagnetic waves that have 0.01-10 nm wavelength range and have energies in the range of about 100 eV to 10 MeV. These electromagnetic waves travel with the velocity of light and can behave just like particles according to the quantum theory. X-rays were discovered in 1985 by a German physicist Roentgen.

X-rays are produced in an X-ray tube that consists of a tungsten filament. Electrons are generated by the W-filament by thermionic emission and they are made to strike on the anode material by applying voltage. As a result of electrons bombardment on the target metal X-rays are produced that are passed through the windows W to get out of the X-ray tube as can be seen in fig.2.

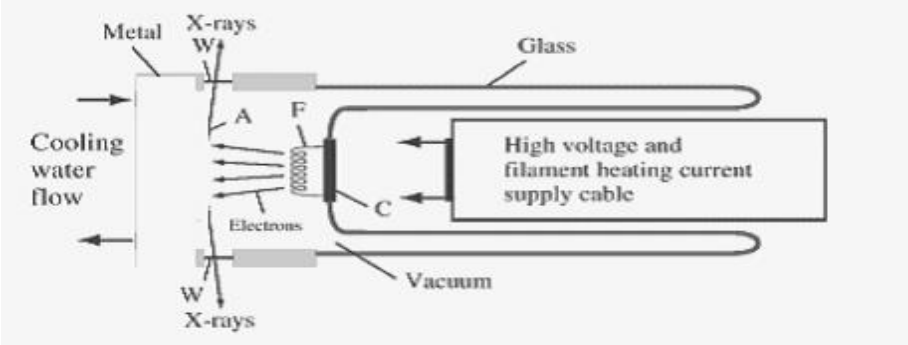

Fig.2. Schematic of an X-ray tube for the production of X-rays [1]

The X-ray tube contains filament F, target metal T and windows W through which X-rays come out of the tube as shown in fig.2 a schematic representation of the spectrum of X-rays produced from molybdenum target as a function of the applied voltage. There are two types of signals. One is the white signals while the others are characteristic radiations K_{α} and $K_{ß}$. In X-ray diffraction analysis of materials we want only the characteristic portion of the X-ray spectrum so we need to get rid of the white portion. This is done by

applying filters. Generally the filter material selected is of 1 atomic number (Z) less than the atomic number of the anode material used for the generation of the X-rays. A Schematic of copper radiation before and after passing through a nickel filter is shown in the fig.3.

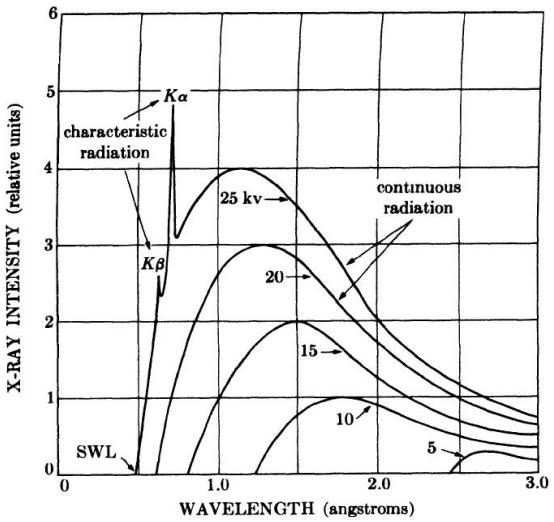

Fig.3. Typical X-ray spectrum of molybdenum as a function of applied voltage[2]

Target	Filter	K_{α}	$K_{\alpha 1}$	$K_{\alpha 2}$	K_{β}	K abs. edge
Cr	**V**	2.29092	2.0848	2.28962	2.29351	2.07012
Fe	**Mn**	1.93728	1.93597	1.93991	1.75663	1.74334
Co	**Fe**	1.79021	1.78892	1.79278	1.62075	1.60811
Cu	**Ni**	1.54178	1.54051	1.54433	1.39217	1.38043
Mo	**Zr**	0.71069	0.709226	0.713543	0.632253	0.61977

Table 1. Characteristic radiations of commonly used anodes and their filters

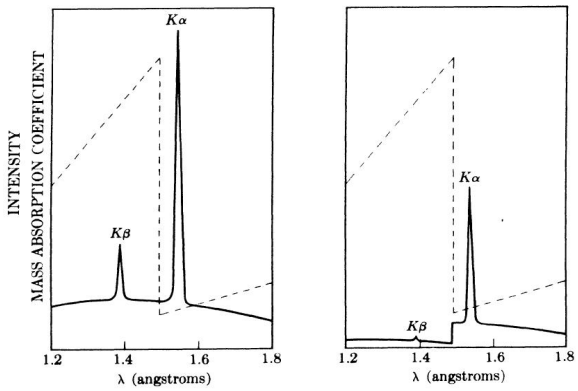

Fig.4. Schematic of copper radiation before (left) and after (right) passing through a nickel filter. dashed line shows the mass absorption coefficient of nickel [2]

When X-rays are incident on the materials, there are four main possible types of processes that can occur as the outcome as in fig.5. Some X-rays pass through the incident material (transmittance), some cause ejection of the electrons (photoelectric effect), some portion of them cause X-ray fluorescence while the others are scattered in various directions coherently or incoherently. The coherently scattered X-rays are used in the standard X-ray diffractometric for the analysis of materials nature and composition.

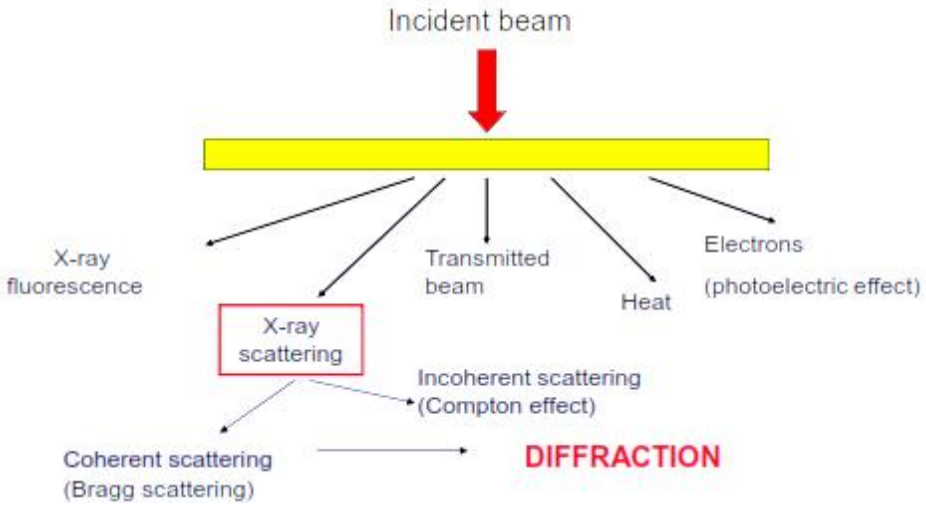

Fig.5. Interaction of X-rays with materials

The X-ray tubes are installed in the X-ray diffractometer equipment used to carry out the diffraction analysis of materials. A monochromatic beam of K_α radiations are struck on the samples after passing through the collimator and antiscatter slit. After the impingement on the sample, X-rays are scattered in various directions and they enter into an X-ray counter normally placed at the same angle as that of incident X-ray beam.

The main components of an X-ray spectrometer are shown in the fig. 6. They include an X-ray source F, sample holder S and detector G, Rowland circle passing through points F (target focal spot), S (center point of diffractometer), and G (the focal point of the diffracted beam), the divergent slits DS and the scattering slits SS, the receiving slit RS [3].

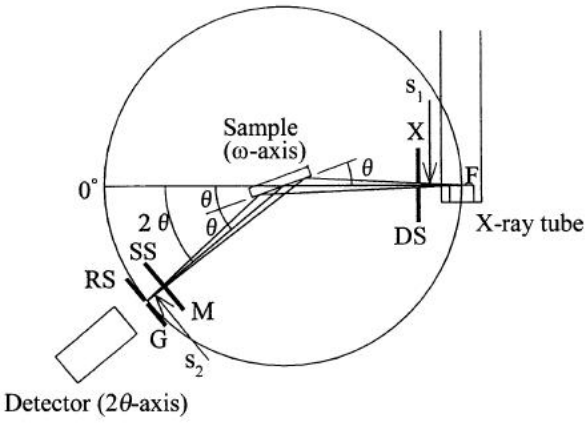

Fig.6 : Schematic of a typical diffractometer [3]

Elastically scattered X-rays from a crystal lattice can cancel each other (destructive interference) in some directions or can add up (constructive interference) in the other directions before entering to the counter. Bragg's law explains these diffractions as:

$$2dsin\theta = n\lambda \qquad \text{Eq.1}$$

Eq. 1. is a well know Bragg's equation where *d* is interplaner distance, θ is the incidence angle, λ is the wavelength, of the incident X-rays and *n* is an integer.

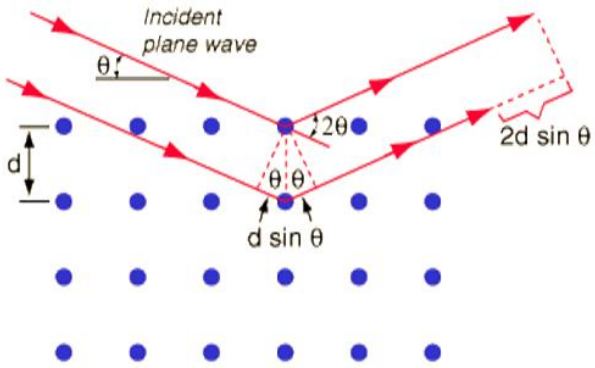

Fig.7. Interference of X-rays scattered by crystals

We *get I-2θ* data when X-ray source S is fixed and sample platform and counter rare is rotated at speeds of ω and 2ω separately. In this condition the diffractometer is called θ-2θ type diffractometer. Whereas if the sample platform is fixed but X-ray source and the X-ray counter both rotate with a same speed of ω, then we obtain *I-θ* data. In this arrangement, the diffractometer is called θ-θ type diffractometer. In this research θ-2θ type scans were done by using a Philips diffractometer between 20 and 80 ° (2θ). The Cu K_α radiations with wavelength (λ) 0.1504 nm were used. The generator voltage and generator current were set to 40 kV and 20 mA respectively. Whereas 0.08°/min was set as the speed of scanning and the step size used was 0.02° respectively.

The diffraction patters obtained from the diffractometry can be used and analyzed to have a lot of useful information about the samples. From angular position (2θ) of the

diffraction pattern peaks, we can have the knowledge about crystal system, spatial group symmetry, unit cell and the phases present. From the intensity *I* of the peaks give information about content of the unit cell, point symmetry, quantitative composition of the mixture as well as the preferred orientation or texture. Whereas from profile and width peak analysis of the diffraction patterns, we can have an idea about crystallite size (ranging from 1-100 nm), defects, residual stresses and texture.

For crystallite size measurement from XRD patterns, an equation developed by Scherrer is used which is given as in eq. 2:

$$d = k\lambda / B\cos\theta$$

where *d* is the crystallite size, K is a constant depending on the geometry of the grains, λ is the copper Kα wavelength, *B* is the width of the XRD peaks (full width at half maximum, FWHM), and θ is the diffraction angle. The value of the *B* is calculated by subtracting the width contributions due to the instrumental errors. The instrumental contributions to the peak width can be calculated by doing a reference scan on a well crystallized reference sample of Si or LaB_6 whose peak widths are only due to the instrumental effects. The actual contribution just from the sample to the broadening of the peak is then calculated by the following equation:

$$B = (B_{obs}{}^2 - B_{ref}{}^2)^{1/2} \qquad \text{Eq.3}$$

The value of *B* obtained from the Equation 2 is then used in the Scherrer eq. (Eq. 3.) to have the crystallite size.

3. Differential thermal analysis

DTA involves heating or cooling a test sample and an inert reference under identical conditions, while recording any temperature difference between the sample and reference. This differential temperature is then plotted against time, or against temperature. Changes in the sample which lead to the absorption or evolution of heat can be detected relative to the inert reference. Differential temperatures can also arise between two inert samples when their response to the applied heat treatment is not identical. DTA can therefore be used to study thermal properties and phase changes which do not lead to a change in enthalpy. The baseline of the DTA curve should then exhibit discontinuities at the transition temperatures and the slope of the curve at any point will depend on the micro structural constitution at that temperature.

A DTA curve can be used as a finger print for identification purposes, for example, in the study of clays where the structural similarity of different forms renders diffraction experiments difficult to interpret. The area under a DTA peak can be to the enthalpy change and is not affected by the heat capacity of the sample.DTA may be defined formally as a technique for recording the difference in temperature between a substance and a reference material against either time or temperature as the two specimens are subjected to identical temperature regimes in an environment heated or cooled at a controlled rate.

Experimental set up:

The key features of a differential thermal analysis

1. Sample holder comprising thermocouples, sample containers and a ceramic or metallic block.

2. Furnace.

3. Temperature programmer.

4. Recording system

The last three items come in a variety of commercially available forms and are not being discussed in any detail. The essential requirements of the furnace are that it should provide a stable and sufficiently large hot zone and must be able to respond rapidly to commands from the temperature programmer. A temperature programmer is essential in order to obtain constant heating rates. The recording system must have a low inertia to faithfully reproduce variations in the experimental set up.

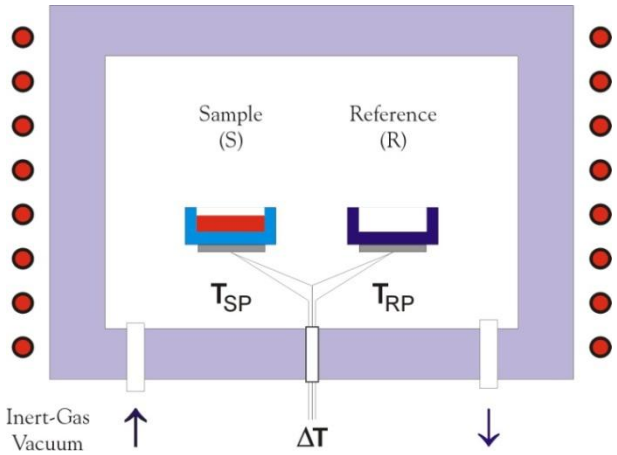

Fig. 8. Schematic illustration of a DTA cell.

The sample holder assembly consists of a thermocouple each for the sample and reference, surrounded by a block to ensure an even heat distribution. The sample is contained in a small crucible designed with an indentation on the base to ensure a snug fit over the thermocouple bead. The crucible may be made of materials such as Pyrex, silica, nickel or platinum, depending on the temperature and nature of the tests involved. The

thermocouples should not be placed in direct contact with the sample to avoid contamination and degradation, although sensitivity may be compromised.
Metallic blocks are less prone to base line drift when compared with ceramics which contain porosity. On the other hand, their high thermal conductivity leads to smaller DTA peaks. The sample assembly is isolated against electrical interference from the furnace wiring with an earthed sheath, often made of platinum coated ceramic material. The sheath can also be used to contain the sample region within a controlled atmosphere or a vacuum. During experiments at temperatures in the range from 200 to 500°C, problems are encountered in transferring heat uniformly away from the specimen. These may be mitigated by using thermocouples in the form of flat discs to ensure optimum thermal contact with the now flat bottomed sample container, made of aluminum or platinum foil. To ensure reproducibility, it is then necessary to ensure that the thermocouple and container are consistently located with respect to each other.

4. Fourier Transform Infra-Red Spectrometry

Fourier Transform Infrared (FTIR) spectroscopy is a spectroscopic technique used to determine the chemical functional groups in a sample. Different functional groups absorb characteristic frequencies of IR radiation. Using various sampling accessories, FTIR spectrometers can accept a wide range of sample types such as gases, liquids, and solids. Thus, FTIR spectroscopy is an important and popular tool for structural elucidation and compound identification. At temperatures above absolute zero, all atoms in molecules are in continuous vibration with respect to each other. When the frequency of a specific vibration is equals to the frequency of the IR radiation, the molecule absorbs the

radiation. The FTIR spectrometer consists of three important components, the IR source, IR detector and an interferometer.

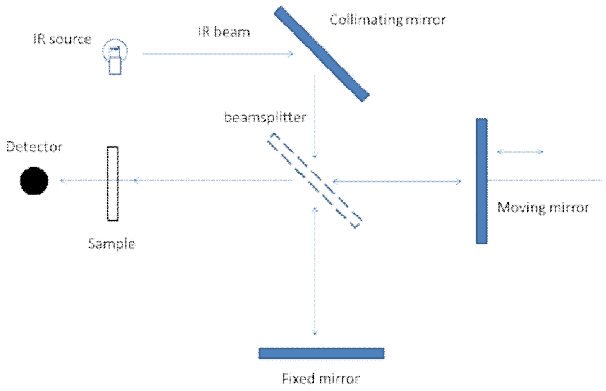

Fig. 9. Components of a FTIR spectrometer

An IR beam comprising of a mid-range IR frequency was directed onto a collimating mirror which reflects the collimated beam onto a beam splitter. The beam splitter is a semi-reflecting device and is often made by depositing a thin film of germanium onto a flat KBr substrate. Half the IR beam that falls on the beam splitter is transmitted to the fixed mirror while the other half is reflected onto the moving mirror. Both beams are reflected from their respective mirrors and recombine at the beam splitter. As the moving mirror changes position, an interference pattern is formed. The resulting beam then passes through the sample and is focused at the detector. The constructive or destructive interference patterns may form depending on the optical path difference between the beam splitter and the two mirrors. The two light beams will be in phase with each other when their optical path difference (δ) is multiple of their wavelength (λ) as the following equation 4.:

$$\delta = n\lambda \qquad \text{eq.4}$$

Where n= 0, 1, 2…. (integers)

The graph of the light intensity verse optical path difference is called an Interferogram. For FTIR, many wavelength of IR beam is emitted by the source at the same time; the resulting Interferogram is the superposition of all Interferogram of individual wavelength. The spectrum can be obtained by performing a Fourier transform.

5. BET analysis

In 1938, Stephen Brunauer, Paul Hugh Emmett, and Edward Teller published an article about the BET theory in a journal [4] for the first time; "BET" consists of the first initials of their family names.

BET theory aims to explain the physical adsorption of gas molecules on a solid surface and serves as the basis for an important analysis technique for the measurement of the specific surface area of a material.

The concept of the theory is an extension of the Langmuir theory, which is a theory for monolayer molecular adsorption, to multilayer adsorption with the following hypotheses:

1. Gas molecules physically adsorb on a solid in layers infinitely;

2. There is no interaction between each adsorption layer;

3. The Langmuir theory can be applied to each layer. The resulting BET equation is expressed by:

$$\frac{1}{[(P_0/P)-1]} = \frac{c-1}{V_m c}\left(\frac{P}{P_0}\right) + \frac{1}{V_m c} \qquad \text{eq.5}$$

Where P and P_0 are the equilibrium and the saturation pressure of adsorbates at the temperature of adsorption, v is the adsorbed gas quantity (for example, in volume units), V_m is the monolayer adsorbed gas quantity and c is the BET constant, which is expressed by:

$$c = \exp\left(\frac{E_1 - E_L}{RT}\right) \qquad \text{eq.6}$$

E_1 is the heat of adsorption for the first layer, and E_L is that for the second and higher layers and is equal to the heat of liquefaction.

Equation (5) is an adsorption isotherm and can be plotted as a straight line with $1/v[(P_0/P)-1]$ on the y-axis and $\phi = (P/P_0)$ on the x-axis according to experimental results (Fig. 10).

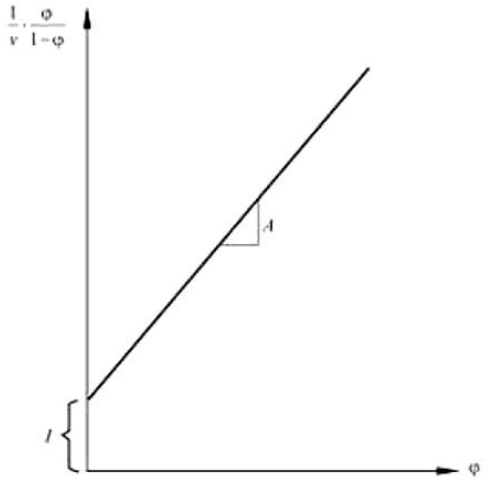

Fig. 10. Schematic representation of a BET plot.

This plot is called a BET plot. The linear relationship of this equation is maintained only in the range of $0.05 < P/P_0 < 0.35$. The value of the slope A and the y-intercept I of the line are used to calculate the monolayer adsorbed gas quantity V*m* and the BET constant c. The following equations can be used:

$$V_m = \frac{1}{A+1} \qquad \text{eq.7}$$

$$c = 1 + \frac{A}{I} \qquad \text{eq.8}$$

The BET method is widely used in surface science for the calculation of surface areas of solids by physical adsorption of gas molecules. A total surface area S_{total} and a specific surface area S are evaluated by the following equation:

$$S_{BET,total} = \frac{V_m NS}{V} \qquad \text{eq.9}$$

Where V*m* is in units of volume which are also the units of the molar volume of the adsorbate gas:

$$S_{BET} = \frac{S_{total}}{a} \qquad \text{eq.10}$$

Where N is Avogadro's number, s is the adsorption cross section of the adsorbing species, V the molar volume of adsorbate gas and a is the mass of adsorbent in (g).
The BET analyses were carried out by using the ASAP 2010 Micromeritics instrument.

6. Scanning electron microscopy

Scanning electron microscopes (SEM) have become very important in the field of characterization of materials. (SEM) is a type of microscope that utilizes a focused beam of electrons to generate high resolution details of the objects under examination. Due to very short wavelength of bombarding electron beams, (SEM) have a very high resolving powers, more depth of field and improved contrast than the optical microscopes [5]. The schematic setup for a scanning electron microscope labeled with important parts is shown in Fig.11

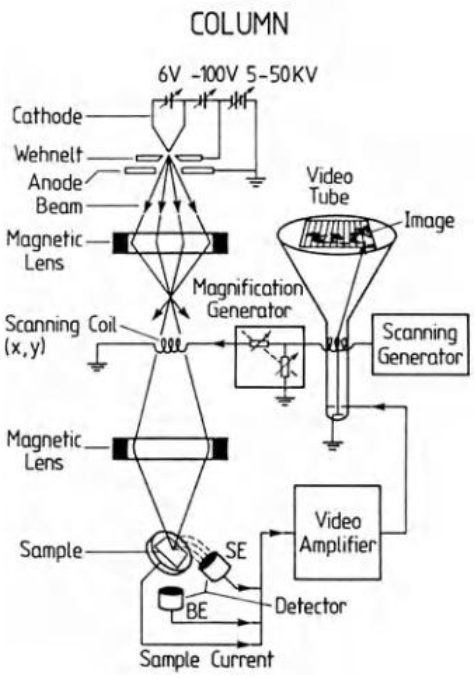

Fig. 11. Schematic Setup of Scanning Electron Microscope [6]

There can be listed several steps to state the imaging process of a (SEM) as given below:

1. A flux of free electrons is created in an electron gun. Electron gun consists of W filament cathode that generates these electrons by thermionic emission process.
2. The electron flux generated by the electron gun is accelerated down in an optical column with the help of high voltage potentials created at the anode.
3. Condenser lenses convert this flux of electrons into a beam of electrons
4. The current of this beam of electrons can be regulated by the condenser lenses and beam regulation aperture.
5. A stigmator is used to remove the ellipticity of the electrons beam
6. A final condensing lens fixes the beam of electrons onto a probe spot.
7. The electron beam bombards on the surface of the sample and as a result of which following types of signals are produced:

Secondary electrons (SE): These are low energy electrons that are emitted from the near surface of the sample. These electrons can be collected in a secondary electron detector to get topographic information of the sample.

Back scattered electrons (BSE): These are actually the bombarded electrons which are scattered back from the inner part of the sample little below the surface. They are higher density electrons than the secondary electrons. As these electrons come almost from the bulk of the sample so they contain information about the density depending upon the average atomic mass and we can say that the image also has information about the compositions of the chemical components of the sample.

X-rays: X-rays are also generated from the sample that can be resolved on the basis of their wavelengths or energies. The characteristic waves resolved on the basis of energy

are collected in the Energy Dispersive X-ray (EDX) Analyzer for composition analysis. Whereas, it is also possible to resolve X-rays by diffraction phenomenon through a regular and periodic solid and can be collected in a gas filled counter called Wavelength Dispersive Spectrometer (WDS).

In addition to the secondary electrons, back scattered electrons and X-rays, light photons or heat is also generated as a result of the electrons beam bombardment on the sample under observation. Generally the secondary electrons come from top few nanometers of the volume of the sample. Whereas the back scattered electrons come from top 40% of the volume and X-rays are emitted from the entire region of bombardment.

Volume and mechanism of electron matter interactions in scanning electron microscopy is shown in fig.12

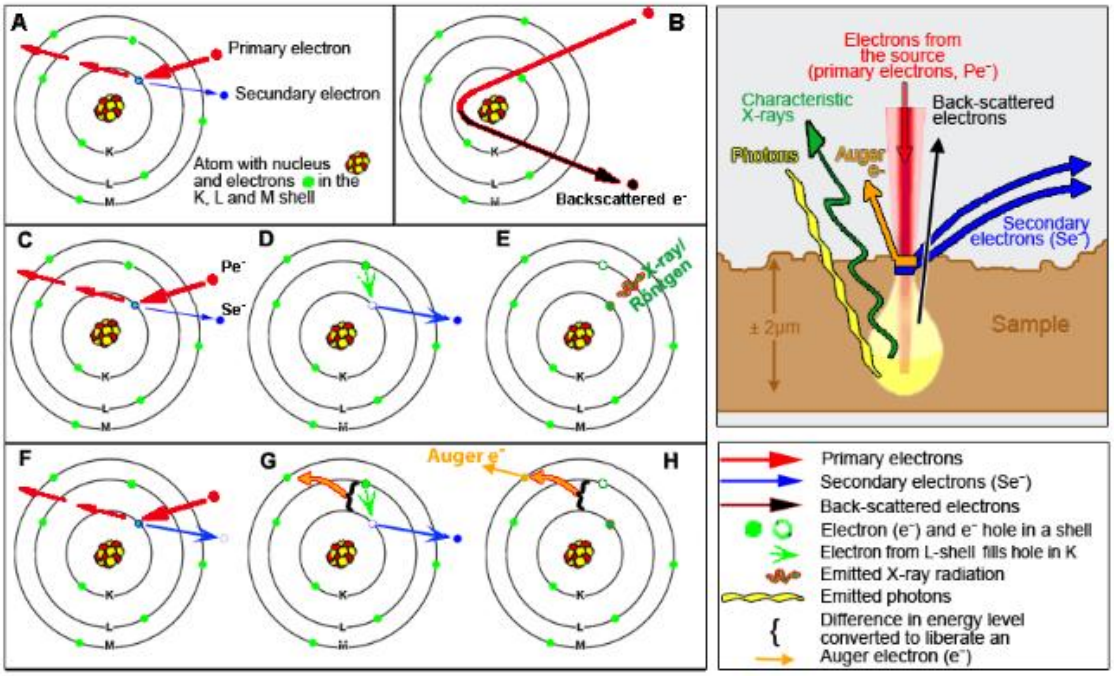

Fig. 12. Volume and mechanism of electron matter interactions (SEM)

7. Screen-printing technique

The screen-printing consists of forcing a rubber or plastic flexible blade, called squeegee, to transfer an ink onto the substrate through a screen (Fig.13).

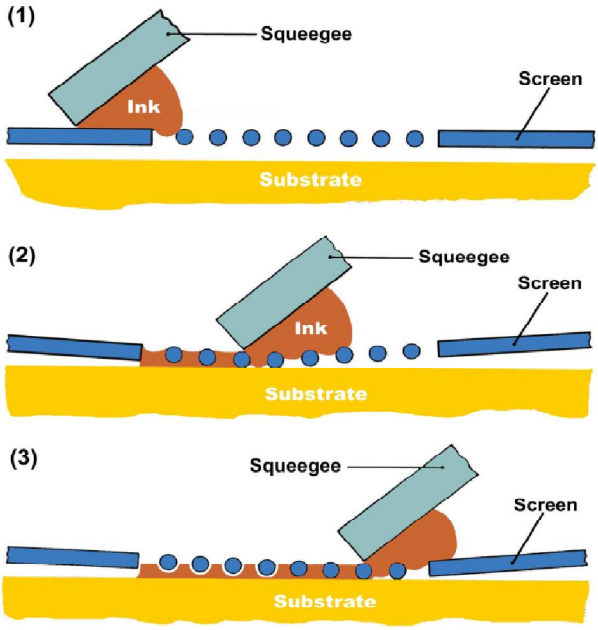

Fig.13. schematic of the screen-printing process [7].

The screen defines the pattern of the printed film and also meters the amount of paste deposited onto the substrate. The most common type of screen comprises a frame, normally cast aluminum or stainless steel, onto which a finely woven mesh is stretched. The mesh itself is usually based on a plain weave pattern, as depicted in fig. 14. Generally, a typical mesh count might be 200 strands per inch: the mesh opening depends on the mesh count and the filament diameter. For a given mesh count, the smaller the filament diameter, the larger the mesh opening which will therefore allow a greater volume of ink to be deposited onto the substrate. Hence, the mesh opening provides one of the means of checking the thickness of the deposit.

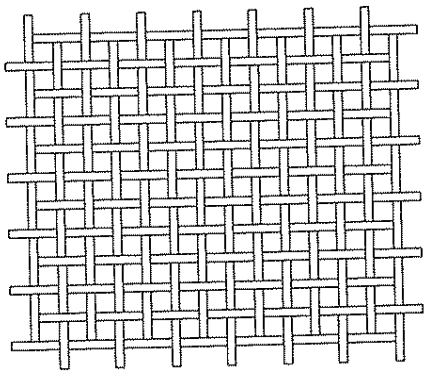

Fig. 14. A plain weave pattern for a typical thick film screen

It is possible to quantify the percentage open area of mesh through which the ink is able to pass:

$$Percentage = \frac{100A^2}{(A+D)^2} \qquad \text{eq.11}$$

where A is the mesh aperture and D is the filament diameter.

A cross-section of a mesh and many definitions and terms used are shown in fig. 15.

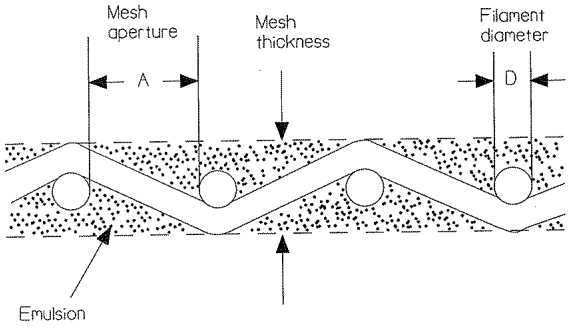

Fig.15. Cross-section of a screen mesh

The pictures of the semi-automatic screen-printing machine used in our laboratory to realize sensors is shown in fig.16, while the masks used to screen print the components of the sensors are presented in fig. 16: in particular the screen's patterns can be different depending on what it is going to be deposited, for example in our laboratory two screens were used, one to realize the electrodes, the other is to deposit the sensing layer.

The used screens were all made of stainless steel and their apertures were 270 mesh, corresponding to 53 µm.

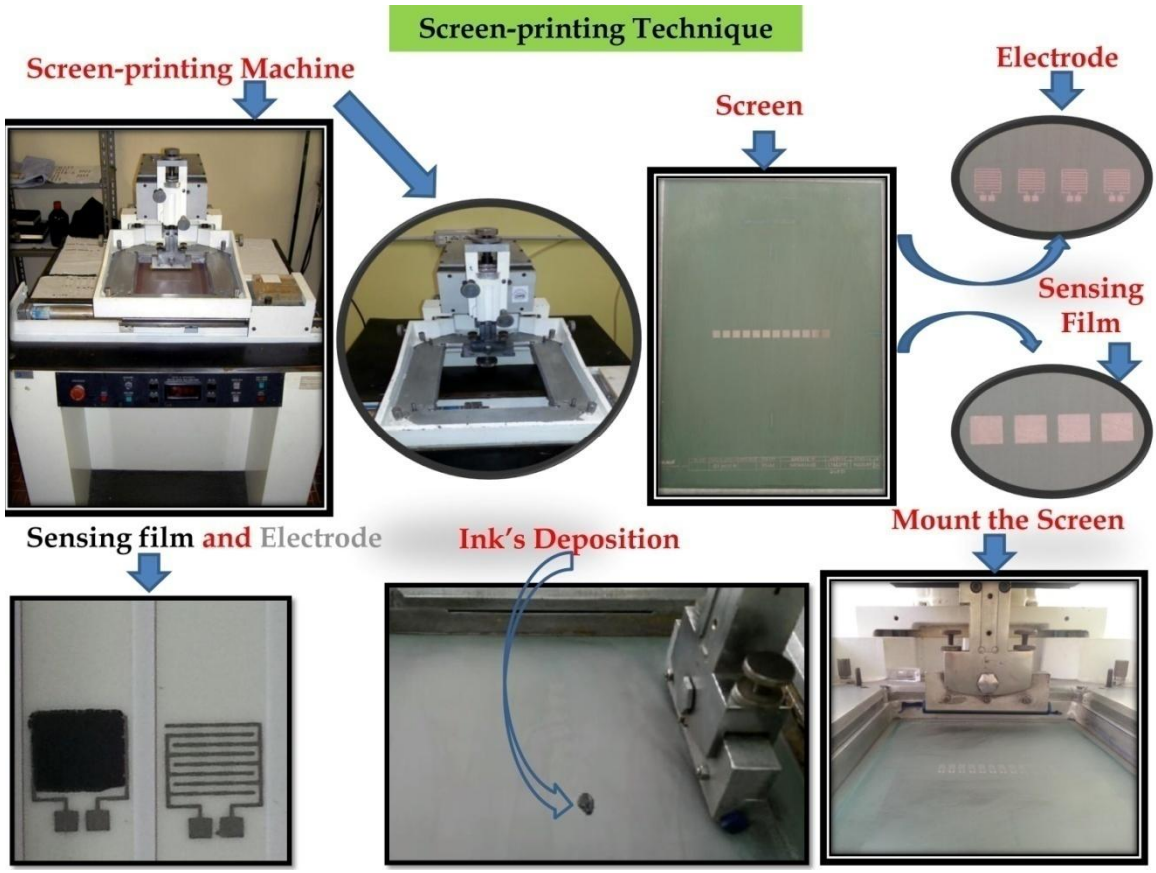

Fig. 16. Schematic diagram of screen-printing technique

8. Screen-printing inks

Each paste for producing thick films contains three components: the basic component, the flux and the binding phase. The flux is a component, also called organic vehicle, which provides a homogeneous suspension of the particles of the basic components and a rheology suitable for the printing of the film configuration. Hence, the vehicle is a temporary, sacrificial ingredient, which should be removed completely in the following steps of the process, during which the microstructure of the deposits is formed. The typical rheological behavior of a screen-printing ink is reported in fig.17.

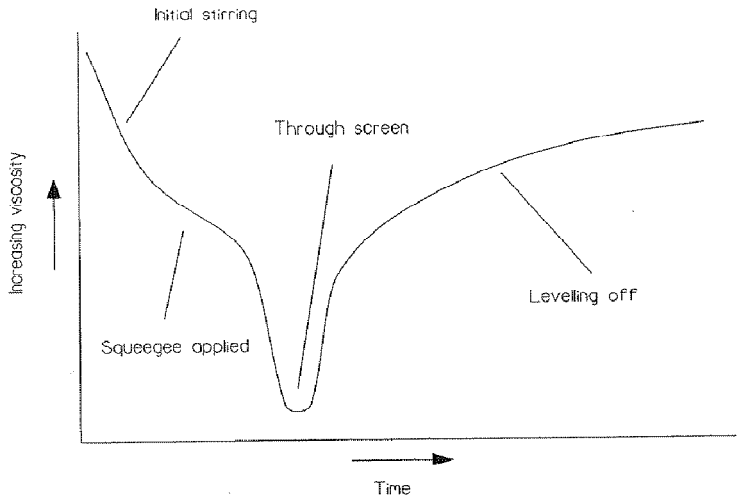

Fig. 17. Rheological behavior of a screen-printing ink.

The rheological behavior a paste should have is thixotropic, because firstly the ink must easily pass through the weaves of the screen thanks to the squeegee's action and then it regains its starting viscosity, such that the deposit keeps the shape of the screen's apertures when it is onto the substrate. So, referring to fig. 17, the paste's viscosity must first of all decrease during the squeegee's action, and then it must rapidly increase when it passes through the screen, coming back to its starting value.

It is possible to remove the sacrificial ingredient by considering two steps: the drying and the firing processes.

In general these two steps are necessary for sensors realization: after printing, the film or electrodes should stand in air for few minutes/hours, in order for the ink to level off and settle. The aim of the drying stage is to remove the organic solvents and make the printed film adherent to the substrate and relatively immune to smudging. The organic agent is still present in the ink at this stage; drying takes place at temperatures between 100-150°C in a conventional oven. The firing process is a phase in which the printed films or electrodes are heat treated for higher temperatures: the thermal program is specifically studied for every sample. At this step, the ink's components are thermally decomposed, leading to an evident shrinkage of the deposit (Fig. 18).

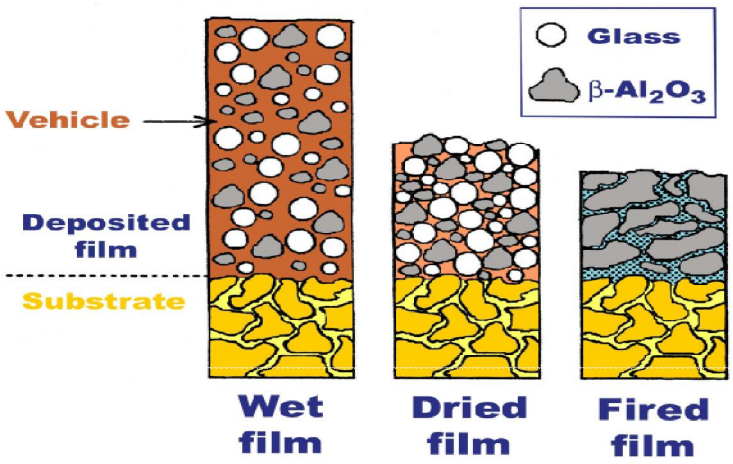

Fig. 18. Shrinkage of the thick film from the wet to the dried phase, followed by the fired stage. As an example, the basic component chosen is α-Al_2O_3

In laboratory, the organic vehicle used to realize the inks, was a blend of terpineol- type solvent, namely ethylene glycol monobutyal ether (Emflow, Emca Remex, USA). The binding phase was poly-(vinyl butyral-co-vinyl alcohol-co-vinyl acetate) (PVB, Aldrich, USA), which created the paste plasticity and ensured the necessary adhesion of the film

to the substrate before the paste was fired. In particular, for all the pastes realized, 0.053 g of PVB and 1.2 cc of Emflow were used: these components were mixed overnight by ball-milling, in order to obtain a homogeneous viscous liquid, and then 2 g of the basic components (doped hematite) were added and mixed to the liquid, thus obtaining a dense paste, ready to be printed on the substrate. Actually two different architectures were developed to create the ceramic sensors: the first one was the classical way to realize screen-printed devices, in particular the sensing films were deposited onto α-Al_2O_3 planar substrates (Coors Tek, USA, ADS-96 R, 96% alumina, 0.85 cm × 5 cm^2) and, on top of them, interdigitated electrodes were printed, while the second one dealt with interdigitated electrodes printed onto the substrate and the sensing layer overlapped them. Interdigitated gold electrodes were used for sensors assembly: starting from a commercial ink (ESL EUROPE 8835 (520°C)), the gold paste was screen-printed onto a α-Al_2O_3 substrate by using a rubber squeegee, or onto the sensing materials: after drying overnight, the electrodes were dried and fired at 520°C for 18 minutes with a 2°C/min heating ramp to optimize their electrical conductivity, according to the ink's manufacturer recommendations. Fig. 19. refers to the architecture's sensors, obtained by printing the paste containing the sensing material (Fig. 19b, in particular the ink was composed by Sr-doped hematite powder) onto an alumina substrate (Fig. 19a). After the sintering treatment of the paste, gold interdigitated electrodes were printed onto the

sensing material (Fig. 19c), followed by a firing process.

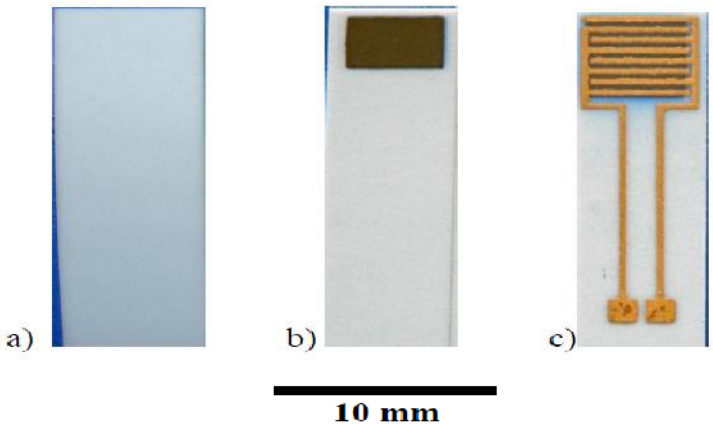

Fig. 19. Steps for the first architecture's sensors assembly

9. Relative humidity measurement device

Humidity test of the sensors were carried out by using a laboratory apparatus for their testing made of a thermostated chamber, operating at 25°C, in which relative humidity (RH) could be varied between 0 and 96%. In this system, referring to (fig. 20), compressed air was separated into two fluxes: one was dehydrated over a chromatography alumina bed, while the second one was directed through two water bubblers, generating, respectively, a dry and a humid flow [8]. Two precision microvalves allowed to recombine the two fluxes into one by means of a mixer and to adjust the RH content while keeping constant the testing conditions: a flow rate of 0.05 L/s. The laboratory apparatus for sensors testing was calibrated such that to ensure a constant air flow during electrical measurements and relative humidity (RH) was varied by steps, each one of 3 minutes.

An external alternating voltage (V = 3.6 V & 1 kHz) was applied on each tested sensor, placed into a PVC tube, acting as a variable resistance of the electrical circuit described above. The sensor resistance was determined by a calibration curve (Fig. 21), drawn by

substituting the sensors, in the circuit, by known resistances. In particular, the sensors operated from about 1.3 V to 2.4 V, corresponding to about 700 kΩ to 7 kΩ. RH values were measured by means of a commercial humidity and temperature probe(Delta Ohm DO9406, Italy, accuracy: ± 2.5% in the 05-90% RH range).

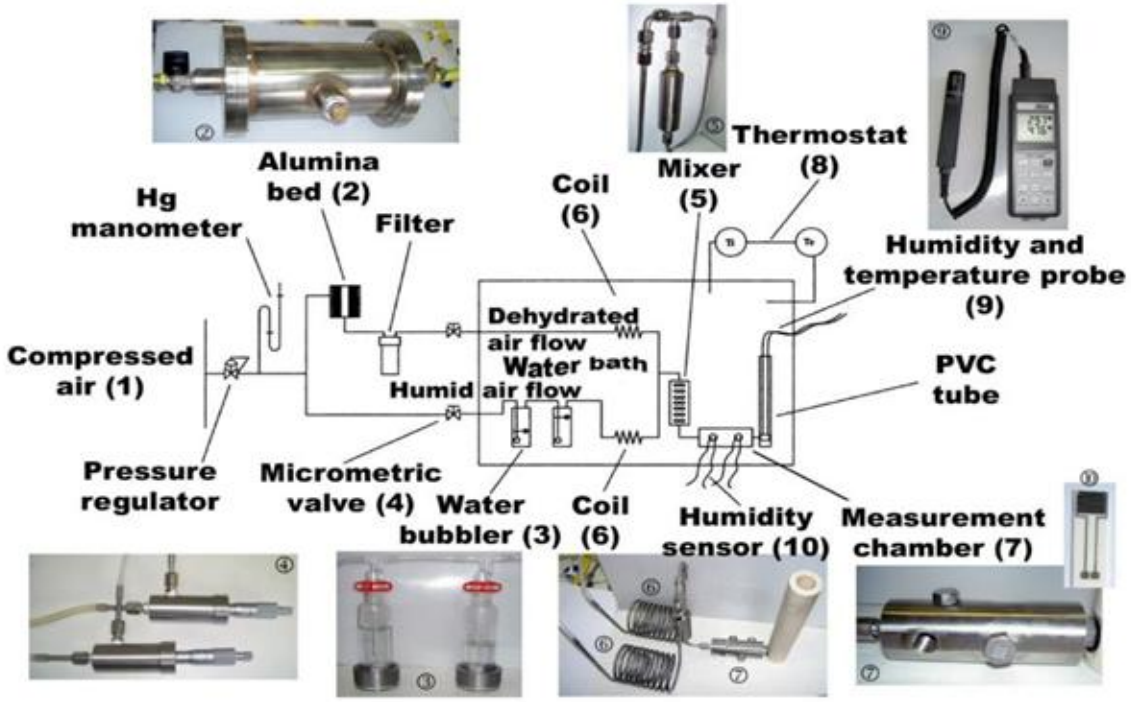

Fig.20. Schematic of the lab apparatus for sensors testing [8]

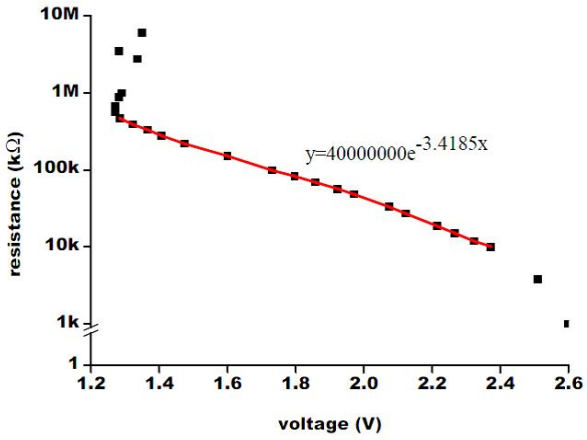

Fig. 21. Calibration curve for sensors testing: red fit indicates the range of voltage in which the sensors operated. In the eq. y indicates resistance, x voltage.

References

[1] Graef, M. De & E. McHenry, M., 2007. Structure of Materials: An Introduction to crystallography, Diffraction and Symmetry, Cambridge, UK: Cambridge University Press

[2] Cullity, B.D., 1956. Elements of X-Ray Diffraction, USA: Addison-.

[3] Waseda, Y., Matsubara, E. & Shinoda, K., 2011. X-Ray Diffraction Crystallography, New York, NY: Springer New York Dordrecht Heidelberg London.

[4] S. Brunauer, P. H. Emmett and E. Teller, J. Am. Chem. Soc. 60, (1938) 309.

[5] Rochow, T.G. & Rochow, E.G., 1995. An Introduction to Microscopy by Means of Light, Electrons, X-Rays, or Ultrasound, Boston, MA: Springer US. Available at: http://link.springer.com/10.1007/978-1-4684-2454-6

[6] Luth, H., 1995. Surfaces and Interfaces of Solid Materials 3rd ed., , NY: Springer.

[7] G. Franzosi and J. M. Tulliani, Serigraa: tecnica preferita per la realizzazione di sensori a gas, Ceramurgia 4 (1999) 273-283.

[8] J.-M. Tulliani, P. Bonville, Influence of the dopants on the electrical resistance of hematite-based humidity sensors, Ceramics International 31 (2005) 507–514.

List of Publications

▲Referred Journal Articles.

1- **Ahmed S. Afify**, M. Ataalla, Azhar Hussain, M. Hassan, Amr Mohammed, J.M. Tulliani, "*Studying the Effect of doping metal ions onto crystalline hematite-based humidity sensors for Environmental Controlling*", **Bulgarian Chemical Communications** (**In press**, Reg. No. **BCC-3899**).

2- M. Hassan, **Ahmed S. Afify**, J.-M. Tulliani, "Synthesis of ZnO nanoparticles onto sepiolite neddles and determination of their sensitvity towards humidity, NO_2 and H_2", **J. Materials Science & Technology** (**In Press**, doi:10.1016/j.jmst.2016.03.008).

3- Mohamed Hassan, **Ahmed Sabry Afify**, Mohamed Ataalla, Amr Mohammed, Anna Staneva, Yanko Dimitriev, Jean Marc Tulliani, "*Preparation and characterization of a zinc oxide nanopowder supported onto inorganic clay*", **J. Chemical Technology and Metallurgy**, Vol. 51(2): 168-172 (2016) ISSN: 1314-7978 (on line).

4- **Ahmed S. Afify**, M. Hassan, M. Piumetti, I. Peter, B. Bonelli, J-M. Tulliani, "*Elaboration and characterization of modified sepiolites and their humidity sensing features for environmental monitoring*", **Applied Clay Science**,Vol. 115: 165–173 (2015) doi:10.1016/j.clay.2015.07.019.

5- M. Ataalla, M. Milanova, M. Hassan, **Ahmed S. Afify**, J.M. Tulliani, Y. Dimitriev, "*Nano- and microsized phases in the WO_3-ZnO-Nd_2O_3-Al_2O_3 system for applications in environmental monitoring*", **Nano-Science Advances in CBRN Agents Detection, Information and Energy Security NATO Science for Peace and Security Series A: Chemistry and Biology**, 451–459 (2015) doi:10.1007/978-94-017-9697-2_46.

▲Referred Conference Articles.

6- Alessio Carullo, Alberto Vallan**, Ahmed S. Afify**, J.-M. Tulliani, "*Development of a fast humidity sensor based on quartz tuning fork*, **Proceeding of IEEE International Instrumentation and Measurement Technology** in Taipei, Taiwan (**I²MTC 2016**) (**Accepted,** Reg . No. **1570226836**).

7- **Ahmed Afify**, M. Hassan, I. Peter, B. Bonelli, J.-M. Tulliani, *"Humidity Sensing Properties of Modified Sepiolite"*, **Proceeding of the 2nd Int. Conf. on Advanced Materials and Nanotechnology** in Hanoi, Vietnam (**ICAMN 2014**)38–44 (2014) ISBN: 978-604-911-946-0.

"وما توفيقى إلا بالله عليه توكلت وهو رب العرش العظيم وأخر دعوانا أن الحمد لله رب العالمين"

أحمد صبري بطحيش-تورينو-إيطاليا 2016